Fermi-edge polaritons with finite hole mass

Dimitri Pimenov

Master's Thesis
Theoretical and Mathematical Physics

Chair of Theoretical Solid State Physics
Faculty of Physics
Ludwig-Maximilians-University Munich

Supervisors: Prof. Dr. Jan von Delft
Dr. Oleg Yevtushenko

May 2015

Contents

List of symbols and abbreviations

This list shows frequently used symbols and abbreviations in alphabetic order along with the definition if it is short, and the formula, figure or page where they first appear.

$A(\mathbf{q}, \Omega)$	2DEG absorption, c.f. (1.38)
$A_I(\epsilon)$	absorption close to Ω_I, c.f. (4.14)
$A_{\text{Ladder}}(\epsilon)$	absorption in the ladder approximation, c.f. (3.12)
$A_{np}(\nu)$	non-perturbative absorption with the Mahan Ansatz, c.f. (3.40)
$A_{np}(y)$	non-perturbative absorption with the Nozières Ansatz, c.f. Fig. 4.14
$A_p(\nu)$	perturbative absorption with the Mahan Ansatz, c.f. Fig. 3.11
$A_p(y)$	perturbative absorption with the Nozières Ansatz, c.f. Fig. 4.4
$\mathcal{A}_{\text{ep}}(\epsilon, \delta)$	exciton-polariton spectral function, c.f. (5.3)
$\mathcal{A}_h(\epsilon)$	infinite mass VB hole spectral function, c.f. (2.39)
$\mathcal{A}_h^c(0, \epsilon)$	coherent part of the ($Q = 0$) VB hole spectral function, c.f. (2.96)
$\mathcal{A}_h^i(0, \epsilon)$	incoherent part of the ($Q = 0$) VB hole spectral function, c.f. (2.97)
$\mathcal{A}_h(\mathbf{Q}, \Omega)$	finite mass VB hole spectral function, c.f. (2.59)
$\mathcal{A}_{\text{np}}(\epsilon, \delta)$	non-perturbative Fermi-edge polariton spectral function for finite hole mass, c.f. Fig. 5.4
$\mathcal{A}_{\text{p}}(\epsilon, \delta)$	perturbative Fermi-edge polariton spectral function for finite hole mass, c.f. Fig. 5.6
$\mathcal{A}_\infty(\epsilon, \delta)$	Fermi-edge polariton spectral function for infinite hole mass, c.f. Fig. 5.2
$a_{\mathbf{k}}$	destruction operator of a CB electron, c.f. (1.2)
a_0	excitonic Bohr radius, c.f. (1.63)
$b_{\mathbf{k}}$	destruction operator of a finite mass VB electron, c.f. (1.2)
b	destruction operator of a infinite mass VB electron, c.f. (1.2)
CB	conduction band, c.f. page 11

CLA	consistent ladder approximation, c.f. page 71
$c_{\mathbf{k}}$	destruction operator of a cavity photon, c.f. (1.8)
$D(t)$	infinite mass VB hole propagator, c.f. (2.10)
$D(\mathbf{Q}, t)$	finite mass VB hole propagator, c.f. (2.3)
$D_c(\mathbf{q}, \Omega)$	cavity photon propagator, c.f. (1.22)
$d_{\mathbf{k}}$	destruction operator of a VB hole, c.f. (2.1)
E_B	Mahan exciton binding energy, c.f. (3.14)
E_G	semiconductor band gap, c.f. page 11
$E_{\mathbf{k}} = k^2/2M$	VB dispersion, c.f. (1.3)
$E_R = (2k_F)^2/2M$	VB hole recoil-energy, c.f. (2.79)
E_0	Wannier exciton binding energy, c.f. (1.62)
F_n	n-th order term in the linked cluster expansion of the VB hole propagator, c.f. (2.22)
FER	Fermi-edge regime, c.f. page 28
$G_{\mathrm{ep}}(\epsilon, \delta)$	exciton-polariton propagator, c.f. (5.1)
$G_{\mathrm{exc}}(\omega)$	exciton propagator (supplement), c.f. (7.8)
$G_c(\mathbf{k}, \omega)$	CB propagator, c.f. (1.40)
$G_v(\mathbf{k}, \omega)$	VB propagator, c.f. (1.40)
$g = \rho V_0$	electron-hole coupling constant, c.f. (2.16)
g_{ep}	exciton-photon coupling constant, c.f. (1.67)
$g_{\mathrm{exc}} = g - 1$	effective exciton-electron interaction, c.f. (7.10)
g_{fp}	Fermi-edge-photon coupling constant, c.f. (5.5)
$gL = g\log(\epsilon + i0^+/\xi)$	parameter controlling the infinite mass leading log expansion, c.f. (3.15)
$g\log(\beta g^2)$	parameter controlling the finite mass leading log expansion, c.f. (3.33)
$g_1(\beta)$	coupling constant separating the perturbative and the non-perturbative absorption regimes, c.f. (3.34)
$g_2(\beta) = \sqrt{\beta}$	coupling constant defining the regime where the Mahan approach works, c.f. (3.38)
H	full light-matter Hamiltonian, c.f. (1.21)

H^{CV}	full electronic Hamiltonian, c.f. (1.21)
H_0^{CV}	bare electronic Hamiltonian, c.f. (1.2)
H_{i}	infinite mass electronic Hamiltonian in the initial state, c.f. (2.7)
H_{f}	infinite mass electronic Hamiltonian in the final state, c.f. (2.8)
H_I^{ph}	light-matter interaction Hamiltonian, c.f. (1.20)
H_0^{ph}	bare photon Hamiltonian, c.f. (1.8)
H_∞	infinite mass electronic Hamiltonian, c.f (2.7) f.
I_1	channel 1 irreducible vertex, c.f. page 81
I_2	channel 2 irreducible vertex, c.f. page 81
$k_0 = \sqrt{2m_{\mathrm{cav}}\Gamma_c}$	photon momentum unit, c.f. (5.8)
M	VB effective mass, c.f. (1.1)
$M_{\mathbf{q}}$	optical matrix element, c.f. (1.19)
$M_+ = m + M$	exciton mass, c.f. page 21
m	CB effective mass, c.f. (1.1)
$m_r = mM/(m+M)$	reduced mass, c.f. page 21
m_{cav}	cavity effective mass, c.f. page 14
m_0	bare electronic mass, c.f. page 12
$N(\nu)$	scattering phase space, c.f. (2.29)
$n_F(\omega)$	$(T = 0)$ Fermi function, c.f. (1.44
QW	quantum well, c.f. page 1.2
$\mathcal{S}$	quantum well area, c.f. (1.13)
R	vertex irreducible in both channels, c.f. page (4.35)
$V(\mathbf{q})$	electron-hole interaction matrix element, c.f. (1.39)
V_0	electron-hole contact interaction matrix element, c.f. (1.71)
VB	valence band, c.f. page 11
W_n	n-th order term in the standard perturbative expansion of the VB hole propagator, c.f. (2.60)
$y = \epsilon/\beta\mu$	rescaled detuning from Ω_I, c.f. (4.27), chapter 4 only

$\alpha = \rho E_B/g^2$	prefactor appearing in exciton-diagrams, c.f. (7.7)
$\beta = m/M$	CB-VB mass ratio, c.f. (1.52)
$\Gamma = g^2\beta\mu$	VB hole decay rate, c.f. (3.22)
Γ_c	cavity photon linewidth, c.f page 89
γ	full electron-hole interaction vertex, c.f. Fig. 4.5
$\gamma_{\mathbf{q}} = M_{\mathbf{q}}^2 \cdot \mathcal{S}$	effective light-matter coupling strength, c.f. (1.53)
γ_0	effective light-matter coupling strength for $\mathbf{q} = 0$, c.f. (1.53)
γ_1	channel 1 reducible vertex, c.f. page 81
γ_2	channel 2 reducible vertex, c.f. page 81
$\Delta_{\mathbf{q}} = E_{\mathbf{Q}-\mathbf{q}} - E_{\mathbf{Q}}$	change of hole energies via electron scattering, c.f. (2.73)
δ	detuning of the cavity mode from the exciton mode/ from the indirect threshold in the FER regime, c.f. (1.68)
$\delta(\omega)$	scattering phase shift, c.f. (2.15)
ϵ	detuning from E_G for the hole propagator, c.f. (2.40)/ detuning from Ω_I for the absorption, c.f. (3.8)
$\epsilon_{\mathbf{k}} = k^2/2m$	CB dispersion, c.f. (1.3)
Λ	full vertex with two legs, c.f. Fig. 4.11
μ	chemical potential, c.f. page 11
ν	detuning from Ω_D, c.f. (3.30)
ξ	UV cutoff of the contact interaction, c.f. page 28
$\Pi(\mathbf{q}, \Omega)$	photon self-energy, c.f. (1.31)
$\Pi_{\mathrm{db}}(\Omega)$	photon self-energy contribution of the bubble with a dressed VB propagator, c.f. (4.16)
$\Pi_{\mathrm{ep}}(\epsilon)$	photon self-energy in the exciton-polariton regime, c.f. (5.2)
$\rho = m/2\pi$	2D single spin density of states, c.f. (1.51)
$\Sigma(\Omega)$	infinite mass hole self-energy, c.f. (2.49)
$\Sigma(\mathbf{Q}, \Omega)$	finite mass hole self-energy, c.f. (2.119)
χ_2	Lindhard-function, c.f. (2.81)
$\Omega_D = E_G + \mu(1+\beta)$	direct absorption threshold, c.f. (3.28)
$\Omega_I = E_G + \mu$	indirect absorption threshold, c.f. (3.2)

ω	detuning from $-E_B$ (supplement), c.f. (7.8)
$\omega_{\mathbf{q}}$	cavity photon dispersion, c.f. (1.6) f.
2DEG	two-dimensional electron gas, c.f. page 12

Abstract

Microcavity polaritons are half-light-half-matter eigenmodes of a quasi two-dimensional system where a direct semiconductor quantum well is embedded in an optical resonator (microcavity). For polaritons to appear, the cavity photon mode energy must be tuned close to an optical transition of the semiconductor. When the semiconductor is heavily n-doped, the relevant transition corresponds to the well-known Fermi-edge singularity, leading to the formation of so-called Fermi-edge polaritons.

In the usual derivation of the Fermi-edge singularity one assumes an infinite valence band hole mass, which is appropriate for low-mobility samples. To describe high-mobility samples, a finite valence band hole mass is required. Recently, the mobility-dependence of Fermi-edge polaritons has been experimentally investigated in Ref. [1], where a high-mobility and a low-mobility sample were compared. The measured polariton spectral function showed a clear mode splitting into an upper and a lower polariton for the low-mobility sample, but for the high-mobility sample almost no mode splitting was reported.

To understand this outcome, we investigate spectral properties of two-dimensional microcavity polaritons in heavily doped semiconductors, with special emphasis on a finite valence band hole mass. A diagrammatic evaluation of the Green's function of the valence band hole for vanishing and large momenta is presented, and the underlying physics of the hole recoil is outlined. Using the outcome of this calculation and restricting ourselves to linear response, we compute the self-energy of the microcavity photon, relying on the diagrammatic approach initiated by Mahan and Nozières. Perturbative and non-perturbative self-energy regimes are introduced and studied for frequencies close to the optical threshold. The parametric limitations of the theory are outlined.

As a result, we are able to compute the polariton spectral function. In the non-perturbative regime, where electron-hole interaction effects dominate as compared to the hole recoil, the polariton spectrum as function of energy and cavity detuning still shows some branch splitting (c.f. Fig. 5.4). In the perturbative regime, where the hole recoil is most prominent, the splitting is seen to vanish almost completely (c.f. Fig. 5.6). Comparing our results with the measurements of Ref. [1], we find them to be in qualitative agreement.

1. Introduction

When a high quality direct semiconductor quantum well (QW) is placed inside an optical microcavity, the strong interaction of photons and QW excitations confined in two dimensions gives rise to a new quasiparticle: the polariton. The properties of this fascinating half-light-half-matter particle strongly depend on the nature of the involved matter excitations.

If the Fermi energy is in the semiconductor band gap, the matter excitations consist of single conduction band electrons bound to valence band holes, so called excitons, and are particle-like. This case is well understood in theory, and the first observation of the resulting microcavity exciton-polaritons was already accomplished in 1992 by Weisbuch et al. [2]. Several studies on exciton-polaritons revealed remarkable results. E.g. exciton-polaritons were shown to form a Bose-Einstein condensate [3], and were proposed as a mechanism for High-T_c superconductivity [4].

If the Fermi energy is significantly above the conduction band bottom, the matter excitations have a complex many-body origin, and loose their quasi-particle nature. An experimental study of the resulting "Fermi-edge polaritons" was first conducted in 2007 by Gabbay et al. [5], and recently extended by Smolka et al. [1] (2014).

The theoretical explanation of Fermi-edge polaritons can be found in the extensive literature on the related "Fermi-edge problem". This problem has been a major topic in theoretical condensed matter physics for a long time, with seminal contributions made by Mahan [6] and Nozières [7], [8], [9].

However, the Fermi-edge problem was mostly studied under the simplifying assumption of an infinite valence band hole mass, corresponding to low-mobility samples. This model fails to explain the experimental findings in [1], where a high-mobility sample was studied, for which an almost complete vanishing of the polariton splitting was reported.

In this work, we aim to remove the assumption of infinite hole mass, and to obtain a qualitative understanding of the resulting two-dimensional Fermi-edge polaritons. We will also compare our theory to the experimental results of [1].

As the first step, we will introduce the setup under consideration and recall the standard theory of exciton-polaritons, which will allow us to formulate the statement of the problem of this thesis in section 1.9.

1.1. Direct gap semiconductors

In this part we will introduce the electronic system which will be studied, and the basic theoretical assumptions. For further detail compare chapter 8 of [10].

Direct gap semiconductors are systems which have fascinating physical features, but still are simple enough for an analytical description.

Their basic electronic properties can be described by a simple two band model, as shown in Fig. 1.1.

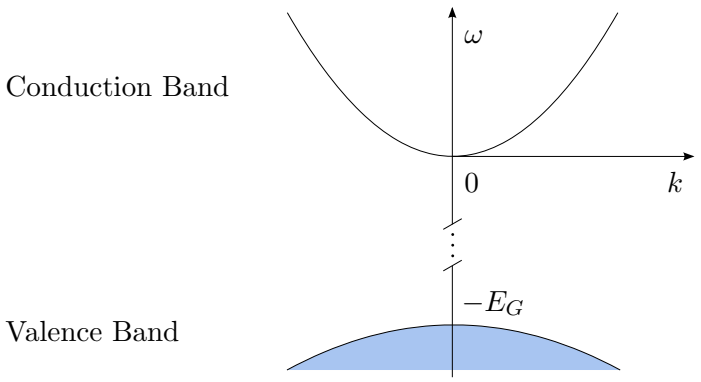

Figure 1.1.: 1D projection of the bandstructure of a typical direct gap semiconductor. Blue shading visualizes filled states.

There is a valence band (VB) with a negative curvature near the Γ-point ($\mathbf{k} = 0$), and a conduction band (CB) with a positive curvature near the Γ-point, with their extrema at momentum $k = 0$, and separated by a gap of energy E_G. By considering only two bands, we can study processes which take place at an energy $E \simeq E_G$. The typical material used in optical experiments is the III-V compound semiconductor GaAs, for which $E_G = 1.518$ eV (see Table 8.2 of Ref. [10]).

In all our considerations E_G will be the largest energy-scale, e.g. much larger than the bandwidths of both bands.

To begin with, let us assume that the chemical potential μ is in the gap: $-E_G < \mu < 0$.

As indicated in Fig 1.1, especially close to the Γ-point, the energy bands have an almost parabolic shape. Therefore, we can define an effective mass in the standard way:

$$m := \left(\frac{\partial^2 E_c}{\partial k^2}\right)^{-1} = \text{const} \ , \qquad M := -\left(\frac{\partial^2 E_v}{\partial k^2}\right)^{-1} = \text{const} \ . \tag{1.1}$$

where $E_{c,v}$ is the energy of the CB and VB electrons, correspondingly, and $k = |\mathbf{k}|$. We always use units s.t. $\hbar = 1$.

We will only study optical experiments fine-tuned to the narrow energy range where this effective mass approximation is valid.

The effective masses have to be understood in a Fermi-liquid picture, containing atomic crystal effects, and intraband interaction effects such as Coulomb CB electron-electron interactions.

Let us further note at this point that we will not consider any temperature effects. Thus, our description will be limited to temperatures T smaller than the low-energy scales that appear in our evaluations. This also allows us to disregard phonons, which are frozen out.

After all simplifications, the system is described by the following Hamiltonian:

$$H_0^{CV} = \sum_{\mathbf{k}} \frac{k^2}{2m} a_{\mathbf{k}}^\dagger a_{\mathbf{k}} - \sum_{\mathbf{k}} \left[\frac{k^2}{2M} + E_G\right] b_{\mathbf{k}}^\dagger b_{\mathbf{k}} \ . \tag{1.2}$$

Here, $a_{\mathbf{k}}$ and $b_{\mathbf{k}}$ are electron operators for the CB and VB, correspondingly. The energy is measured from the bottom of the CB, see Fig. 1.1.

The momentum in (1.2) belongs to the first Brillouin zone. The space dimensionality will be specified in the next section. We also implicitly assume spin sums. However, in this thesis we will never actually consider spin physics except for prefactors of 2.

We will often use the abbreviations:

$$\epsilon_{\mathbf{k}} = \frac{k^2}{2m} , \qquad E_{\mathbf{k}} = \frac{k^2}{2M} . \tag{1.3}$$

For the effective masses appearing in (1.2) we have $M \gg m$. In real GaAs samples, actually the situation is more complicated, namely there are (at least) two hole bands called heavy hole (hh) and light hole (lh) band, the hh band having the larger energy. In units of bare electron mass m_0, the CB and the hh-band masses in 3D read (see Table 8.4 of Ref. [10]):

$$m_{CB} =: m \simeq 0.066 , \qquad m_{hh} =: M \simeq 0.47 \qquad \Rightarrow \qquad \beta := \frac{m}{M} \simeq 0.14 . \tag{1.4}$$

In the following we take into account the hh-band only, always assuming that $\beta \ll 1$. A possible origin for even larger hole band masses is disorder in the system. Classically, in disordered systems we have spatially fluctuating potentials, which can bind electrons. The larger the particle mass, the easier it can be bound or localized. Thus, the heavy VB electrons tend to form such localized state. This can justify the assumption of an infinite hole mass ($M = \infty$).

1.2. Quantum wells

So far we did not specify the dimensionality of our system. From now on we will only be concerned with systems that are effectively two-dimensional, so called two-dimensional electron gases (2DEG). The physical realization of a 2DEG can be achieved with a quantum well (QW) . A detailed review can be found in chapter 19 of Ref. [11].

Qualitatively, a QW is made inserting the semiconductor in question A between two layers of a semiconductor B, see Fig. 1.2(a). For a GaAs QW, often the combination $Al_{1-y}Ga_yAs$ is used. If we want to achieve a confinement of electrons and holes in the thin layer A, we need a z-dependence of the band extrema in the sample as shown in Fig. 1.2(b). Such a structure is called a type I QW.

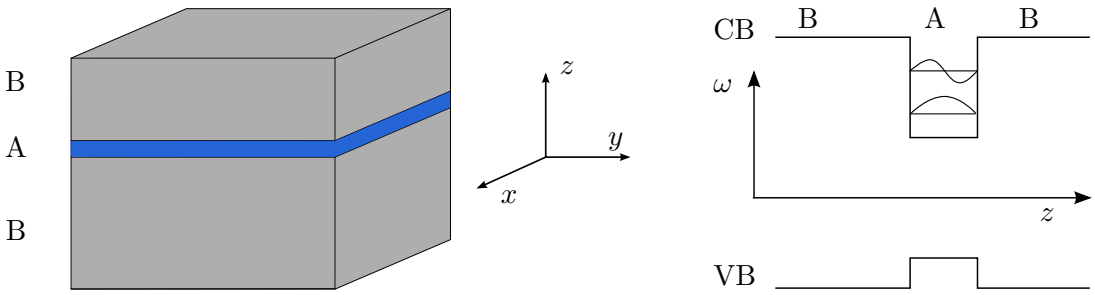

Figure 1.2.: (a) A typical QW. (b) z-dependence of band extrema of a type I QW.

In an idealized picture, the band discontinuities at the layer edges form a square well potential in z-direction. The electron bands then split into a finite number of discrete

subbands, where each band corresponds to a particular envelope-function solution of the Hamiltonian in z-direction. Two such envelope functions are indicated in Fig. 1.2(b). The energies of the subbands read:

$$E_n(\mathbf{k}_\parallel) = \epsilon_n + \frac{1}{2m^*}(k_x^2 + k_y^2) \ , \tag{1.5}$$

where $\mathbf{k}_\parallel$ is the in-plane momentum and ϵ_n is the n-th energy level of the z-dependent Hamiltonian. For a square well potential one has $\epsilon_n \sim \frac{n^2}{d^2}$, where d is the width of the thin layer. Hence, for thin enough layers the subband-splitting is large enough s.t. we can consider only one subband n_α for the CB and VB each, usually the lowest respectively highest one. In the following we will do so, and disregard all z-dependence, effectively treating all envelope functions as delta functions.

We will further absorb the subband-splitting ϵ_{n_α} in the definition of the gap, which we regard as experimental parameter.

However, we can still assume the gap to be of the same order as in the 3D case – e.g. in the quasi-2D experiment of Ref. [1] the measured value for GaAs is $E_G \simeq 1.52$ eV.

In reality, also the effective masses can be different in 2D, with a strong dependence on concrete experimental parameters, especially on the electron density. For high enough densities, which will be the regime consired from chapter 2 onwards, one can assume the values to be similar to the 3D case (see e.g. Ref. [12] for the CB and Ref. [13] for the VB).

1.3. Interaction with light

Let us now study the interaction of the system specified by (1.2) with light (c.f. [14], chapter 13, [15], chapter 10). In particular we will be interested in setups where not only the electrons, but also the photons are confined in 2D, which will lead to a reversible light-matter coupling (as opposed to a simple radiative decay of the matter excitations). As will be shown below, the general advantage of a 2D setup as compared to 3D is an enhanced light-matter coupling.

The confinement of photons can be achieved by inserting the QW in the center of an optical cavity, i.e a system consisting of two mirrors with high reflectivity separated by a distance L. In our setups of interest $L \simeq \ \mu$m, hence one uses the name *microcavity*. The mirrors can either be metallic or consist of so-called *distributed Bragg reflectors* (DBR), which are made of alternating layers of a quarter of wavelength of semiconductor materials with different indices of refraction.

This optical resonator has standing wave eigenmodes. A sketch of a setup with metallic mirrors and of the lowest eigenmode is shown in Fig. 1.3.

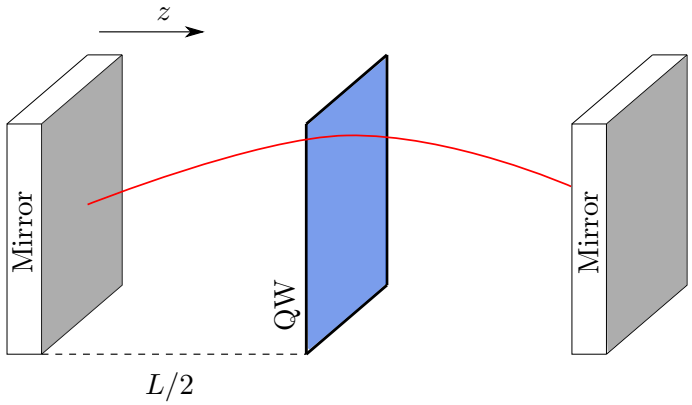

Figure 1.3.: Sketch of an optical cavity with a QW inside. The red line indicates the electrical field strength of the lowest cavity eigenmode.

The cavity eigenmodes have the following dispersion as function of the QW in-plane wave-vector $\mathbf{q}$:

$$\omega_{\mathbf{q}} = \frac{c}{n_{\text{cav}}}\sqrt{\frac{\pi^2 l^2}{L^2} + \mathbf{q}^2} \ , \tag{1.6}$$

where c is the speed of light, n_{cav} the cavity refractive index and $l \in \mathbb{N} \setminus \{0\}$ is any natural number. We assume that the cavity is lossless and absorptionless except for the QW, i.e. $n_{\text{cav}} = \sqrt{\epsilon_{\text{cav}}}$, where ϵ_{cav} is the cavity dielectric constant. Restricting ourselves to the lowest mode and for light fields incident almost perpendicular to the xy-plane, i.e. for $\mathbf{q}^2 \ll \pi^2/L^2$, we can write:

$$\omega_{\mathbf{q}} \simeq \omega_0 + \frac{\mathbf{q}^2}{2m_{\text{cav}}} \ , \tag{1.7}$$

with $\omega_0 = c\pi/n_{\text{cav}}L$ and the effective cavity mass $m_{\text{cav}} = \omega_0 \cdot n_{\text{cav}}^2/c^2$. Restoring units, for $\hbar\omega_0 \simeq 1.5$ eV and typical AlGaAs DBR cavities, one obtains $m_{\text{cav}} \simeq 3 \cdot 10^{-5}\ m_0$.

The cavity mode energy can be modified using a wedged cavity geometry, s.t. the effective length L depends on the position of the QW in the cavity.

The bare cavity photon Hamiltonian reads:

$$H_0^{\text{ph}} = \sum_{\mathbf{q}} \omega_{\mathbf{q}} c_{\mathbf{q}}^\dagger c_{\mathbf{q}} \ , \tag{1.8}$$

where $c_{\mathbf{q}}$ are bosonic photon operators. The sum in (1.8) implicitly contains the summation over polarizations. Since we disregard spin physics, we will also not consider any explicit polarization dependence.

In our setup the cavity modes will interact with the QW modes. Let us now sketch the derivation of the 2D interaction Hamiltonian and emphasize the underlying approximations.

We start with the standard minimal coupling Hamiltonian:

$$H_I^{\text{ph}} = \int d^2r\ \hat{\Psi}^\dagger(\mathbf{r}) \left(-\frac{e}{m_0}\hat{\mathbf{A}}(\mathbf{r}) \cdot \hat{\mathbf{p}} + \frac{e^2}{2m_0}\hat{\mathbf{A}}^2(\mathbf{r}) \right) \hat{\Psi}(\mathbf{r}) \ , \tag{1.9}$$

Here, e is the unit charge, m_0 the bare electronic mass, $\hat{\mathbf{A}}(\mathbf{r})$ the quantized electromagnetic vector-field operator in the Coulomb gauge, and $\hat{\mathbf{p}}$ the momentum operator. The integral runs over the whole QW. $\hat{\Psi}(\mathbf{r})$ is the position field operator defined as:

$$\hat{\Psi}(\mathbf{r}) = \sum_{\mathbf{k}} \phi_{c,\mathbf{k}}(\mathbf{r}) a_{\mathbf{k}} + \sum_{\mathbf{k}} \phi_{v,\mathbf{k}}(\mathbf{r}) b_{\mathbf{k}} \ , \tag{1.10}$$

where the ϕ-factors are the single particle wavefunctions for the CB and VB for momenta $\mathbf{k}$. These are products of plane waves and Bloch functions. We now insert (1.10) into (1.9) and restrict ourselfes to one-photon-processes, thus ignoring the part proportional to $\hat{\mathbf{A}}^2$. In addition, we consider interband transitions only. In this way we obtain:

$$H_I^{\mathrm{ph}} = \sum_{\mathbf{k},\mathbf{p}} a_{\mathbf{k}}^\dagger b_{\mathbf{p}} \cdot \left(-\frac{e}{m_0}\right) \int d^2r \ \overline{\phi_{c,\mathbf{k}}(\mathbf{r})} \ \hat{\mathbf{A}}(\mathbf{r}) \cdot \hat{\mathbf{p}} \ \phi_{v,\mathbf{p}}(\mathbf{r}) \qquad + \qquad h.c. \tag{1.11}$$

We now use the mode-expansion of the vector-potential:

$$\hat{\mathbf{A}}(\mathbf{r}) = \sum_{\mathbf{q}} \frac{\mathcal{E}_{\mathbf{q}}}{\omega_{\mathbf{q}}} \left(\mathbf{u}_{\mathbf{q}}(\mathbf{r}) c_{\mathbf{q}} + \overline{\mathbf{u}_{\mathbf{q}}(\mathbf{r})} c_{\mathbf{q}}^\dagger \right) \ . \tag{1.12}$$

$\omega_{\mathbf{q}}$ the cavity mode dispersion as in (1.7), and $\mathbf{u}_{\mathbf{q}}$ contains the polarization vectors $\mathbf{e}_{\mathbf{q}}$:

$$\mathbf{u}_{\mathbf{q}}(\mathbf{r}) = \frac{1}{\sqrt{\mathcal{S} \cdot L}} \ \mathbf{e}_{\mathbf{q}} \exp\left(i\mathbf{q} \cdot \mathbf{r}\right) \ , \tag{1.13}$$

where $\mathcal{S}$ is the QW area. We will work in the thermodynamic limit $\mathcal{S} \to \infty$.

$\mathcal{E}_{\mathbf{q}}$ is the electrical field amplitude created by one photon, which fulfills the relation:

$$\mathcal{E}_{\mathbf{q}} = \sqrt{\frac{\omega_{\mathbf{q}}}{2\epsilon_{\mathrm{cav}}}} \ . \tag{1.14}$$

Inserting (1.12) into (1.11) gives 4 terms. Of these we disregard the terms of the form $a_{\mathbf{k}}^\dagger b_{\mathbf{p}} c_{\mathbf{q}}^\dagger$ and $a_{\mathbf{k}} b_{\mathbf{p}}^\dagger c_{\mathbf{q}}$, since they describe the simultaneous creation or annihilation of a cavity photon and a CB-VB electron-hole pair, which is beyond our description. Ignoring these terms corresponds to the *rotating wave approximation*. As long as we only study processes where the cavity mode energies $\omega_{\mathbf{q}}$ are comparable to the band gap E_G, this approximation is excellent.

The result then reads:

$$H_I^{\mathrm{ph}} = \sum_{\mathbf{k},\mathbf{p},\mathbf{q}} a_{\mathbf{k}}^\dagger b_{\mathbf{p}} c_{\mathbf{q}} \cdot \underbrace{\left(-\frac{e}{m_0}\right) \cdot \frac{\mathcal{E}_{\mathbf{q}}}{\omega_{\mathbf{q}}} \int d^2r \ \overline{\phi_{c,\mathbf{k}}(\mathbf{r})} \ \mathbf{u}_{\mathbf{q}}(\mathbf{r}) \cdot \hat{\mathbf{p}} \ \phi_{v,\mathbf{p}}(\mathbf{r})}_{=M_{\mathbf{k},\mathbf{p},\mathbf{q}}} \quad + \quad h.c. \tag{1.15}$$

In evaluating the optical matrix element $M_{\mathbf{k},\mathbf{p},\mathbf{q}}$ we switch to a sum of integrations over crystal unit cells. We also make use of the *electric Dipole approximation*, which corresponds to ignoring the space dependence of the polarization vector on the length scale of one unit cell:

$$\exp\left(i\mathbf{q} \cdot \mathbf{r}\right) \simeq 1 \qquad \text{for} \qquad \mathbf{r} = \mathcal{O}(a_0) \ , \tag{1.16}$$

where a_0 is the lattice constant. In the energy range of interest this approximation is certainly valid, since

$$\lambda_{\text{optical}} \simeq \frac{2\pi\hbar c}{E_G} \simeq 1\ \mu\text{m}\ , \tag{1.17}$$

while $a_0 = \mathcal{O}(\text{Å})$.

With these considerations after some manipulations we end up with:

$$M_{\mathbf{k},\mathbf{p},\mathbf{q}} = \delta_{\mathbf{k},\mathbf{p}+\mathbf{q}} \cdot -i \underbrace{\frac{\epsilon_{\mathbf{k}} + E_{\mathbf{p}} + E_G}{\omega_{\mathbf{q}}}}_{\simeq 1} \frac{\mathcal{E}_{\mathbf{q}}}{\sqrt{\mathcal{S}\cdot L}} \cdot \underbrace{N \int_{s_0} d^2 r \overline{\phi_{c,\mathbf{k}}(\mathbf{r})}\, (\mathbf{e}_{\mathbf{q}} \cdot e\mathbf{r})\, \phi_{v,\mathbf{p}}(\mathbf{r})}_{=\mu_{cv}}\ , \tag{1.18}$$

where the integral runs over one unit cell with area s_0, and N is the number of unit cells in the QW. μ_{cv} is recognized as the familiar dipole matrix element. It stays finite in the thermodynamic limit due to the normalization of the single particle wave functions.

We will ignore the momentum dependence of the dipole matrix element, which is weak for momenta sufficiently far away from the edge of the Brillouin zone. In addition we approximate the ratio of the difference of the band energies and the cavity photon energy by 1, as indicated in (1.18). Thus, we can write:

$$M_{\mathbf{k},\mathbf{p},\mathbf{q}} = -iM_{\mathbf{q}} \cdot \delta_{\mathbf{k},\mathbf{p}+\mathbf{q}} \qquad \text{with} \quad M_{\mathbf{q}} \in \mathbb{R}\ , \tag{1.19}$$

and our final expression for H_I^{ph} reads:

$$H_I^{\text{ph}} = -i \sum_{\mathbf{p},\mathbf{q}} M_{\mathbf{q}} \cdot a^\dagger_{\mathbf{p}+\mathbf{q}} b_{\mathbf{p}} c_{\mathbf{q}} \qquad + \qquad h.c. \tag{1.20}$$

In comparison to 3D, the 2D wavefunctions of the CB and VB appearing in 1.18 have an enhanced overlap. This results in a stronger light-matter interaction, which is advantageous for optical experiments.

The expressions (1.8), (1.20) are the only cavity terms we are going to consider. We will disregard other effects like cavity driving or photon-photon interactions. A review of such additional effects can be found in Ref. [16].

The first term of (1.20) describes the following basic process: a photon comes in and lifts an electron from the VB to the CB. This results in a VB hole. A sketch of this process for an empty CB is shown in Fig. 1.4.

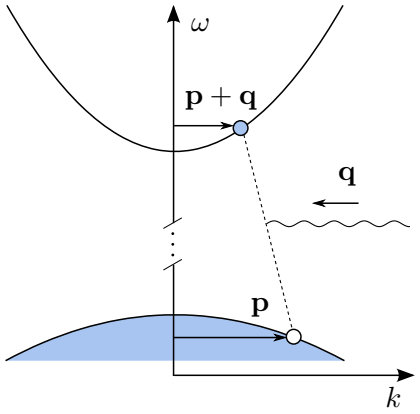

Figure 1.4.: Sketch of an electron-hole creation process and involved momenta. The wavy line represents the photon.

In the literature one often switches to hole operators for the VB. We will, however, always make use of electron operators except for chapter 2.

1.4. The photon propagator

One important point is still missing in our description:

As first observed by Wannier [17], as soon as a VB hole is created, it will interact with the CB electrons via an attractive Coulomb-interaction, which will depend on the transferred momentum.

Since the attraction only occures after a photon absorption process, it is called a *final state interaction*. Taking it into account, our Hamiltonian reads:

$$H = \underbrace{\sum_{\mathbf{k}} \epsilon_{\mathbf{k}} a^\dagger_{\mathbf{k}} a_{\mathbf{k}} - \sum_{\mathbf{k}} \left[E_{\mathbf{k}} + E_G\right] b^\dagger_{\mathbf{k}} b_{\mathbf{k}} + \frac{1}{\mathcal{S}} \sum_{\mathbf{k},\mathbf{q},\mathbf{p}} V(\mathbf{p}-\mathbf{k}) a^\dagger_{\mathbf{k}} a_{\mathbf{p}} b_{\mathbf{k}-\mathbf{q}} b^\dagger_{\mathbf{p}-\mathbf{q}}}_{=H^{CV}} + \tag{1.21}$$
$$+ \sum_{\mathbf{q}} \omega_{\mathbf{q}} c^\dagger_{\mathbf{q}} c_{\mathbf{q}} - i \sum_{\mathbf{p},\mathbf{q}} M_{\mathbf{q}} \cdot a^\dagger_{\mathbf{p}+\mathbf{q}} b_{\mathbf{p}} c_{\mathbf{q}} \quad + \quad h.c. \quad .$$

We will specify $V(\mathbf{p}-\mathbf{k})$ later. The optical properties of this system can be extracted from the connected photon-propagator of a single cavity mode, which we define in a standard way as:

$$D_c(\mathbf{q},t) = \frac{\langle\Phi|\hat{T}\left\{c_{\mathbf{q}}(t) c^\dagger_{\mathbf{q}}(0)\right\}|\Phi\rangle}{\langle\Phi|\Phi\rangle} \ , \tag{1.22}$$

Here, $\hat{T}$ denotes the time-ordering operator, $|\Phi\rangle$ the interacting photon vacuum, and $c_{\mathbf{q}}(t), c^\dagger_{\mathbf{q}}(t)$ are Heisenberg-picture operators w.r.t. the full Hamiltonian H (1.21). The spectral information is contained in the retarded photon Green's function:

$$D^R_c(\mathbf{q},\Omega) = \frac{1}{\Omega - \omega_{\mathbf{q}} + i0^+ - \Pi^R(\mathbf{q},\Omega)} \ , \tag{1.23}$$

where 0^+ is an infinitesimal positive number and $\Pi^R(\mathbf{q},\Omega)$ the retarded photon self-energy.

(1.23) describes a photon, which is dressed by QW polarization excitations. We can also think of it as a new quasiparticle. After Hopfield [18] this quasiparticle is called *polariton*, which is a combination of the words photon and polarization.

Our aim will be to calculate polariton properties, which can be done perturbatively in H_I^{ph}. To this end we write:

$$\tilde{H} + H_I^{\mathrm{ph}} = H \ , \tag{1.24}$$

and apply conventional $T = 0$ perturbation-theory w.r.t. $|0\rangle$, the ground-state of $\tilde{H}$. $|0\rangle$ describes a state without VB holes in the system.

Starting from (1.22), we then obtain (c.f. Ref. [19], Formula (8.9)):

$$iD_c(\mathbf{q},t) = \sum_{n=0}^{\infty} \frac{(-i)^n}{n!} \int_{-\infty}^{\infty} dt_1 ... dt_n \frac{\langle 0|\hat{T}\left\{H_I^{\mathrm{ph}}(t_1)...H_I^{\mathrm{ph}}(t_n)c_{\mathbf{q}}^\dagger(t)c_{\mathbf{q}}(0)\right\}|0\rangle}{\langle 0|U_\epsilon(\infty,-\infty)|0\rangle} \ . \tag{1.25}$$

$U_\epsilon(\infty,\infty)$ is the time-evolution operator adiabatically connecting the interacting and non-interacting ground-state (see Ref. [19] for details). The denominator of (1.25) cancels all disconnected diagrams. In the following we will not rewrite it explicitly, presuming that all Green's functions are connected. All operators appearing in (1.25) are interaction picture operators w.r.t. H_I^{ph}, i.e. Heisenberg picture operators w.r.t. $\tilde{H}$.

To shorten notations, we introduce electron-hole operators:

$$B_{\mathbf{q}}^\dagger = \sum_{\mathbf{p}} M_{\mathbf{q}} a_{\mathbf{p}+\mathbf{q}}^\dagger b_{\mathbf{p}} \ , \qquad B_{\mathbf{q}} = \sum_{\mathbf{p}} M_{\mathbf{q}} b_{\mathbf{p}}^\dagger a_{\mathbf{p}+\mathbf{q}} \ . \tag{1.26}$$

We can think of $B_{\mathbf{q}}^\dagger$ as the creation operator for one quantum of polarization with fixed momentum $\mathbf{q}$.

Since H_I^{ph} contains only single photon operators, the lowest contribution to (1.25) arises from second order. Therefore, we arrive at:

$$iD_c(\mathbf{q},t) \simeq iD_c^{(0)}(\mathbf{q},t) + \tag{1.27}$$
$$\frac{1}{2}\int_{-\infty}^{\infty} dt_1 dt_2 \, \langle 0|\hat{T}\left\{\left(\sum_{\mathbf{q}_1} B_{\mathbf{q}_1}^\dagger c_{\mathbf{q}_1} - c_{\mathbf{q}_1}^\dagger B_{\mathbf{q}_1}\right)(t_1)\left(\sum_{\mathbf{q}_2} B_{\mathbf{q}_2}^\dagger c_{\mathbf{q}_2} - c_{\mathbf{q}_2}^\dagger B_{\mathbf{q}_2}\right)(t_2)\ c_{\mathbf{q}}(t)c_{\mathbf{q}}^\dagger(0)\right\}|0\rangle \ .$$

Since the $B_{\mathbf{q}}$ and $c_{\mathbf{q}}$ operators always commute, the time ordering factorizes. Furthermore, we can use the fact that

$$\hat{T}\left\{B_{\mathbf{q}}^\dagger(t_1)B_{\mathbf{q}}(t_2)\right\} = \hat{T}\left\{B_{\mathbf{q}}(t_2)B_{\mathbf{q}}^\dagger(t_1)\right\} \ , \tag{1.28}$$

since the B-operators are quadratic in fermion operators. Then, application of Wick's theorem on (1.27) results in:

$$iD_c(\mathbf{q},t) \simeq iD_c^{(0)}(\mathbf{q},t) + \int_{-\infty}^{\infty} d_{t_1} dt_2 \, \langle 0|\hat{T}\left\{B_{\mathbf{q}}(t_2)B_{\mathbf{q}}^\dagger(t_1)\right\}|0\rangle \, D(\mathbf{q},t-t_2)D(\mathbf{q},t_1) \ . \tag{1.29}$$

Since our Hamiltonian is time-independent, all quantities can only depend on the time difference. Thus, taking the Fourier-transform of (1.29), and using the fact that the time integrals are just a double convolution, we obtain:

$$iD_c(\mathbf{q},\Omega) \simeq iD_c^{(0)}(\mathbf{q},\Omega) + \left(D_c^{(0)}(\mathbf{q},\Omega)\right)^2 \cdot \int dt \exp(i\Omega t)\, \langle 0|\hat{T}\left\{B_{\mathbf{q}}(t)B_{\mathbf{q}}^\dagger(0)\right\}|0\rangle \ . \tag{1.30}$$

With help of the Dyson equation we can identify the proper self-energy:

$$\Pi(\mathbf{q},\Omega) = -i \int dt \exp(i\Omega t)\, \langle 0|\hat{T}\left\{B_{\mathbf{q}}(t)B_{\mathbf{q}}^\dagger(0)\right\}|0\rangle \ . \tag{1.31}$$

The expression (1.31) is a Kubo-type formula, and corresponds to linear response in the photon field.

$\Pi(\mathbf{q},\Omega)$ has the following crucial property: it is automatically retarded, i.e.

$$\Pi(\mathbf{q},\Omega) = \Pi^R(\mathbf{q},\Omega) \ . \tag{1.32}$$

This is easily seen in the time-domain, considering:

$$\Pi(\mathbf{q},t) = -i\,\langle 0|\hat{T}\left\{B_{\mathbf{q}}(t)B_{\mathbf{q}}^\dagger(0)\right\}|0\rangle = -iM_{\mathbf{q}}^2 \sum_{\mathbf{p}_1,\mathbf{p}_2} \langle 0|\hat{T}\left\{b_{\mathbf{p}_1}^\dagger(t)a_{\mathbf{p}_1+\mathbf{q}}(t)a_{\mathbf{p}_2+\mathbf{q}}^\dagger(0)b_{\mathbf{p}_2}(0)\right\}|0\rangle \tag{1.33}$$

$$= -i\theta(t) \ \cdot \ M_{\mathbf{q}}^2 \sum_{\mathbf{p}_1,\mathbf{p}_2} \langle 0|b_{\mathbf{p}_1}^\dagger(t)a_{\mathbf{p}_1+\mathbf{q}}(t)a_{\mathbf{p}_2+\mathbf{q}}^\dagger(0)b_{\mathbf{p}_2}(0)|0\rangle \ .$$

In the second line we used the fact that the noninteracting vacuum $|0\rangle$ has a filled VB, s.t. $b_{\mathbf{p}}^\dagger|0\rangle$ vanishes. It is well known that the Fourier-transform of a function which only has support on the positive semiaxis in the time domain is analytic in the upper half plane in the frequency domain, i.e. is retarded (Titchmarsh's theorem, c.f. Ref. [20]).

We can relate the self-energy $\Pi(\mathbf{q},\Omega)$ to the optical susceptibility of the QW, $\chi(\mathbf{q},\Omega)$. One has

$$\epsilon(\mathbf{q},\Omega) = 1 + 4\pi\chi(\mathbf{q},\Omega) \ , \tag{1.34}$$

where $\epsilon(\mathbf{q},\Omega)$ is the QW optical dielectric function. Starting from Maxwell's equations one can show (c.f. Ref. [21], section 2.10.) that in a homogeneous system with dielectric function $\epsilon(\mathbf{q},\Omega)$ the photon Green's function must be modified as:

$$D_c(\mathbf{q},\Omega) = \frac{1}{\sqrt{\epsilon(\mathbf{q},\Omega)}\cdot\Omega - \omega_{\mathbf{q}} + i0^+} \ . \tag{1.35}$$

Equating (1.35) with (1.23) results in:

$$\epsilon(\mathbf{q},\Omega) = \left(1 - \frac{\Pi(\mathbf{q},\Omega)}{\Omega}\right)^2 \ . \tag{1.36}$$

However, in the derivation of $\Pi(\mathbf{q},\Omega)$ we only kept terms to second order in the matter-light coupling constant $M_{\mathbf{q}}$. To be consistent, when taking the square on the right hand side of (1.36), only the linear term $\Pi(\mathbf{q},\Omega)$ is kept. Comparing with (1.34), we obtain:

$$\chi(\mathbf{q},\Omega) \simeq -\frac{\Pi(\mathbf{q},\Omega)}{2\pi\Omega} \ . \tag{1.37}$$

The QW absorption coefficient $\alpha(\mathbf{q},\omega)$ is proportional to $\Im[\chi(\mathbf{q},\Omega)]$. Therefore we have

$$A(\mathbf{q},\Omega) := -\Im\left[\Pi(\mathbf{q},\Omega)\right] \sim \alpha(\mathbf{q},\Omega) \tag{1.38}$$

for Ω close to E_G. In the following we will leave out the prefactors and just refer to $A(\mathbf{q},\Omega)$ as the absorption.

To summarize: The absorption is proportional to the imaginary part of the photon self-energy.

1.5. Wannier-excitons

We will now review the calculation of $\Pi(\mathbf{q},\Omega)$ in the regime where $-E_G < \mu < 0$. For $V(\mathbf{p}-\mathbf{k})$ we assume a quasi-2D Coulomb interaction (see Ref. [22], section 7.3):

$$V(\mathbf{p}-\mathbf{k}) = -\frac{2\pi e^2}{|\mathbf{p}-\mathbf{k}|\epsilon_0} \ , \tag{1.39}$$

where ϵ_0 is the QW dielectric constant. For GaAs $\epsilon_0 \simeq 13$ (static).

Applying perturbation theory in $V(\mathbf{q})$ analogously to (1.25), we can compute $\Pi(\mathbf{q},t)$. In zeroth order in the interaction Wick's theorem gives:

$$\Pi^{(0)}(\mathbf{q},t) = -iM_{\mathbf{q}}^2 \sum_{\mathbf{p}} G_c^{(0)}(\mathbf{p}+\mathbf{q},t) G_v^{(0)}(\mathbf{p},-t) \ . \tag{1.40}$$

Here, $G_c^{(0)}, G_v^{(0)}$ are bare time-ordered Green's functions for the CB and VB, respectively, defined in the standard way. Fourier-transformation yields:

$$\Pi^{(0)}(\mathbf{q},\Omega) = -iM_{\mathbf{q}}^2 \sum_{\mathbf{p}} \int_{-\infty}^{\infty} \frac{d\omega}{2\pi} G_c^{(0)}(\mathbf{p}+\mathbf{q},\Omega+\omega) G_v^{(0)}(\mathbf{p},\omega) \ . \tag{1.41}$$

The corresponding Feynman-diagram is shown in Fig. 1.5. We will call this object an electron-hole bubble.

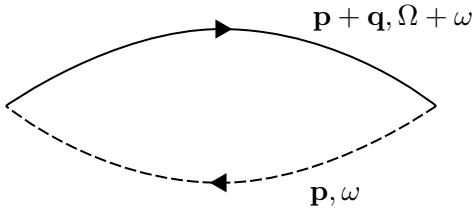

Figure 1.5.: Zeroth order electron-hole bubble. Full lines represent CB electrons, dashed lines VB electrons.

We now use the standard formula:

$$G_c^{(0)}(\mathbf{k},\omega) = \frac{1-n_F(\omega)}{\omega-\epsilon_{\mathbf{k}}+i0^+} + \frac{n_F(\omega)}{\omega-\epsilon_{\mathbf{k}}-i0^+} = \frac{1-n_F(\epsilon_{\mathbf{k}})}{\omega-\epsilon_{\mathbf{k}}+i0^+} + \frac{n_F(\epsilon_{\mathbf{k}})}{\omega-\epsilon_{\mathbf{k}}-i0^+} \tag{1.42}$$

$$= \frac{1}{\omega-\epsilon_{\mathbf{k}}+i0^+\mathrm{sign}(\epsilon_{\mathbf{k}}-\mu)} \ , \tag{1.43}$$

where the second equality holds since $i0^+$ is infinitesimal. n_F is the Fermi occupation function

$$n_F(\omega) \overset{T\to 0}{=} \theta(\mu - \omega) \ . \tag{1.44}$$

A formula analogous to (1.42) holds for the VB.

For our choice of μ, we have

$$n_F(\epsilon_{\mathbf{k}}) = 0 \ , \qquad n_F(-E_{\mathbf{k}} - E_G) = 1 \qquad \text{for all wavevectors } \mathbf{k}. \tag{1.45}$$

One can show that as long as (1.45) is true the second order photon self-energy is exact, since higher orders will just produce multiples of it. (c.f. Ref. [15], page 203, Ref. [21], section 4.6.3).

Proceeding, (1.41) reads:

$$\Pi^{(0)}(\mathbf{q}, \Omega) = -iM_{\mathbf{q}}^2 \sum_{\mathbf{p}} \int_{-\infty}^{\infty} \frac{d\omega}{2\pi} \frac{1}{\Omega + \omega - \epsilon_{\mathbf{p}+\mathbf{q}} + i0^+} \cdot \frac{1}{\omega + E_{\mathbf{p}} + E_G - i0^+} \ . \tag{1.46}$$

Closing the contour below yields

$$\Pi^{(0)}(\mathbf{q}, \Omega) = M_{\mathbf{q}}^2 \sum_{\mathbf{p}} \frac{1}{\Omega - E_{\mathbf{p}} - E_G - \epsilon_{\mathbf{p}+\mathbf{q}} + i0^+} \ , \tag{1.47}$$

which is proportional to the resonant part of the optical susceptibility for free carriers (see Ref. [22], formula 5.62). The corresponding absorption then reads:

$$A^{(0)}(\mathbf{q}, \Omega) = \pi M_{\mathbf{q}}^2 \sum_{\mathbf{p}} \delta(\Omega - E_{\mathbf{p}} - E_G - \epsilon_{\mathbf{p}+\mathbf{q}}) \ . \tag{1.48}$$

This expression is recognized as Fermi's Golden Rule for the transition rate of the photon absorption, which does not take into account the final state interaction. We can further evaluate (1.48) by writing:

$$E_{\mathbf{p}} + E_G + \epsilon_{\mathbf{p}+\mathbf{q}} = E_G + \frac{1}{2m_r}(\mathbf{p} + \frac{m_r}{m}\mathbf{q})^2 + \frac{1}{2M_+}q^2 \ , \tag{1.49}$$

where m_r is the reduced mass and $M_+ = m + M$. Switching to an an integration in (1.48) and shifting the integration variable we obtain:

$$A^{(0)}(\mathbf{q}, \Omega) = \frac{\gamma_{\mathbf{q}}\pi\rho}{1+\beta} \cdot \theta\left(\Omega - E_G - \frac{1}{2M_+}q^2\right) \ , \tag{1.50}$$

where

$$\rho = \frac{m}{2\pi} \tag{1.51}$$

is the single spin DOS in 2D,

$$\beta = \frac{m}{M} \tag{1.52}$$

is the mass ratio, and

$$\gamma_{\mathbf{q}} = M_{\mathbf{q}}^2 \cdot \mathcal{S} \tag{1.53}$$

is effective light-matter coupling strength. The additional factor of $\mathcal{S}$ in the definition of $\gamma_{\mathbf{q}}$ came from changing to a momentum integral. $\gamma_{\mathbf{q}}$ stays finite in the thermodynamic limit.

We will always work under the assumption that β is small, taking into account the leading terms in β only. Thus, we will approximate the prefactor $1/(1+\beta) \simeq 1$ in (1.50).

The interpretation of $A^{(0)}(\mathbf{q}, \Omega)$ is transparent: As soon as the photon energy is larger than sum of the gap and the center of mass energy of an electron hole pair with momentum $\mathbf{q}$, the absorption sets in, and is proportional to the DOS of the CB which measures the phase space of available states.
Let us now derive $\Pi(\mathbf{q}, \Omega)$ in higher orders. We will only sketch the most important steps. Details can be found in Ref. [21], chapter 9.22 - in 3D, but the calculation in 2D is analogous. We use a diagrammatic evaluation. One can show that the only diagrams contributing to $\Pi(\mathbf{q}, \Omega)$ are the so-called ladder diagrams, as drawn in Fig. 1.6.

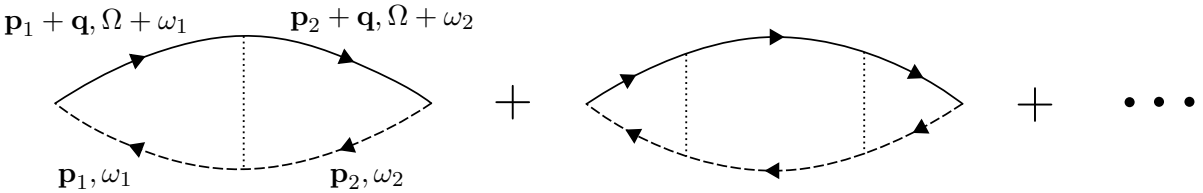

Figure 1.6.: The series of ladder diagrams. Dotted lines represent the Coulomb interaction.

All other diagrams (especially all self-energy diagrams) vanish for the following reason: In the time domain, all non-ladder diagrams either contain CB electrons propagating backwards in time or VB electrons propagating forwards in time. The bare Green's functions in the time domain read:

$$G_c^{(0)}(\mathbf{k}, t) = -i\left[\theta(t) - n_F(\epsilon_{\mathbf{k}})\right] \exp\left(-i\epsilon_{\mathbf{k}} t\right) \tag{1.54}$$

$$G_v^{(0)}(\mathbf{k}, t) = -i\left[\theta(t) - n_F(-E_{\mathbf{k}} - E_G)\right] \exp\left(-i\left(-E_{\mathbf{k}} - E_G\right) t\right) \ . \tag{1.55}$$

Thus, because of the condition for the Fermi-functions (1.45):

$$t < 0 \ \Rightarrow \ G_c(\mathbf{k}, t) \sim n_F(\epsilon_{\mathbf{k}}, t) = 0 \tag{1.56}$$

$$t > 0 \ \Rightarrow \ G_v(\mathbf{k}, t) \sim 1 - n_F(-E_{\mathbf{k}} - E_G, t) = 0 \ . \tag{1.57}$$

An example for a CB-self-energy diagram that is absent due to the condition (1.57) is shown in Fig. 1.7.

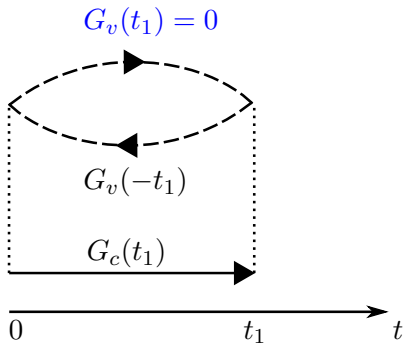

Figure 1.7.: Vanishing CB self-energy diagram. For $t_1 > 0$, the VB Green's function shown in blue is zero.

One can sum the whole series of ladder diagrams by introducing an auxiliary function $P_{\mathbf{q}}(\mathbf{r}, \Omega + i0^+)$ s.t.

$$\Pi(\mathbf{q}, \Omega) = \gamma_{\mathbf{q}} P_{\mathbf{q}}(\mathbf{r} = 0, \Omega + i0^+) \ . \tag{1.58}$$

$P_{\mathbf{q}}(\mathbf{r}, \Omega + i0^+)$ is related to the vertex function. Starting from a Bethe-Salpeter-type integral equation one can then write down a differential equation for $P_{\mathbf{q}}(\mathbf{r}, \Omega + i0^+)$:

$$\left(\Omega + i0^+ - E_G - \frac{q^2}{2M_+} - H_H\right) P_{\mathbf{q}}(\mathbf{r}, \Omega + i0^+) = \delta(\mathbf{r}) \tag{1.59}$$

$$H_H = -\frac{1}{2m_r}\nabla_{\mathbf{r}}^2 - \frac{e^2}{\epsilon_0 r} \ .$$

H_H is recognized as the Hamiltonian for the relative motion in a Hydrogen atom. The eigenfunctions $\phi_n(\mathbf{r})$ of H_H are known:

$$H_H \phi_n(\mathbf{r}) = \epsilon_n \phi_n(\mathbf{r}) \ . \tag{1.60}$$

This eigenfunction-equation is referred to as *Wannier equation*. Expanding in the eigenfunctions, one obtains a solution for $P_{\mathbf{q}}$ and, therefore, also for $\Pi(\mathbf{q}, \Omega)$:

$$\Pi(\mathbf{q}, \Omega) = \gamma_{\mathbf{q}} \sum_n \frac{|\phi_n(0)|^2}{\Omega - E_G - q^2/2M_+ - \epsilon_n + i0^+} \ . \tag{1.61}$$

The summation extends over all eigenstates, i.e. over bound and scattering states. The bound states are commonly called *Wannier-excitons*.

In comparison to the free carrier susceptibility (1.47), formula (1.61) shows a redshift of the excitation energies due to the formation of Hydrogen-like bound states. In addition, it contains the factors $|\phi_n(\mathbf{r} = 0)|^2$. Since $\mathbf{r}$ is the relative position of CB electron and VB hole, this factor describes the probability to create an electron-hole pair at the same point, which is required for photon absorption.

The bound state energies ϵ_n, counted from $E_G + q^2/2M_+$, fulfill the relation:

$$E_n = -E_0 \cdot \frac{1}{(n + 1/2)^2} \ , \qquad E_0 = \frac{e^4 m_r}{2\epsilon_0^2} = \frac{1}{2m_r a_0^2} \ . \tag{1.62}$$

The lowest (1s) exciton has an energy of $-4E_0$, where $E_0 \simeq 4$ meV for GaAs (see Ref. [22], Fig. 10.1). a_0 is the (3D)-excitonic Bohr radius:

$$a_0 = \frac{\epsilon_0}{me^2} + \mathcal{O}(\beta) \ . \tag{1.63}$$

For GaAs $a_0 \simeq 13$ nm.

For a two-dimensional description to be valid, the width of the QW d should be smaller than a_0.

Inserting the 2D hydrogenic wavefunctions into (1.61), one can obtain the absorption $A(\mathbf{q}, \Omega)$ from (1.61). This results in an expression known as *2D Elliott formula*. We will not give it here, for details see Ref. [22], formula (10.110). A plot of $A(\mathbf{q}, \Delta)$ as a function of the normalized detuning

$$\Delta = \frac{\Omega - E_G - \frac{q^2}{2M_+}}{E_0} \tag{1.64}$$

is shown in Fig. 1.8, where we have only kept the three lowest bound states and used a finite damping to highlight the exciton poles.

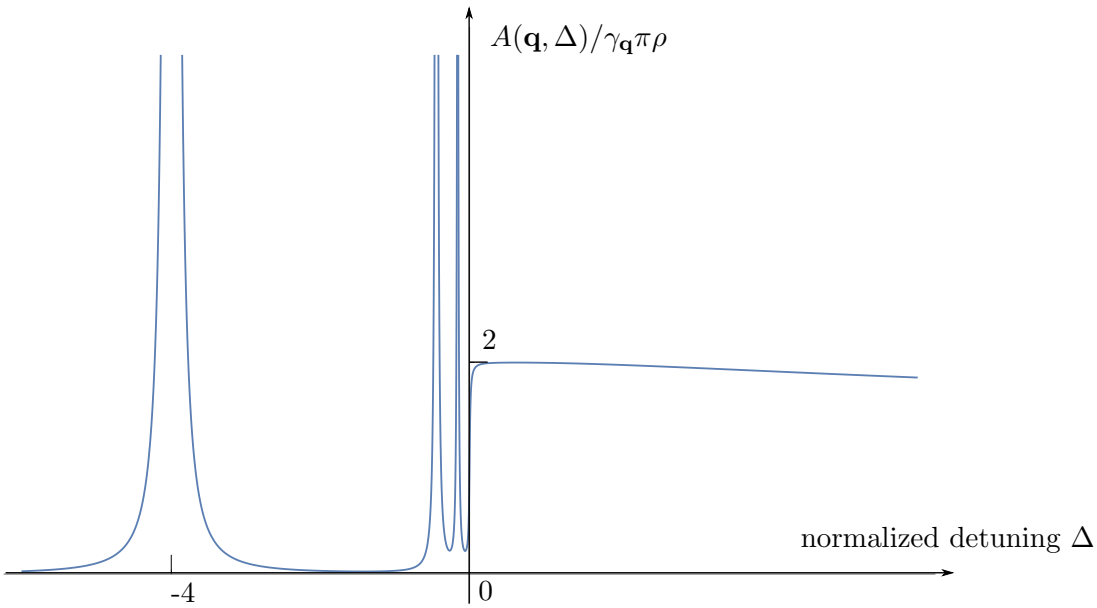

Figure 1.8.: Absorption in the Wannier-exciton regime. The lowest bound state ($n = 0$) appears broader due to it's enhanced weight, which scales as $1/(n + 1/2)^3$.

Besides the pole structure Fig. 1.8 also shows an increase by a factor of 2 at the onset of the continuum absorption (compare with (1.50)), which can be seen as a residue of the excitonic enhancement.

1.6. Exciton-polaritons

Having obtained the photon-self-energy (1.61), we can also calculate the polariton dispersion. Of the sum in (1.61) we only keep the 1s-exciton ($n = 0$), meaning that the

cavity mode is tuned close to the 1s-exciton resonance. Furthermore, the weight of the higher-order bound states is sizably smaller. Thus, we consider a two-oscillator model. In the limit of infinite exciton and photon lifetime, we can simply insert the $n = 0$ contribution into (1.23). The eigenenergies of the resulting *exciton-polaritons* can then be found by solving for the zeros of the denominator. This gives a quadratic equation, with the solutions:

$$\Omega_\pm = \frac{1}{2}\left(\omega_\mathbf{q} + e_\mathbf{q} \pm \sqrt{(\omega_\mathbf{q} - e_\mathbf{q})^2 + 4g_{\mathrm{ep}}^2(\mathbf{q})}\right) , \tag{1.65}$$

where

$$e_\mathbf{q} = E_G + \frac{q^2}{2M^+} - 4E_0 \tag{1.66}$$

is the exciton dispersion, and

$$g_{\mathrm{ep}}(\mathbf{q}) = \sqrt{\gamma_\mathbf{q}}|\phi_0(0)| \tag{1.67}$$

is the exciton-photon coupling. To have two well resolved polariton branches, $2g_{\mathrm{ep}}(\mathbf{q})$ must be larger than both the cavity linewidth Γ_c and the exciton linewidth. This constitutes the so-called *strong coupling regime*. In this regime we can think of the photon as being absorbed and reemitted by the QW and reflected by the mirrors several times, s.t. the notion of the polariton as a new quasiparticle is really justified.

Let us now recall the cavity photon dispersion (1.7):

$$\omega_\mathbf{q} \simeq \omega_0 + \frac{\mathbf{q}^2}{2m_{\mathrm{cav}}} .$$

with $m_{\mathrm{cav}} \simeq 10^{-5} m_0$, while $M^+ \simeq M \simeq 0.5 m_0$. Therefore, in comparison to the photon, the exciton is practically dispersionless. In addition, as can be seen from formulas (1.7), (1.14) ff., also the $\mathbf{q}$-dependence of $g_{\mathrm{ep}}(\mathbf{q})$ is weak. Thus, it is justified to set $\mathbf{q} = 0$ in the calculation of the photon self-energy $\Pi(\mathbf{q}, \omega)$. We will do so in the following, effectively considering only vertical VB-CB transitions.

We now introduce the detuning δ of the cavity mode from the exciton mode:

$$\delta = \omega_0 - e_0 . \tag{1.68}$$

Using this notation, Fig 1.9 shows a plot of the polariton and bare cavity and exciton dispersions, with $e_\mathbf{q} \simeq e_0$ and $g_{\mathrm{ep}}(\mathbf{q}) \simeq g_{\mathrm{ep}}(0) =: g_{\mathrm{ep}}$.

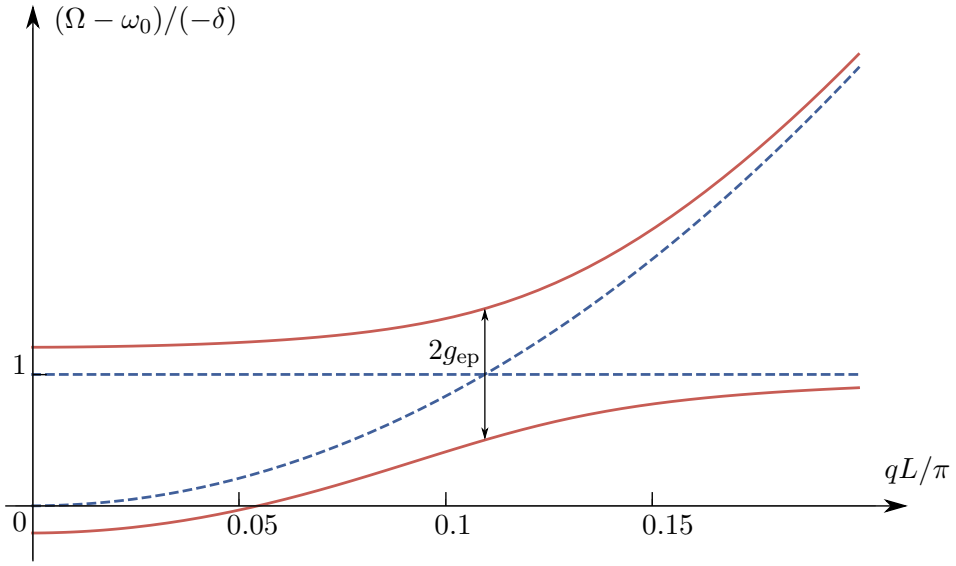

Figure 1.9.: Dispersion of the exciton-polariton. Blue dashed curves show bare cavity and exciton dispersions, red curves show polariton dispersions. Used parameters: $\delta/\omega_0 = -0.006$, $\delta/g_{\mathrm{ep}} = -2$.

One can see that at small momenta the upper polariton-branch approaches the exciton-branch, while at larger momenta it approaches the photon branch. Thus, the upper polariton is exciton-like for small momenta, and light-like for large momenta. For the lower polariton one has the opposite behaviour. This is often made explicit by so called *Hopfield coeffcients*, measuring the effective light and matter content of the polaritons. In the simple exciton-polariton case, these can be found by introducing polariton operators as linear combination of photon and exciton operators (c.f. Ref. [22], page 203ff.).

A further discussion of polariton properties in combination with experimental results in a different regime of Fermi energy will be presented in chapter 5. A detailed review on exciton-polaritons can be found in Ref. [23].

1.7. The Fermi-edge regime: experimental motivation

The well-established theory of microcavity exciton-polaritons discussed in the preceeding sections is fairly simple due to the absence of a Fermi sea dynamically responding to the excitons. As soon as the Fermi sea is populated, which is the case for n-doped semiconductors, the nature of excitons and polaritons will change. For very weak dopings the exciton can bind an additonal CB electron, resulting in so-called *trions*. We will not further consider this regime; a very recent theoretical study is presented in Ref. [24].

If the Fermi-energy is well above the bottom of the CB, further changes can be expected due to the strong response of the Fermi sea. This situation is found in two recent experiments conducted by Gabbay et al. [5] (2007) and Smolka et al. [1] (2014), where the CB was populated strongly. Taking Ref. [1] (see supplementary material) as an example, this can be achieved in two steps:

First, to insert free carriers in the CB, the system is n-doped. To reduce the impurity scattering, not the QW itself is doped, but a layer which is spatially separated. This

procedure is called *modulation doping* (compare also Ref. [25], section 11.3.4). The impurity-density of the QW can be indirectly characterized via the electron mobility. One can qualitatively distinguish two cases: Low-mobility samples have a high-impurity concentration, and vice versa. Since the mobility scales as one over mass (c.f. Ref. [26], page 601ff.), in low-mobility samples we can qualitatively assume the hole mass to be infinite, while in high-mobility GaAs samples the mass is assumed to be as in (1.4).

Second, the capping layer of the sample is p-doped. This layer then effectively acts as an electron reservoir. The electron density respectively the Fermi level of the QW can then be tuned applying a voltage between the QW and the capping layer.

The experiments of Refs. [5], [1] measured the properties of polaritons in these heavily doped systems, claiming to reach the strong coupling limit: E.g. in [1] the cavity photon linewidth is given as $\Gamma_c \simeq 1$ meV, while the exciton-photon coupling respectively the polariton splitting is measured to be $2g_{\mathrm{ep}} \simeq 2$ meV.

The resulting so-called *Fermi-edge polaritons* are found to differ drastically from the simple exciton-polaritons. An especially remarkable feature is the strong dependence on the electron mobility accentuated in [1], where a high-mobility and a low-mobility sample were investigated. The measured polariton spectral function as function of energy E and cavity detuning δ (c.f. (1.68)) is shown in Fig. 1.10. A detailed discussion of this measurement will be presented in section 5.2. For now, we will only highlight the main points.

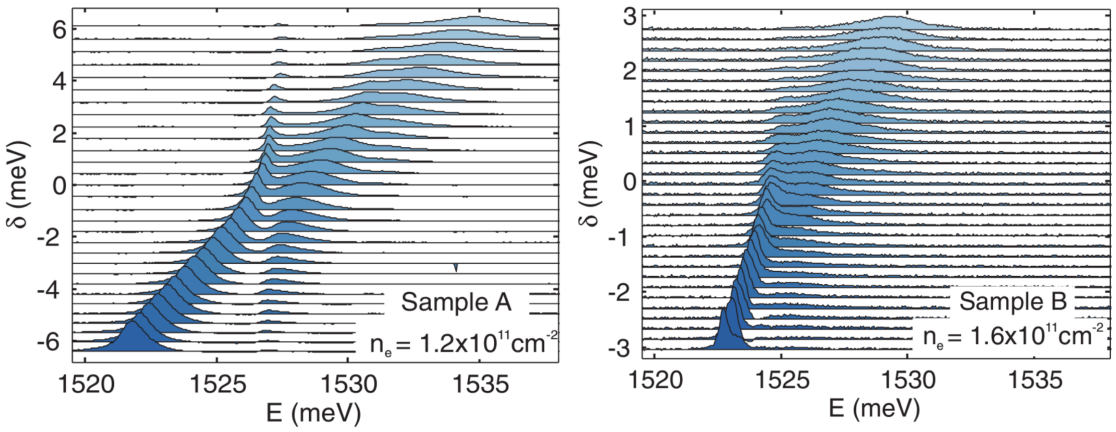

Figure 1.10.: Polariton spectra as function of energy E and cavity detuning δ, measured in Ref. [1]. Left figure: low-mobility sample. Right figure: high-mobility sample. Data shown with courtesy of A. Imamoğlu.

While in the low-mobility sample (left) two clear polariton branches are visible, in the high-mobility sample (right) the polariton-splitting vanishes almost completely. This behaviour can certainly not be explained within the theory of exciton-polaritons (nor with trions), where the mobility respectively hole mass dependence of the polaritons is marginal.

As already qualitatively pointed out in [1], the key origin of this reduced Fermi-edge polariton splitting is the hole recoil, which is absent for infinite mass holes.

1.8. The Fermi-edge regime

To theoretically describe the polariton formation in heavily doped semiconductor microcavities, let us now introduce the **Fermi-edge regime** (FER) of a large Fermi-energy. To be specific, we will regard a setup where the chemical potential μ is much larger than the exciton binding energy E_0:

$$\mu \gg E_0 \ . \tag{1.69}$$

This condition can also be rewritten as:

$$k_F \cdot a_0 \gg 1 \ , \tag{1.70}$$

where k_F is the Fermi-wavevector, and a_0 the excitonic Bohr radius. In this regime, which requires strong doping as discussed on page 26, the semiconductor is called *degenerate*.

By contrast, we call the regime of $\mu \ll E_0$, where excitonic effects are dominant as discussed in the previous sections, the **exciton regime**.

In Ref. [1], $\mu \simeq 4$ meV, which has to be compared to $E_0 = 4$ meV for GaAs. Thus, we can regard this experiment as somewhat inbetween the FER and the exciton regime.

In order to keep the calculations feasible, from now on we will use a simplified model for the interaction. Namely, we will use a contact interaction in real space, i.e. a constant in momentum space. The calculations below will show that in the FER the dominant contributions to all observables will arise from momenta close to k_F. Therefore, we will use the following interaction Ansatz:

$$V(\mathbf{q}) \simeq V(k_F) \simeq -\frac{2\pi e^2}{\epsilon_0(k_F + \kappa)} = -V_0 \ , \tag{1.71}$$

where κ is the 2D screening wave-vector. In the static Lindhard-Ansatz, $\kappa \sim 1/a_0$, s.t. we can actually disregard it as compared with k_F.

It should be noted that the assumption of a purely 2D screening is a pretty rough approximation - there will always be screening from layers outside the QW, which will effectively reduce the value of V_0.

We will further assume that the interaction is cut off at energies $\epsilon_{\mathbf{k}} = \mu + \xi$, where $\xi = \mathcal{O}(\mu)$. Typically, $\mu + \xi$ is of order of the CB bandwidth. The special case of $\mu = \xi$ corresponds to half filling.

To summarize, the energy scales under consideration are:

$$E_0 \ll \mu, \xi \ll E_G \ . \tag{1.72}$$

A sketch of the bandstucture in the FER is shown in Fig. 1.11.

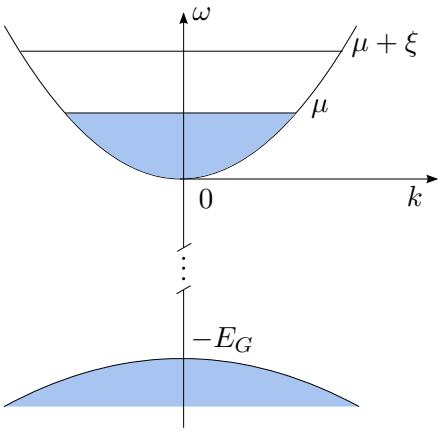

Figure 1.11.: 1D projection of the bandstructure in the FER.

Of course, the requirement of a large chemical potential is actually best fulfilled in metals. For these, a type of problem close in spirit to our study is the *x-ray-edge problem*: One considers the process where an electron is lifted from a core level of the atom to the conduction band. The required energies are usually in the (soft) x-ray regime, hence the name. The empty electronic state of the core shell can also be regarded as a hole, which is very localized; therefore, in the x-ray-edge problem it is meaningful to regard the hole mass as infinite.

1.9. Statement of the problem

We are now in a position to formulate the aim of this thesis: To obtain a qualitative understanding of the results found in Ref. [1], we will study two-dimensional microcavity polaritons in the FER, concentrating on finite hole masses. To our knowledge, this problem was not yet considered in the literature in full detail. Our study has the following structure:

- To obtain insights in the physics of hole recoil, we will first calculate the VB hole Green's function in the FER, using perturbative techniques. We will especially elucidate the influence of particle-hole scattering phase-space on the shape of the VB hole spectral function, studying it for vanishing and large momenta.
- We will use the results of the first step as an input to compute the photon self-energy in linear resonse, making use of the extensive literature on the x-ray-edge problem. Our main technical tool will be the leading-log approximation suggested by Mahan [6] and Nozières [7], [27]. Our study will focus on frequencies close to the optical threshold. The physical implications of a finite hole mass will be clarified, and the validity of our theory will be outlined.
- As the final step, we will then compute the FER finite mass polariton spectral function, discussing the physical requirements for polariton formation. We will also compare our results to the findings of Ref. [1].
- As a supplement, we sketch a way to go beyond the FER analytically, which we have not completed yet.

Our theory does not allow for a detailed quantitative explanation for the outcome of Ref. [1]: First of all, we will use relatively rough approximations, and our results can thus only indicate trends. Second, the experiment in Ref. [1] does not correspond to a clear theoretical parametric regime, as was outlined in the previous section. This is also the case for the effective dimensionality: As noted in section 1.5, a purely two-dimensional description requires that the width of the sample d is much smaller than the excitonic Bohr radius a_0. In Ref. [1] $d = 20$ nm as compared to $a_0(\mathrm{GaAs}) \simeq 13$ nm, which means that the system is neither in 2D nor in 3D.

However, because the basic features of polaritons will be found to be weakly dependent on space dimensions, our study can still reproduce some fundamental findings of Ref. [1] qualitatively.

2. The hole propagator in the Fermi-edge regime

In preparation of the evaluation of the FER photon self-energy in the next chapter, we will now calculate a simpler quantity, which will already give us useful physical insights: the VB hole propagator D.

In the Wannier-exciton case discussed in section 1.5, this propagator was a simple free particle propagator, since all self-energy diagrams vanished. In the FER, however, the interaction with the CB electrons will significantly alter the form of D, as will be shown below.

In this chapter only we will switch from VB electron to VB hole operators. This involves the following standard replacements (we use d's for CB hole operators):

$$b_{\mathbf{k}} \;\rightarrow\; d^{\dagger}_{-\mathbf{k}} \;, \qquad\qquad b^{\dagger}_{\mathbf{k}} \;\rightarrow\; d_{-\mathbf{k}} \;. \tag{2.1}$$

In addition a VB hole with momentum $\mathbf{k}$ has the energy $E_G + E_{\mathbf{k}}$.

Since a hole is just a missing electron, the Fermi function of holes n^h_F in the FER fulfills:

$$n^h_F(E_{\mathbf{k}} + E_G) = 1 - n_F(-E_{\mathbf{k}} - E_G) = 0 \;, \tag{2.2}$$

where we used that the unexcited VB is completely filled. In terms of the hole operators, our quantity of interest in this chapter will be:

$$D(\mathbf{Q}, t) = -i \,\langle 0|\hat{T}\left\{ d_{\mathbf{Q}}(t) d^{\dagger}_{\mathbf{Q}}(0)\right\}|0\rangle \;\; . \tag{2.3}$$

Since we will be interested in the absorption later on, we average over the state $|0\rangle$, i.e. the noninteracting ground-state of the system without CB or VB holes.

It is easily seen that

$$D(\mathbf{Q}, t) \sim \theta(t) \;, \tag{2.4}$$

s.t. the VB hole Green's function is automatically retarded.
It should further be noted that the CB electron propagator in the Fermi-edge regime still is that of a free particle: the decay rate of CB electrons is proportional to the VB hole density, which is assumed to be zero. Since in the rest of this thesis all appearing CB electron propagators will be bare ones, we will leave out the superscript (0) for them.

An experiment, which in principle can directly measure the hole spectral function $\mathcal{A}_h(\mathbf{Q}, \Omega)$, corresponding to (2.3), is *X-ray photoelectron spectroscopy* (XPS). (see Ref. [21], section 9.3.5.). In XPS, a photon with energies of order of keV is used to excite a VB electron to a very large kinetic energy. The excited electron leaves the sample very fast, and is practically unaffected by the CB Fermi-sea. A measurement of the kinetic energies of the outgoing electrons is therefore directly related to $\mathcal{A}_h(\mathbf{Q}, \Omega)$.

2.1. The hole propagator: infinite mass case

2.1.1. Anderson orthogonality

Following the literature (c.f. Refs. [21], [28]), we will start from the calculation of the propagator of an immobile hole, i.e. $M = \infty$. This means that the hole dispersion is completely flat, and hole operators do not have a momentum quantum number.

In the infinite mass case, the hole propagator was calculated by many authors as byproduct of the absorption in the x-ray-edge problem. A short overview over these works will be presented in section 3.1.

Let us now write down the Hamiltonian H_∞ for the CB-VB system (without photons). For physical transparence, we will phrase the interaction term as a contact potential in real space. Thus, starting from H^{CV} as defined in (1.21), our ($M = \infty$) - Hamiltonian reads:

$$H_\infty = E_G d^\dagger d + \sum_{\mathbf{k}} \epsilon_{\mathbf{k}} a^\dagger_{\mathbf{k}} a_{\mathbf{k}} - V_0 \Psi^\dagger(\mathbf{r}=0)\Psi(\mathbf{r}=0) d^\dagger d \ , \tag{2.5}$$

where Ψ are the CB electron position operators, and we have centered our coordinate system at the position of the hole. We have also left out the constant term corresponding to the filled VB.

The hole operators appear in (2.5) only in the combination $n_d = d^\dagger d$, which is the hole number operator. Since a hole is a fermion, n_d can have the (eigen-)values 0 or 1. In dependence of the value of n_d, two sectors for the CB electron system can be defined.

In the absence of a hole ($n_d = 0$), there is just the bare CB Fermi-sea without interactions. As soon as a hole is created ($n_d = 1$), it acts as a local potential scatterer for the CB electrons. Thus, the creation of a hole can be seen as a *quantum quench* connecting the two sectors [29].

With the notation

$$\hat{V} = -V_0 \Psi^\dagger(\mathbf{r}=0)\Psi(\mathbf{r}=0) \ , \tag{2.6}$$

the corresponding electronic Hamiltonian H_∞ for the two sectors reads:

$$H_\infty(n_d = 0) = \sum_{\mathbf{k}} \epsilon_{\mathbf{k}} a^\dagger_{\mathbf{k}} a_{\mathbf{k}} = H_\mathrm{i} \qquad \mathrm{i} \mathrel{\widehat{=}} \text{initial} \tag{2.7}$$

$$H_\infty(n_d = 1) = E_G + \underbrace{\sum_{\mathbf{k}} \epsilon_{\mathbf{k}} a^\dagger_{\mathbf{k}} a_{\mathbf{k}} + \hat{V}}_{=H_\mathrm{f}} \qquad \mathrm{f} \mathrel{\widehat{=}} \text{final} \ . \tag{2.8}$$

These two sectors have different groundstates. We will call them $|0\rangle$ for H_i, and $|G\rangle$ for H_f.

It is interesting to consider the overlap $|\langle 0|G\rangle|$ of these two states. As first shown by Anderson, in the thermodynamic limit it will vanish: The two groundstates are said to show *Anderson orthogonality* [30]. In a simplified way, this intriguing property can be understood as follows (c.f. Ref. [21], section 9.3.3):

For a system consisting of N CB electrons, and considering S-waves only, $|0\rangle$ can be described as an N-dimensional Slater determinant of wave functions of the form

$\sin(kr)/kr$. On the other hand, far from the origin, $|G\rangle$ will consist of an N-dimensional Slater determinant of shifted S-waves of the form $\sin(kr+\delta)/kr$. Here, δ is the small scattering phase shift for one-electron scattering from the hole potential.
One can compute the overlap of these two Slater-determinants. Effectively, it will be proportional to the N-th power of terms which are slightly smaller than 1. As a result, one obtains:

$$|\langle 0|G\rangle| = N^{-\frac{\delta^2}{\pi^2}} \ . \tag{2.9}$$

In the thermodynamic limit, $N \to 10^{23}$, the overlap will therefore vanish.

2.1.2. Heuristic calculation of the hole propagator

Our aim now is to find the time-ordered hole propagator:

$$D(t) = -i\,\langle 0|\hat{T}\{e^{iH_\infty t} d e^{-iH_\infty t} d^\dagger\}|0\rangle = -i\theta(t)\,\langle 0|e^{iH_\infty t} d e^{-iH_\infty t} d^\dagger|0\rangle \ . \tag{2.10}$$

For the second equality, we used that H_∞ conserves the number of holes, and there are no holes in the groundstate $|0\rangle$.

The right hand side of (2.10) has the following operator structure: First, a hole is created. Then, the time-evolution operator $\exp(-itH_\infty)$ acts on a state with one hole ($n_d = 1$). Then, the hole is destroyed again. And finally, the inverse time-evolution operator $\exp(itH_\infty)$ acts on a state without holes ($n_d = 0$). Thus, employing the definitions (2.7), (2.8), we can rewrite $D(t)$ as:

$$D(t) = -i\theta(t) e^{-itE_G}\,\langle 0|e^{iH_\mathrm{i} t} d e^{-iH_\mathrm{f} t} d^\dagger|0\rangle \ . \tag{2.11}$$

Since H_i, H_f do not contain hole operators, in (2.11) we can just commute d with $\exp(-iH_\mathrm{i}t)$, which leads to:

$$D(t) = -i\theta(t) e^{-itE_G}\,\langle 0|e^{iH_\mathrm{i} t} e^{-iH_\mathrm{f} t} d d^\dagger|0\rangle = -i\theta(t) e^{-itE_G}\,\langle 0|e^{iH_\mathrm{i} t} e^{-iH_\mathrm{f} t}|0\rangle \ , \tag{2.12}$$

where we used that $d d^\dagger |0\rangle = (1-n_d)|0\rangle = |0\rangle$.

Following Ref. [29], the behaviour of $D(t)$ can be found in a heuristic manner. Inserting a $\mathbb{1}$ of eigenstates $|n\rangle$ of H_f in (2.12), one obtains:

$$i e^{it(E_G - E_i)} D(t) = \theta(t) \sum_n e^{-iE_n t} |\langle 0|n\rangle|^2 \ , \qquad \text{with } H_i|0\rangle = E_i|0\rangle \ . \tag{2.13}$$

In the long time limit, due to fast oscillations, the only contribution to (2.13) will arise from the term $|\langle 0|G\rangle|^2 \sim N^{-2\delta^2/\pi^2}$ (c.f. (2.9)).

As time increases, the local scattering potential will influence increasing length scales $L(t) \sim v_F t$, where v_F is the Fermi velocity. The effective particle number contributing to the overlap will be proportional to this length: $N \sim L(t)$. As a result, the long time behaviour of $D(t)$ looks like:

$$D(t) \sim t^{-2\frac{\delta^2}{\pi^2}} \ . \tag{2.14}$$

Let us analyse the phase shift δ. For a local scatterer, and for energies close to μ, δ is given by (c.f. [28], formula 25.29)):

$$\delta(\omega \simeq \mu) = \arctan(\pi\rho V_0) \ . \tag{2.15}$$

A useful interpretation of δ is given by the *Friedel sum rule* ([21], section 4.1.3):

According to this rule, δ/π can be seen as the displaced charge (in units of e), which is moved by the scattering potential from infinity to a large, but finite sphere around the scattering site.

The value of the phase-shift is determined by the dimensionless quantity

$$g = \rho V_0 \ . \tag{2.16}$$

In the FER, inserting the definitions for ρ and V_0 (1.71), we have:

$$g \simeq \frac{2\pi e^2}{\epsilon_0 k_F} \cdot \frac{m}{2\pi} = \frac{1}{a_0 \cdot k_F} = \frac{1}{\sqrt{\mu/E_0}} \ll 1 \ , \qquad \text{for} \quad E_0 \ll \mu \ , \tag{2.17}$$

where we also used the definition of the excitonic Bohr radius (1.63).

Thus, we can approximate δ by

$$\delta/\pi = g + \mathcal{O}(g^3) \ . \tag{2.18}$$

In this approximation, (2.14) then reads:

$$D(t) \sim t^{-2g^2} \ . \tag{2.19}$$

To summarize, (2.19) shows a power law singularity originating from the Anderson orthogonality after local quantum quench, induced by photon absorption. Since g can be changed e.g. by modifying the chemical potential, this power law is experimentally tunable. A detailed theoretical study of such a tunable Anderson orthogonality in the context of Kondo physics can be found in Ref. [31], and a experimental realization is presented in Ref. [32].

The preceeding derivation was actually independent of the space dimension except for the definition of g. This is a general feature at ($M = \infty$) for the hole propagator as well as for the absorption: The problems are effecively one-dimensional, and can also be solved by bosonization. This approach was first applied in this context by Schotte and Schotte in Ref. [33]. A summary is found in section 26 VI of Ref. [28]. This effective one-dimensionality will, however, no longer be fulfilled at ($M < \infty$). Thus, we will keep the restriction to 2D in the following.

2.1.3. Linked-cluster calculation of the hole propagator

Having obtained a first hint of $D(t)$, let us now calculate it diagrammatically. We choose the diagrammatic evaluation, because it will allow for a straightforward generalization to finite hole masses M.

We have seen in (2.12), that $D(t)$ is proportional to the factor:

$$\langle 0|e^{iH_\mathrm{i}t}e^{-iH_\mathrm{f}t}|0\rangle = \langle 0|\hat{S}(t)|0\rangle \ , \tag{2.20}$$

with the S-matrix $\hat{S} = e^{iH_\mathrm{i}t}e^{-iH_\mathrm{f}t}$.

With this manipulation we have completely erased the hole propagators from the problem. The only effect of the hole is now to determine when the potential $\hat{V}$ contained in H_f is switched on, namely only for times between 0 and t. We can make this explicit

by attributing a time-dependence to the potential. Switching to momentum space, it then reads:

$$\hat{V}(t_i) = -V_0\theta(t-t_i)\theta(t_i)\frac{1}{\mathcal{S}}\sum_{\mathbf{k}_1,\mathbf{k}_2} a^\dagger_{\mathbf{k}_1}(t_i)a_{\mathbf{k}_2}(t_i) \ . \tag{2.21}$$

With this definition, (2.20) can be summed in exponential form using the linked cluster theorem (see Ref. [21], section 3.6.1): One introduces functions $F_n(t)$ s.t.

$$\langle 0|\hat{S}(t)|0\rangle = \exp\left[\sum_{n=1}^{\infty} F_n(t)\right] \ . \tag{2.22}$$

These functions are shown to be:

$$F_n(t) = \frac{(-i)^n}{n}\int_0^t dt_1 ... \int_0^t dt_n \, \langle 0|T\{\hat{V}(t_1)...\hat{V}(t_n)\}|0\rangle_{dc} \ , \tag{2.23}$$

where the subscript dc means that one only has to sum over topologically different, connected diagrams. As we will see explicitly for the first two terms, in our case these diagrams are closed CB electron loops.

The basic idea of the linked cluster theorem is to count how many copies of a certain connected diagram will appear in a certain order of interaction, and resum these copies in such a form that one only has to evaluate each connected, topologically different diagram once. In spirit this resummation is close to Dyson's equation, and the proof for formula (2.22) is just an exercise in combinatorics. We will see that the relevant contributions F_n are logarithmic, so upon reexponentiation $D(t)$ will be a power law of time. We will restrict ourselves to the calculation of the leading behaviour of this power law in the coupling constant g defined in (2.16).

Let us start the evaluation. To begin with, the zeroth order hole propagator is given by:

$$D^{(0)}(t) = -i\theta(t)e^{-itE_G} \ . \tag{2.24}$$

Then, using (2.23), the first order term in the cluster expansion reads:

$$\begin{aligned} F_1(t) &= -i\int_0^t dt_1 \, \langle 0|\hat{V}(t_1)|0\rangle = \int_0^t V_0 \frac{1}{\mathcal{S}}\sum_{\mathbf{k}_1} G_c(\mathbf{k}_1, 0^-) \\ &= itV_0\frac{1}{\mathcal{S}}\sum_{\mathbf{k}_1} n_F(\epsilon_{\mathbf{k}_1}) = 2itV_0 n \ . \end{aligned} \tag{2.25}$$

where n is the homogeneous CB electron density. In (2.25) we have used the standard rule for the evaluation of equal time Green's functions as well as formula (1.54). The additional factor of 2 came from the spin degree of freedom. Diagrammatically, (2.25) corresponds to a simple CB-electron loop, as shown in Fig. 2.1.

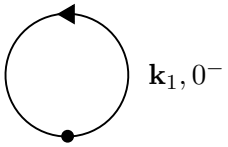

Figure 2.1.: First order CB electron loop. The dot represents the time-dependent potential (2.21).

Upon exponentiation, this term will lead to a linear red-shift of the gap E_G. It can also be seen as change of the total CB Fermi-sea energy in presence of the scattering potential.

We will, however, never try to calculate such shifts of the gap energy, regarding E_G as an experimental parameter. Thus, we will disregard the contribution from $F_1(t)$.

In second order, application of Wick's theorem yields exactly one connected contribution:

$$F_2(t) = -\frac{1}{2\mathcal{S}^2} \sum_{\mathbf{k},\mathbf{k_2}} V_0^2 \int_0^t dt_1 \int_0^t dt_2 \; G_c(\mathbf{k}_1, t_2 - t_1) G_c(\mathbf{k}_2, t_1 - t_2) \; . \tag{2.26}$$

The corresponding diagram is a second order CB loop, shown in Fig. 2.2.

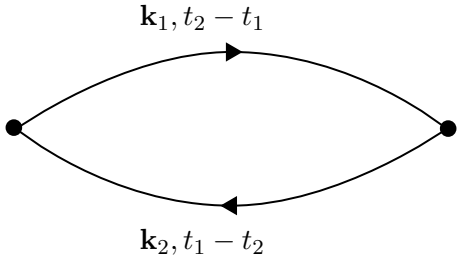

Figure 2.2.: Second order CB electron loop.

Upon inserting $G_c(\mathbf{k}, t)$ from (1.54), the time integrals are easily evaluated, resulting in:

$$F_2(t) = -\frac{V_0^2}{\mathcal{S}^2} \sum_{\mathbf{k}_1\mathbf{k}_2} \left[\frac{it n_F(\epsilon_{\mathbf{k}_1})}{\epsilon_{\mathbf{k}_2} - \epsilon_{\mathbf{k}_1}} - \frac{n_F(\epsilon_{\mathbf{k}_1})(1 - n_F(\epsilon_{\mathbf{k}_2}))}{(\epsilon_{\mathbf{k}_2} - \epsilon_{\mathbf{k}_1})^2} (1 - e^{-it(\epsilon_{\mathbf{k}_2} - \epsilon_{\mathbf{k}_1})}) \right] \; . \tag{2.27}$$

The first summand linear in time again just shifts the gap, and we will disregard it. Let us concentrate on the second term, which we will just call $F_2(t)$ from now on. Relabeling momenta, $\mathbf{k}_1 = \mathbf{p}$, $\mathbf{k}_2 = \mathbf{p} + \mathbf{q}$, it can be rewritten as:

$$F_2(t) = -\int_{-\infty}^{\infty} \frac{1}{\nu^2} N(\nu)(1 - e^{-i\nu t}) d\nu \tag{2.28}$$

$$N(\nu) = \frac{V_0^2}{\mathcal{S}^2} \sum_{\mathbf{p},\mathbf{q}} n_F(\epsilon_{\mathbf{p}})(1 - n_F(\epsilon_{\mathbf{p}+\mathbf{q}})) \delta(\nu + \epsilon_{\mathbf{p}} - \epsilon_{\mathbf{p}+\mathbf{q}}) \; . \tag{2.29}$$

The function $N(\nu)$ has a transparent physical interpretation. It counts the phase space for the following process: A CB electron is scattered by the local VB hole potential, which results in a particle-hole excitation of the CB Fermi sea. Such processes were absent in the Wannier case since the CB was empty. In the FER, however, these will determine the shape of the hole spectral function $\mathcal{A}_h$, as we will see below. It should be noticed, that these excitations necessarily cost energy ($\nu > 0$) due to the structure of the Fermi-functions in (2.29). A sketch of such a process is shown in Fig. 2.3.

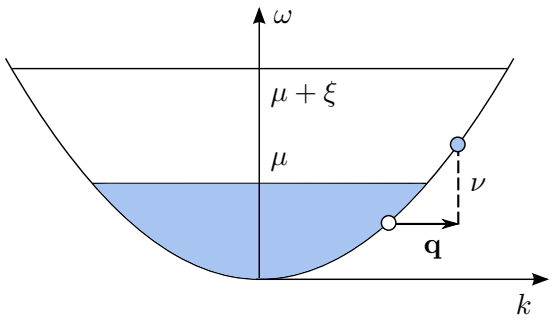

Figure 2.3.: Sketch of a CB particle-hole excitation.

Let us now evaluate $N(\nu)$. Switching to energy integrals, one obtains

$$N(\nu) = 2g^2 \int_{-\mu}^{0} d\epsilon_1 \int_{0}^{\xi} d\epsilon_2 \; \delta(\nu + \epsilon_1 - \epsilon_2) \; , \tag{2.30}$$

where again we got a prefactor of 2 from the spin summation, we used g as defined in (2.16) and the upper cutoff on the interaction ξ.

(2.30) is easily integrated. At low frequencies $N(\nu)$ will be linear in ν, and for frequencies $\nu > \xi$ it will decrease continously, vanishing for $\nu = \xi + \mu$. This behaviour is understood as follows: Increasing the energy, the phase space for scattering increases since there are less final states forbidden by the Pauli principle; for energies above the bandwidth scatterings are not possible anymore. Since the details of the UV cutoff are of no physical relevance, we can then approximate $N(\nu)$ in the following way:

$$N(\nu) = 2g^2 \nu \cdot \theta(\nu) \cdot \theta(\xi - \nu) \; . \tag{2.31}$$

Inserting this into (2.28), we obtain:

$$F_2(t) = -2g^2 \int_{0}^{\xi} \frac{1}{\nu} (1 - e^{-i\nu t}) d\nu \; . \tag{2.32}$$

We notice that $F_2(t)$ has the property

$$F_2(-t) = \overline{F_2(t)} \; , \tag{2.33}$$

which was also the case for the S-matrix, see (2.20). As will be seen below, this property will simplify the evaluation of the hole spectral function $\mathcal{A}_h(\Omega)$. Therefore, we will do approximations in such a way that (2.33) is conserved.

We will now bring $F_2(t)$ in a compact form considering different limits of $|t|$.

First, we consider $|t| \ll 1/\xi$. Then the argument of the exponential will be small, hence one can expand the exponential to first order, which leads to :

$$F_2(t) \simeq -2g^2 it\xi \qquad\qquad |t| \ll 1/\xi \; . \tag{2.34}$$

For $|t| \gg 1/\xi$ one can split the integral into two parts. For $\nu < 1/|t|$ we can again expand the exponential. For for $\nu > 1/|t|$ the exponential will be larger than 1, hence in this region it will oscillate quickly and we can qualitatively ignore it. Together this leads to:

$$\begin{aligned} F_2(t) \simeq -2g^2 i \int_{0}^{1/|t|} d\nu \; t \quad - 2g^2 \int_{1/|t|}^{\xi} d\nu \; \frac{1}{\nu} &= -2g^2 i \cdot \mathrm{sign}(t) - 2g^2 \log(\xi|t|) \\ &\simeq -2g^2 \log(\xi|t|) \qquad t \gg 1/\xi \; . \end{aligned} \tag{2.35}$$

The last line holds with *logarithmic accuracy*, which is the major approximation technique that will be used in this work. In this approximation, one can ignore terms of order of 1 in comparison to terms which are logarithmically divergent.

We note that, inserting the long time form of $F_2(t)$ into (2.20) and (2.10), we obtain:

$$D(t) = -ie^{-iE_G t}(\xi t)^{-2g^2} \qquad t \gg 1/\xi \ , \tag{2.36}$$

coinciding with the heuristic result (2.19).

Let us proceed with the calculation of the hole spectral function $\mathcal{A}_h$. First we notice, that with logarithmic accuracy one can always write:

$$\log(z) \simeq \log(|z|) \qquad \forall z \in \mathbb{C} \setminus \mathbb{R}_0^- \quad s.t. \ |z| \gg 1 \ , \tag{2.37}$$

where we used the principal branch of the logarithm, and the fact that the imaginary part of the complex logarithm is at most 2π.

Employing the approximation (2.37), one can combine the two limits of $F_2(t)$ s.t. the analytic property (2.33) is fulfilled:

$$F_2(t) \simeq -2g^2 \log(1 + it\xi) \ . \tag{2.38}$$

Since $D(t)$ is retarded, we can obtain the spectral function by just taking the imaginary part.

$$\mathcal{A}_h(\Omega) = -2\Im\left[\int_{-\infty}^{\infty} dt \exp(i\Omega t) D(t)\right] = 2\Re\left[\int_0^{\infty} dt \exp\left(i(\Omega - E_G)t\right) \exp\left(F_2(t)\right)\right] \ . \tag{2.39}$$

We now introduce the detuning from the gap ϵ:

$$\epsilon = \Omega - E_G \ . \tag{2.40}$$

In terms of ϵ, and using the property (2.33), we can rewrite (2.39) as

$$\mathcal{A}_h(\epsilon) = \int_{-\infty}^{\infty} dt \exp\left(i\epsilon t\right) \exp\left(F_2(t)\right) \ . \tag{2.41}$$

Inserting the simplified form (2.38), we obtain

$$\mathcal{A}_h(\epsilon) = \int_{-\infty}^{\infty} dt \frac{\exp\left(i\epsilon t\right)}{(1 + it\xi)^{2g^2}} \ . \tag{2.42}$$

This integral can be performed by a contour integration (see page 617 of Ref. [21] for details). The result reads:

$$\mathcal{A}_h(\epsilon) = \theta(\epsilon)\Gamma(1 - 2g^2)\frac{2\sin(2\pi g^2)}{\xi}\frac{\exp(-\epsilon/\xi)}{(\epsilon/\xi)^{1-2g^2}} \ , \tag{2.43}$$

where Γ is the Gamma function. Near the threshold, $\mathcal{A}_h(\epsilon)$ behaves as a power law:

$$\mathcal{A}_h(\epsilon) \sim \frac{1}{\xi} \cdot (\epsilon/\xi)^{2g^2-1} \ . \tag{2.44}$$

With help of identities for Gamma functions, one can check that $\mathcal{A}_h(\epsilon)$ is properly normalized:

$$\int_{-\infty}^{\infty} \frac{d\epsilon}{2\pi} \mathcal{A}_h(\epsilon) = 1 \ . \tag{2.45}$$

Using this property, it is also clear that

$$\lim_{g\to 0} \ \mathcal{A}_h(\epsilon) = 2\pi\delta(\epsilon) \ , \qquad \text{as expected.} \tag{2.46}$$

A plot of $\mathcal{A}_h(\epsilon)$ is shown in Fig. 2.4.

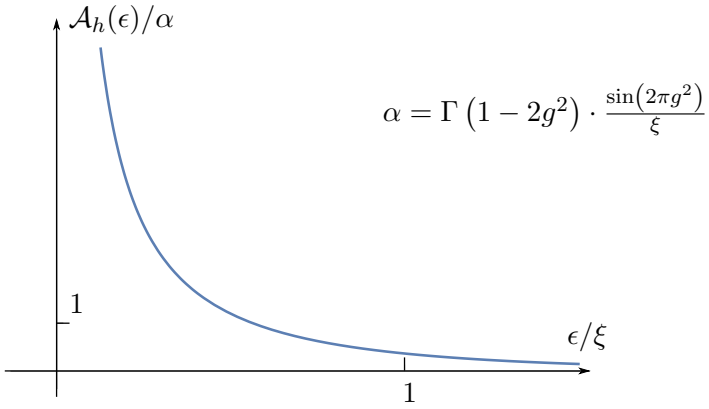

Figure 2.4.: Infinite mass hole spectral function for $g = 0.1$.

Let us restate the most important point: Without interactions, or for $\mu < 0$, the hole spectral function would just be a delta function. In the FER, however, we have particle hole excitations of the CB Fermi-sea, shown in Fig 2.3. Since such excitations are possible at an infinitesimal energy cost, the delta function is turned into a power law for energies larger than E_G.

2.1.4. Dyson equation calculation of the hole propagator

Another possibility to obtain the VB hole propagator is the straightforward use of the Dyson equation. This means that we have to reattach the hole propagators to the electron-loop diagrams discussed so far, and calculate the self-energy.

This method is also implicitly shown in the first two of the seminal three papers on the x-ray-edge problem by Nozieres et al. [7], [8], where also the results of this section can be found.

To be consistent with the calculations done so far, as lowest Ansatz for the VB hole self-energy $\Sigma(\Omega)$ we must use the diagram in the frequency domain corresponding to Fig. 2.2 with reattached hole propagators. The relevant diagram is then shown in Fig. 2.5.

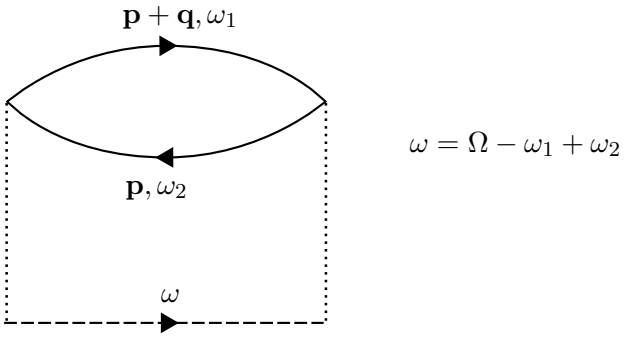

Figure 2.5.: Self-energy used for the hole propagator. Dashed lines represent VB holes, labeled with the frequency only since they are momentum-independent.

Let us evaluate this diagram. First, we recall the bare Green's functions, using (1.42):

$$G_c(\mathbf{k},\omega) = \frac{1}{\omega - \epsilon_\mathbf{k} + i0^+\mathrm{sign}(\epsilon_\mathbf{k} - \mu)} \tag{2.47}$$

$$D^{(0)}(\omega) = \frac{1}{\omega - E_G + i0^+} \ . \tag{2.48}$$

Using these, the diagram of Fig. 2.5 reads:

$$\Sigma(\Omega) = \frac{2V_0^2}{(2\pi)^6}\int d\mathbf{p}\ d\mathbf{q}\ d\omega_1\ d\omega_2\ \frac{1}{\Omega - E_G + i0^+}\cdot \frac{1}{\omega_1 - \epsilon_{\mathbf{p}+\mathbf{q}} + i0^+\mathrm{sign}(\epsilon_{\mathbf{p}+\mathbf{q}} - \mu)}\cdot \frac{1}{\omega_2 - \epsilon_\mathbf{p} + i0^+\mathrm{sign}(\epsilon_\mathbf{p} - \mu)} \ . \tag{2.49}$$

The frequency integrations are easy contour integrals. They yield, in terms of detuning:

$$\Sigma(\epsilon) = \frac{2V_0^2}{(2\pi)^4}\int d\mathbf{p}\ d\mathbf{q}\ \frac{n_F(\epsilon_\mathbf{p})(1 - n_F(\epsilon_{\mathbf{p}+\mathbf{q}}))}{\epsilon - \epsilon_{\mathbf{p}+\mathbf{q}} + \epsilon_\mathbf{p} + i0^+} \ . \tag{2.50}$$

To begin with, we evaluate $\Sigma(\epsilon)$ with logarithmic accuracy. This can be done, keeping the term $i0^+$ in the denominator of (2.50) finite during the integration. Then all appearing logarithms will be well defined. Of course, such an evaluation actually only gives $\Re[\Sigma](\epsilon)$ (compare (2.37)).

Following Ref. [7] (compare Eq. (25b) ff.), we assume $\Re[\Sigma](0)$ to be already absorbed in the definition of the renormalized gap E_G. Switching to energy integrations and cutting the $\mathbf{q}$-integration at the cutoff $\xi + \mu$, the leading logarithmic term of $\Re[\Sigma](\epsilon)$ then reads:

$$\Re[\Sigma](\epsilon) \simeq 2g^2\epsilon\log(|\epsilon|/\xi) \ . \tag{2.51}$$

Starting from (2.50), one can also explicitly calculate $\Im[\Sigma](\epsilon)$:

$$\Im[\Sigma](\epsilon) = -\frac{V_0^2}{(2\pi)^3}\int d\mathbf{p}\ d\mathbf{q}\ n_F(\epsilon_\mathbf{p})(1 - n_F(\epsilon_{\mathbf{p}+\mathbf{q}}))\delta(\epsilon - \epsilon_{\mathbf{p}+\mathbf{q}} + \epsilon_\mathbf{p}) \ . \tag{2.52}$$

Comparing with (2.30) ff., this is readily evaluated:

$$\Im[\Sigma](\epsilon) = -2g^2\pi\epsilon\cdot\theta(\epsilon) \ . \tag{2.53}$$

We can combine $\Im[\Sigma]$, $\Re[\Sigma]$ as

$$\Sigma(\epsilon) = 2g^2\epsilon \log\left(\frac{-\epsilon - i0^+}{\xi}\right) = 2g^2\epsilon\log(|\epsilon|/\xi) - i2g^2\pi\epsilon\cdot\theta(\epsilon)\ . \tag{2.54}$$

Beginning with $\Re[\Sigma](|\epsilon|)$ (notice the absolute value in (2.51)), there is another way to find $\Im[\Sigma](\epsilon)$ (compare [7], eq. (42) ff.):
We note that $\Sigma[\epsilon]$ is retarded. This is obvious from (2.50), and also holds for arbitrary hole self-energy diagrams: Since a hole necessarily propagates forward in time, one also has $\Sigma(t) \sim \theta(t)$. Therefore, having obtained $\Re[\Sigma](|\epsilon|)$, $\Im[\Sigma](|\epsilon|)$ is fixed by Kramers-Kronig relations.

We can then determine $\Im[\Sigma](\epsilon)$ from the fact that the spectral function $\mathcal{A}_h(\epsilon)$ fulfills:

$$\mathcal{A}_h(\epsilon)\begin{cases} > 0 & \epsilon > 0 \\ = 0 & \epsilon < 0 \end{cases}\ . \tag{2.55}$$

This fixes the signs for the imaginary part of the complex logarithm, yielding (2.54). This will be the way to go in most of our calculations: We will evaluate retarded quantities with logarithmic accuracy, with typical results like

$$\epsilon^\alpha = \exp\left[\alpha\log(\epsilon)\right]\ .$$

Then, using known properties like (2.55), we will add the imaginary part of the logarithm as in (2.54).

Using (2.54), one can then straightforwardly obtain the spectral function from the Green's function:

$$D(\epsilon) = \frac{1}{\epsilon - \Sigma(\epsilon)} \tag{2.56}$$

$$\mathcal{A}_h(\epsilon) \simeq 4\pi\frac{g^2}{\epsilon}\cdot\theta(\epsilon) + \mathcal{O}\left(\frac{g^4\log(\epsilon/\xi)}{\epsilon}\right)\ . \tag{2.57}$$

It should be noted that the result (2.57) is independent of $\Re[\Sigma](\epsilon)$.

Comparing (2.57) with the cluster result (2.43), we see that in leading order g^2 the two approaches coincide. If we only retain the self-energy diagram of Fig. 2.5, the two approaches will differ for higher orders in g. We should then prefer the cluster expression, since it coincides with the heuristic Anderson orthogonality result. Furthermore, the exponent of the cluster result is also obtained in the famous paper by Nozières and de Dominicis [9]. There, the calculation of the infinite mass hole propagator is reduced to a one-body problem, resulting in an integral equation. This equation can then be solved exactly in the limit $\epsilon \to 0$.

However, the Dyson Ansatz will prove useful in the evaluation of the finite mass hole spectral function, as discussed below.

2.2. The hole propagator: finite mass case

Let us advance to finite hole masses. Now the Hamiltonian H in the hole picture reads:

$$H = \sum_{\mathbf{k}} (E_G + E_{\mathbf{k}}) d^\dagger_{\mathbf{k}} d_{\mathbf{k}} + \sum_{\mathbf{k}} \epsilon_{\mathbf{k}} a^\dagger_{\mathbf{k}} a_{\mathbf{k}} - \underbrace{\frac{V_0}{\mathcal{S}} \sum_{\mathbf{p},\mathbf{k},\mathbf{q}} a^\dagger_{\mathbf{k}+\mathbf{q}} a_{\mathbf{k}} d^\dagger_{\mathbf{p}-\mathbf{q}} d_{\mathbf{p}}}_{=\hat{V}} \ . \tag{2.58}$$

We aim to calculate the spectral function of the VB hole propagator (2.3):

$$\mathcal{A}_h(\mathbf{Q}, \Omega) = -2\Im\left[D(\mathbf{Q}, \Omega)\right], \tag{2.59}$$

again using the fact that the VB hole is automatically retarded.

2.2.1. Linked-cluster approach

First, let us try to proceed in analogy to the infinite mass case. However, since $d_{\mathbf{Q}}$ does not have such simple projector properties, we cannot simply relate the Green's function to the S-matrix.

Following a suggestion by A. Rosch [34], the way around this problem is the cluster expansion for the Green's function (compare Ref. [21], section 3.6.2). As before, we will relate the standard perturbative expansion to the exponentiated version. First, one has

$$iD(\mathbf{Q}, t) = \sum_{n=0}^{\infty} \lambda^n W_n(\mathbf{Q}, t) \ , \tag{2.60}$$

where λ is a dimensionless coupling constant introduced to keep track of the powers of $\hat{V}$. Later we will set $\lambda = 1$. The factors $W_n(\mathbf{Q}, t)$ are defined as:

$$W_n(\mathbf{Q}, t) = \frac{(-i)^n}{n!} \int_{-\infty}^{\infty} dt_1 ... \int_{-\infty}^{\infty} dt_n \, \langle 0 | T\{\hat{V}(t_1) ... \hat{V}(t_n) d_{\mathbf{Q}}(t) d^\dagger_{\mathbf{Q}}(0)\} | 0 \rangle \ . \tag{2.61}$$

In order to resum this as:

$$D(\mathbf{Q}, t) = D^{(0)}(\mathbf{Q}, t) \exp\left[\sum_{n=1}^{\infty} \lambda^n F_n\right] \ , \tag{2.62}$$

upon comparing orders of λ we arrive at the following equations:

$$F_1 = \frac{-iW_1}{D^{(0)}} \tag{2.63}$$

$$F_2 = \frac{-iW_2}{D^{(0)}} - \frac{1}{2} F_1^2 \ . \tag{2.64}$$

Let us calculate $D(\mathbf{Q}, t)$ using these formulas. The zeroth order propagator reads:

$$D(\mathbf{Q}, t) = -i\theta(t) e^{-i(E_G + E_{\mathbf{Q}})t} \ . \tag{2.65}$$

For $W_1(\mathbf{Q}, t)$ we obtain:

$$W_1(\mathbf{Q}, t) = \frac{iV_0}{\mathcal{S}} \int_{-\infty}^{\infty} dt_1 \sum_{\mathbf{k}_1, \mathbf{p}_1, \mathbf{q}_1} \langle 0 | a^\dagger_{\mathbf{k}_1+\mathbf{q}_1}(t_1) a_{\mathbf{k}_1}(t_1) d^\dagger_{\mathbf{p}_1-\mathbf{q}_1}(t_1) d_{\mathbf{p}_1}(t_1) d_{\mathbf{Q}}(t) d^\dagger_{\mathbf{Q}}(0) | 0 \rangle = \tag{2.66}$$

$$= -i^4 \frac{V_0}{\mathcal{S}} \int_{-\infty}^{\infty} dt_1 \sum_{\mathbf{k}_1} G^{(0)}(\mathbf{k}_1, 0^-) D(\mathbf{Q}, t_1) D(\mathbf{Q}, t - t_1) \ .$$

The other disconnected contraction gives no contribution since it is proportional to $D(\mathbf{k}, 0^-) = 0$.

The diagram corresponding to $W_1(\mathbf{Q}, t)$ is shown in Fig. 2.6.

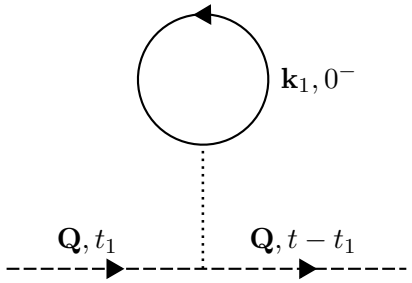

Figure 2.6.: $W_1(\mathbf{Q}, t)$, first order contribution to $D(\mathbf{Q}, t)$.

Comparing this diagram to the corresponding one in the infinite mass case, Fig. 2.1, we see that we obtain the diagrams in the finite mass case from the ones in the infinite mass case by drawing an incoming and outgoing VB hole line at each vertex.

Inserting the bare Green's functions (1.54) and (2.65), (2.66) is easily evaluated:

$$W_1(\mathbf{Q}, t) = 2iV_0 \int_{-\infty}^{\infty} dt_1 n \cdot \theta(t - t_1)\theta(t_1) e^{-i(E_G + E_{\mathbf{Q}})t} = 2inV_0 \theta(t) e^{-i(E_G + E_{\mathbf{Q}} t)} t \ . \tag{2.67}$$

Hence, using (2.63):

$$F_1(\mathbf{Q}, t) = 2itV_0 n \ , \tag{2.68}$$

which coincides with the infinite mass result (2.25).

As in the infinite mass case, we assume that this shift is contained in the definition of the renormalized gap.

Now let us calculate $W_2(\mathbf{Q}, t)$. First, there are two contributions (identical upon relabeling of variables) from contractions like this:

$$W_2^a(\mathbf{Q}, t) = -\frac{1}{2\mathcal{S}^2} V_0^2 \int_{-\infty}^{\infty} dt_1 \int_{-\infty}^{\infty} dt_2 \sum_{\mathbf{k}_1, \mathbf{p}_1, \mathbf{q}_1} \sum_{\mathbf{k}_2, \mathbf{p}_2, \mathbf{q}_2} \tag{2.69}$$

$$\langle 0 | c^\dagger_{\mathbf{k}_1 + \mathbf{q}_1}(t_1) c_{\mathbf{k}_1}(t_1) d^\dagger_{\mathbf{p}_1 - \mathbf{q}_1}(t_1) d_{\mathbf{p}_1}(t_1) c^\dagger_{\mathbf{k}_2 + \mathbf{q}_2}(t_2) c_{\mathbf{k}_2}(t_2) d^\dagger_{\mathbf{p}_2 - \mathbf{q}_2}(t_2) d_{\mathbf{p}_2}(t_2) d_{\mathbf{Q}}(t) d^\dagger_{\mathbf{Q}}(0) | 0 \rangle =$$

$$\frac{i^5}{2} \int_{-\infty}^{\infty} dt_1 \int_{-\infty}^{\infty} dt_2 \sum_{\mathbf{p}, \mathbf{q}} G_c(\mathbf{p}, t_1 - t_2) G(\mathbf{p} + \mathbf{q}, t_2 - t_1) D^{(0)}(\mathbf{Q}, t_1) D^{(0)}(\mathbf{Q} - \mathbf{q}, t_2 - t_1) D^{(0)}(\mathbf{Q}, t - t_2) \ .$$

Diagrammatically, this is depicted in Fig. 2.7.

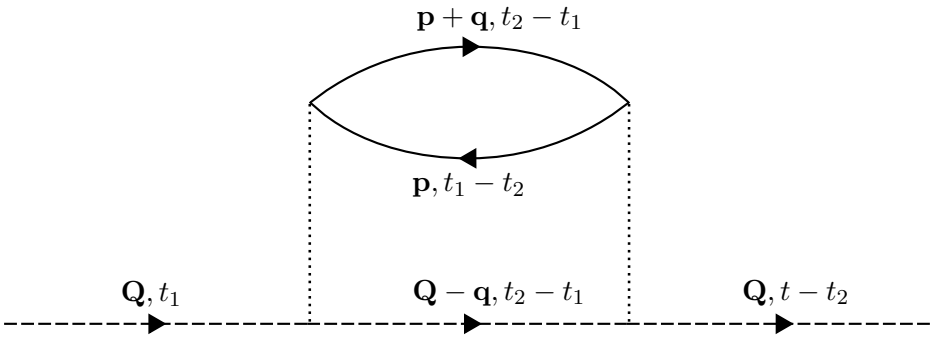

Figure 2.7.: $W_2^a(\mathbf{Q}, t)$, second order contribution to $D(\mathbf{Q}, t)$.

We note that this diagram exactly corresponds to the one we used for the hole self-energy in the infinite mass case, c.f. Fig. 2.5.

The second contribution to $W_2(\mathbf{Q}, t)$ comes from contractions like this (there are again two identical combinations):

$$W_2^b(\mathbf{Q}, t) = -\frac{1}{2} V_0^2 \int_{-\infty}^{\infty} dt_1 \int_{-\infty}^{\infty} dt_2 \sum_{\mathbf{k}_1, \mathbf{p}_1, \mathbf{q}_1} \sum_{\mathbf{k}_2, \mathbf{p}_2, \mathbf{q}_2} \tag{2.70}$$

$$\langle 0 | c^\dagger_{\mathbf{k}_1+\mathbf{q}_1}(t_1) c_{\mathbf{k}_1}(t_1) d^\dagger_{\mathbf{p}_1-\mathbf{q}_1}(t_1) d_{\mathbf{p}_1}(t_1) c^\dagger_{\mathbf{k}_2+\mathbf{q}_2}(t_2) c_{\mathbf{k}_2}(t_2) d^\dagger_{\mathbf{p}_2-\mathbf{q}_2}(t_2) d_{\mathbf{p}_2}(t_2) d_{\mathbf{Q}}(t) d^\dagger_{\mathbf{Q}}(0) | 0 \rangle$$

$$= -\frac{i^5}{2} \int_{-\infty}^{\infty} dt_1 \int_{-\infty}^{\infty} dt_2 \sum_{\mathbf{k}_1, \mathbf{k}_2} G_c(\mathbf{k}_1, 0^-) G_c(\mathbf{k}_2, 0^-) D^{(0)}(\mathbf{Q}, t_1) D^{(0)}(\mathbf{Q}, t_2 - t_1) D^{(0)}(\mathbf{Q}, t - t_2)$$

The corresponding diagram is shown in Fig. 2.8.

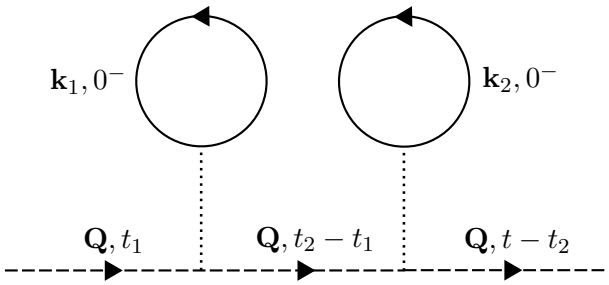

Figure 2.8.: $W_2^b(\mathbf{Q}, t)$, second order contribution to $D(\mathbf{Q}, t)$.

All other contractions vanish since they contain VB holes propagating backwards in time.

Now let us evaluate $F_2(\mathbf{Q}, t)$, using formula (2.64). Inserting the bare Green's functions, it is seen that:

$$\frac{-i2W_2^b(\mathbf{Q}, t)}{D^{(0)}} - \frac{1}{2} F_1^2(\mathbf{Q}, t) = 0 \ , \tag{2.71}$$

as expected, since Fig. 2.8 is essentially just the square of Fig. 2.6, and the cluster expansion is designed to count every disjunkt diagram only once.

Inserting the bare Green's function into (2.69) and after straightforward integration, we thus obtain:

$$F_2(\mathbf{Q},t) = \frac{-i2W_2^a(\mathbf{Q},t)}{D^{(0)}} = \tag{2.72}$$
$$V_0^2 \sum_{\mathbf{p},\mathbf{q}} \left[\frac{itn_F(\epsilon_\mathbf{p})(1-n_F(\epsilon_{\mathbf{p}+\mathbf{q}}))}{\epsilon_{\mathbf{p}+\mathbf{q}}+\Delta_\mathbf{q}-\epsilon_\mathbf{p}} - \frac{n_F(\epsilon_\mathbf{p})(1-n_F(\epsilon_{\mathbf{p}+\mathbf{q}}))}{(\epsilon_{\mathbf{p}+\mathbf{q}}+\Delta_\mathbf{q}-\epsilon_\mathbf{p})^2}(1-e^{-it(\epsilon_{\mathbf{p}+\mathbf{q}}+\Delta_\mathbf{q}-\epsilon_\mathbf{p})}) \right] ,$$

where

$$\Delta_\mathbf{q} = E_{\mathbf{Q}-\mathbf{q}} - E_\mathbf{Q} \ . \tag{2.73}$$

It should be noted that (2.72) coincides with the infinite mass expression (2.27) for $\Delta_\mathbf{q} = 0$ (the first term looks different, but the expressions coincide by antisymmetry). The factor $(\epsilon_{\mathbf{p}+\mathbf{q}} - \epsilon_\mathbf{p} + \Delta_\mathbf{q})$ appearing in (2.72) is precisely the energy cost for creating one bubble as shown in Fig. (2.7).

2.2.2. Hole spectral function for $Q = 0$

Let us now specialize on an external hole momentum of $Q = 0$. We choose this value as the simplest case of study; furthermore, one can expect to gain insights on zero-momentum excitons, for which the calculation is in principle similar (c.f. supplement, chapter 7).

The calculation of the $(Q = 0)$ hole spectral function was already accomplished in Ref. [35], where a saddle-point evaluation of a functional integral was used. We will, however, stick to the cluster approach introduced in the last section. We believe that this allows for a simpler understanding of the underlying physics, especially in view of the calculation of the absorption we will do later on. We will recover all findings of Ref. [35] relevant for our problem, and furthermore be able to verify some important analytical properties of the hole spectral function. In addition, we will clarify the connection with the $Q > 0$ case, which was not considered in Ref. [35].

A short linked-cluster calculation of a similar (spin-dependent) problem can be found in Ref. [36].

Let us start the evaluation. Beginning with (2.73), for $Q = 0$ we have:

$$\Delta_\mathbf{q} = E_\mathbf{q} \ . \tag{2.74}$$

As in the infinite mass case we concentrate on the second term of $F_2(\mathbf{Q},t)$. In the same fashion, we obtain:

$$F_2(t) = -\int_\infty^\infty \frac{1}{\nu^2} N(\nu)(1-e^{-i\nu t})d\nu \tag{2.75}$$
$$N(\nu) = V_0^2 \sum_{\mathbf{p},\mathbf{q}} n_F(\epsilon_\mathbf{p})(1-n_F(\epsilon_{\mathbf{p}+\mathbf{q}}))\delta(\nu - E_\mathbf{q} + \epsilon_\mathbf{p} - \epsilon_{\mathbf{p}+\mathbf{q}}) \ . \tag{2.76}$$

In the evaluation of $N(\nu)$, now we have to distinguish two cases. First, we consider the high-frequency case $\nu \lesssim \xi$, i.e. ν not much smaller than the UV cut-off. Then clearly for all relevant momenta $\mathbf{q}$ we have:

$$\nu \gg E_\mathbf{q} \ . \tag{2.77}$$

Therefore we can just set $\nu - E_{\mathbf{q}} \simeq \nu$ in the delta-function (2.76), and reuse the infinite mass result (2.31):

$$N(\nu) \simeq 2g^2\nu\theta(\xi - \nu) \ , \qquad \nu \lesssim \xi \ . \tag{2.78}$$

The reason for this is transparent: For frequencies much higher than characteristic VB hole kinetic energies, the VB hole behaves as if it were immobile.

Now let us consider the low-frequency case, i.e. $\nu \ll \xi$. First, we notice that in the delta-function of (2.76), we necessarily have $\nu - E_{\mathbf{q}} > 0$ due to the structure of the Fermi-functions. This also means that $N(\nu)$ will vanish at $\nu = 0$: every scattering will increase the energy of the $(Q = 0)$ - hole from E_G to $E_G + q^2/2M$ and result in a particle hole excitation of the CB Fermi sea, which also costs energy. Thus, only scatterings for $\nu > 0$ are possible.

Second, we observe that in the limit $\nu \to 0$ in the $\mathbf{q}$-sum in (2.76) only the momenta $q < 2k_F$ contribute, since for higher values of q necessarily $\epsilon_{\mathbf{p}+\mathbf{q}} - \epsilon_{\mathbf{p}} > 0$. Thus, there are two cutoffs on the $\mathbf{q}$-sum:

- $q^2/2M < \nu \Rightarrow q < \sqrt{2M\nu}$ and
- $q < 2k_F$.

Following Ref. [35], we will call the energy, at which the two cutoffs conincide, the *recoil energy* E_R:

$$E_R = \frac{(2k_F)^2}{2M} = 4\beta\mu \ . \tag{2.79}$$

E_R corresponds to the maximal energy transferred to a hole in a scattering process where the resulting CB-electron hole pair has an infinitesimal energy. A sketch of such a process is shown in Fig. (2.9). Since we are working in the hole picture, the VB energy band is shown inverted.

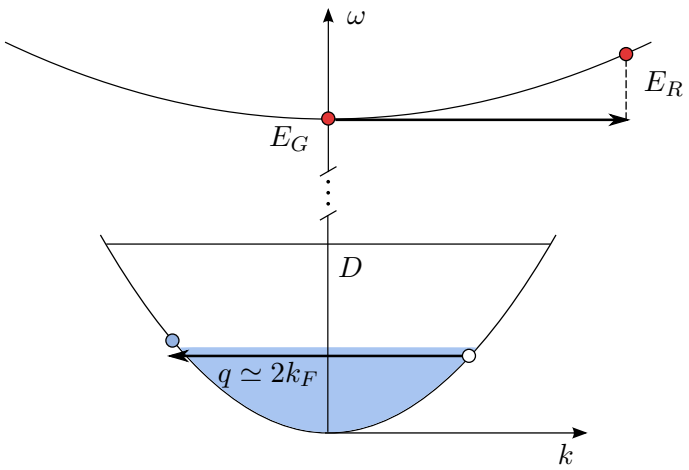

Figure 2.9.: Low-energy scattering process where E_R is transfered to the VB hole. VB holes are drawn as red dots.

We will now restrict ourselves to the ultra-low frequency regime, meaning that we will calculate the leading behaviour in ν of $N(\nu)$ for $\nu \ll E_R$. Since E_R can be seen as

the characteristic kinetic energy of a VB hole, this means that we are interested in the high-mobility limit. E_R will serve as the crossover scale between the high mobility and the immobility limit.

Starting from (2.76), switching to momentum integrations and carrying out the implicit spin sum, we thus have to calculate:

$$N(\nu) = 2V_0^2 \int_{q<\sqrt{2M\nu}} \frac{d\mathbf{q}}{(2\pi)^2} L(\mathbf{q}, \nu - E_\mathbf{q}) \tag{2.80}$$
$$L(\mathbf{q}, \nu - E_\mathbf{q}) = \int \frac{d\mathbf{p}}{(2\pi)^2} n_F(\epsilon_\mathbf{p})(1 - n_F(\epsilon_{\mathbf{p}+\mathbf{q}}))\delta(\nu - E_\mathbf{q} + \epsilon_\mathbf{p} - \epsilon_{\mathbf{p}+\mathbf{q}})\theta(\nu - E_\mathbf{q}) \ .$$

Due to the $\mathbf{q}$-dependence of the term $E_\mathbf{q}$, the evaluation of this integral is more difficult than in the infinite mass case. We can proceed observing that the term $L(\mathbf{q}, \nu - E_\mathbf{q})$ is proportional to the imaginary part of the 2D Lindhard-function χ_2. The calculation of the latter is a text-book problem; in two dimensions it is found in Ref. [37]. Comparing with formula (5.5) of Ref. [37], we find:

$$L(q, \nu - E_\mathbf{q}) = -\frac{1}{2\pi}\theta(\nu - E_\mathbf{q})\chi_2(q, \nu - E_\mathbf{q}) \ . \tag{2.81}$$

To match the notations in Ref. [37], we now introduce rescaled variables:

$$x = \frac{q}{k_F} \ , \qquad \omega_x = \alpha - \frac{E_\mathbf{q}}{\mu} \ , \qquad \alpha = \frac{\nu}{\mu} \ . \tag{2.82}$$

In terms of these rescaled variables, we will be looking for the leading behaviour of $N(\alpha)$ in α. For fixed α, $\chi_2(x, \omega_x)$ then reads:

$$\chi_2(x, \omega_x) = \begin{cases} \chi_2^b(x, \omega_x) & -1 + \sqrt{1 + \omega_x} < x < 1 - \sqrt{1 - \omega_x} \\ \chi_2^a(x, \omega_x) & 1 - \sqrt{1 - \omega_x} < x < 1 + \sqrt{1 - \omega_x} \\ \chi_2^b(x, \omega_x) & 1 + \sqrt{1 - \omega_x} < x < 1 + \sqrt{1 + \omega_x} \\ 0 & \text{else} \end{cases} \ , \tag{2.83}$$

where

$$\chi_2^a(x, \omega_x) = -\frac{k_F^2}{2\pi} \cdot \frac{1}{\mu} \cdot \frac{1}{x} \left[\sqrt{1 - \frac{1}{4}\left(\frac{\omega_x}{x} - x\right)^2} - \sqrt{(1 - \frac{x^2}{4}) - \frac{\omega_x}{2} - \frac{\omega_x^2}{4x^2}} \right] \ . \tag{2.84}$$

and

$$\chi_2^b(x, \omega_x) = -\frac{k_F^2}{2\pi} \frac{1}{\mu} \frac{1}{x} \sqrt{1 - \frac{1}{4}\left(\frac{\omega_x}{x} - x\right)^2} \ . \tag{2.85}$$

In our energy regime of interest the momentum cut-off is given by

$$x < \sqrt{\alpha/\beta} \ll 1 \ , \tag{2.86}$$

s.t. we only have to consider the first two cases of (2.83). We now notice that:

$$\omega_x = \mathcal{O}(\alpha) \ . \tag{2.87}$$

Simply by considering the boundaries in (2.83) one can then show that the contribution to $N(\alpha)$ coming from χ_2^b will scale as $\mathcal{O}(\alpha^2)$, which will be shown to be subleading. Thus, we concentrate on the contribution from χ_2^a.

Expanding it in ω_x leads to:

$$\chi_2^a(x,\omega_x) = -\frac{k_F^2}{2\pi}\cdot\frac{1}{\mu}\cdot\frac{1}{x}\frac{\omega_x}{\sqrt{4-x^2}} + \mathcal{O}(\omega_x^3)\ . \tag{2.88}$$

In leading order of accuracy, we can then rewrite the relevant integral (2.80) as:

$$N(\alpha) = \frac{2V_0^2}{(2\pi)^3}\frac{(k_F)^4}{\mu}\int_0^{\sqrt{\alpha/\beta}} dx\ \frac{\alpha-\beta x^2}{\sqrt{4-x^2}}\ . \tag{2.89}$$

In extending the lower boundary of (2.89) down to zero we made an error of order

$$\int_0^{\alpha} dx\ \chi_2^a(x,\omega_x) = \mathcal{O}(\alpha^2)\ , \tag{2.90}$$

which can be shown considering higher derivatives of $\chi_2^a(x,\omega_x)$ in ω_x. The remaining integral (2.89) is carried out easily noticing that since $\sqrt{\alpha/\beta} \ll 1$, we can approximate the squareroot by $1/2$. As a result we obtain:

$$N(\nu) = \frac{4g^2}{3\pi}\cdot\frac{1}{\sqrt{E_R}}\cdot\nu^{3/2}\ , \qquad \nu \ll E_R\ . \tag{2.91}$$

In terms of α thus $N(\alpha)\sim\alpha^{3/2}$.

To make progress in the calculation of $\mathcal{A}_h(0,\Omega)$, we now combine the two limits of $N(\nu)$, (2.78) and (2.91), in the following rough approximation:

$$N(\nu) = \begin{cases} C_1 g^2\cdot\nu^{3/2} & 0<\nu<E_R\ , \qquad C_1 = 4/(3\pi\sqrt{E_R}) \\ 2g^2\cdot\nu + C_2 & E_R<\nu<\xi \\ 0 & \nu>\xi \end{cases}\ . \tag{2.92}$$

We have introduced the constant $C_2 = \mathcal{O}(E_R)$ (the concrete value is irrelevant) to ensure continuity of $N(\nu)$. A schematic plot of $N(\nu)$ is shown in Fig. 2.10.

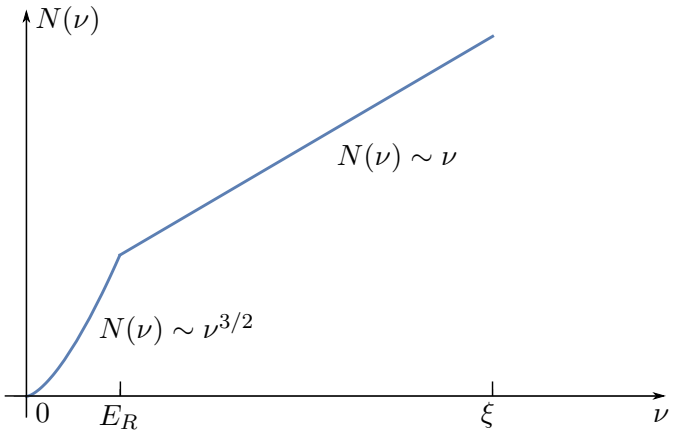

Figure 2.10.: Schematic plot of the scattering phase space function $N(\nu)$.

As discussed in the infinite mass case, $N(\nu)$ measures the phase space for the scattering of CB electrons and VB holes with energy cost ν. We have found that this phase space is reduced in the region $\nu < E_R$. This can be understood as follows: For ν very small, there are two extremal scattering processes in terms of the transferred momentum q:

- Scatterings with $q \simeq 0^+$. A sketch of these is shown in Fig. (2.11).

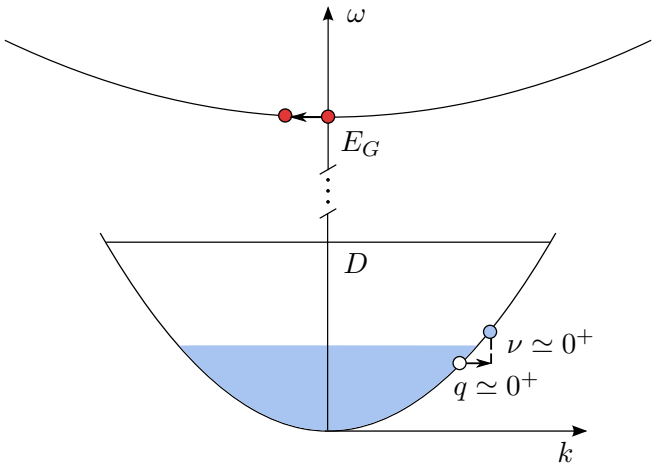

Figure 2.11.: Scattering with low momentum transfer and low energy cost.

  Since for these processes the final kinetic energy of the VB hole is negligible, they will still contribute to the low-frequency phase space.

- Scatterings with $q \simeq 2k_F$. The corresponding picture was shown in Fig. 2.9. In the infinite mass case, since the hole band was flat, such scatterings could happen at infinitesimal energy cost. Now, however, the energy cost is at least E_R. Therefore, these scatterings will not contribute to the low-frequency phase space, which is thus reduced compared to the infinite mass case.

Let us now continue with the evaluation of $\mathcal{A}_h(0,\Omega)$. In terms of ϵ, the detuning from E_G, and analogously to formula (2.41), we have to calculate:

$$\mathcal{A}_h(0,\epsilon) = \int_{-\infty}^{\infty} dt \;\; \exp\left(i\epsilon t\right) \exp\left(F_2(t)\right) \tag{2.93}$$

$$F_2(t) = -\int_0^{\xi} d\nu \;\; \frac{1}{\nu^2} N(\nu)(1 - e^{-i\nu t}) \; . \tag{2.94}$$

First, we consider the behaviour of $F_2(t)$ as $t \to \pm\infty$. In the infinite mass limit $F_2(t)$ was logarithmically divergent, c.f. (2.35). Now, however, since the factor $N(\nu)/\nu^2$ is integrable at $\nu = 0$, inserting (2.92) into (2.94) yields:

$$\lim_{t\to\pm\infty} F_2(t) = \text{const} \simeq 2g^2 \log(E_R/\xi) \qquad \text{for } E_R \ll \xi \; , \tag{2.95}$$

which holds with logarithmic accuracy. Inserting this limit into (2.93), we obtain the quasi-particle (coherent) part of the spectral function:

$$\mathcal{A}_h^c(0,\epsilon) = 2\pi (E_R/\xi)^{2g^2} \cdot \delta(\epsilon) \; . \tag{2.96}$$

The appearance of this peak can again be understood in terms of scattering phase space: Since scatterings with $q \simeq 2k_F$ cost a finite amount of energy E_R, there is not enough phase space available to completely convert the noninteracting spectral function, which is a delta peak, into a power law as in the infinite mass case. A delta peak with a finite weight always remains, as also found in Ref. [35].

It should be noted, that for $M \to \infty$, i.e. $E_R \to 0$, the weight vanishes, while in the absence of interactions, $g = 0$, the delta peak aquires the full weight 2π.

Let us now consider the incoherent part of the spectral function. It can be found simply subtracting the coherent part. Splitting $\exp(F_2(t))$ in the coherent and incoherent part, one obtains:

$$\mathcal{A}_h^i(0,\epsilon) = (E_R/\xi)^{2g^2} \int_{-\infty}^{\infty} dt\ e^{i\epsilon t} \left[\exp\left(\int_0^{\xi} d\nu \frac{1}{\nu^2} N(\nu) e^{-i\nu t} \right) - 1 \right] \tag{2.97}$$

$$= (E_R/\xi)^{2g^2} \int_{-\infty}^{\infty} dt\ e^{i\epsilon t} \sum_{n=1}^{\infty} \frac{1}{n!} \left[\int_{-\infty}^{\infty} \frac{d\nu}{2\pi}\ e^{-i\nu t} \cdot 2\pi \frac{1}{\nu^2} N(\nu)\theta(\nu)\theta(\xi-\nu) \right]^n . \tag{2.98}$$

To begin with, we specialize on a qualitative evaluation of the limit $\epsilon \to 0$. The largest contribution to the integral comes from typical times:

$$t_{\text{typ}} \sim 1/\epsilon\ . \tag{2.99}$$

Thus, $e^{-i\nu t}$ will oscillate quickly, hence the term in square brackets will have a small value. Also $N(\nu)$ itself contains the small parameter g^2. Therefore, as leading approximation one can just keep the first order term of the exponential. With the notation:

$$B(\nu) = 2\pi \frac{N(\nu)}{\nu^2} \theta(\nu)\theta(\xi-\nu)\ , \tag{2.100}$$

we see that in this approximation

$$\mathcal{A}_h^i(0,\epsilon) \simeq (E_R/\xi)^{2g^2} \left[FT \circ FT^{-1}(B) \right](\epsilon)\ , \tag{2.101}$$

where FT denotes the Fourier-transform. Therefore, we just obtain:

$$\mathcal{A}_h^i(0,\epsilon) \simeq (E_R/\xi)^{2g^2} B(\epsilon)\ . \tag{2.102}$$

Inserting the low frequency behaviour of N, we see that

$$\mathcal{A}_h^i(0,\epsilon) \sim \frac{1}{\sqrt{\epsilon}} \qquad \epsilon \ll E_R\ , \tag{2.103}$$

which again coincides with the results in Ref. [35]. As in the discussion of the incoherent part, we observe that in comparison to the infinite mass limit (2.44), the spectral function is narrower for $\epsilon > 0$.

Let us continue with the evaluation of some important analytic properties of the spectral function. Starting from (2.98), and interchanging the sum and the time integral, one observes that the time integral of the n-th summand yields a delta-function of the form:

$$\delta(\epsilon - \nu_1 - \nu_2\ ...\ - \nu_n) \qquad \text{with } \nu_1,\ ...\ \nu_n \in [0,\xi]\ . \tag{2.104}$$

Therefore, we conclude that $\mathcal{A}_h^i(0,\epsilon) \sim \theta(\epsilon)$, as expected.

For the further evaluation it is worth noticing that $\mathcal{A}_h^i$ is just a sum of multiple convolutions of $B(\nu)$:

$$\mathcal{A}_h^i(0,\epsilon) = (E_R/\xi)^{2g^2} \sum_{n=1}^{\infty} \frac{1}{n! \cdot (2\pi)^{n-1}} \underbrace{[B * ... * B]}_{n \text{ times}}(\epsilon) \ . \tag{2.105}$$

Since $B(\nu) > 0$, one immediately obtains $A_h^i(0,\epsilon) > 0$. In addition, the positivity of the convolutions shows that the expansion of the exponential was meaningful in the first place by monotone convergence. Using

$$\int_{-\infty}^{\infty} \frac{d\epsilon}{2\pi} B(\epsilon) \simeq 2g^2 \log(\xi/E_R) \ , \tag{2.106}$$

and the identity

$$\int_{-\infty}^{\infty} dx \, (f * f)(x) = \left(\int_{-\infty}^{\infty} dx f(x) \right)^2 \ , \tag{2.107}$$

one can further check that the sum rule for $\mathcal{A}_h(0,\epsilon)$ is fulfilled:

$$\begin{aligned} &\int_{-\infty}^{\infty} \frac{d\epsilon}{2\pi} \mathcal{A}_h(0,\epsilon) = \int_{-\infty}^{\infty} \frac{d\epsilon}{2\pi} \left(\mathcal{A}_h^c(0,\epsilon) + \mathcal{A}_h^i(0,\epsilon) \right) = \\ &\left(\frac{E_R}{\xi} \right)^{2g^2} \left\{ 1 + \int_{-\infty}^{\infty} \frac{d\epsilon}{2\pi} \left(B(\epsilon) + \frac{1}{2!2\pi} (B * B)(\epsilon) + \frac{1}{3!(2\pi)^2} (B * B * B)(\epsilon) ... \right) \right\} \\ &\simeq \left(\frac{E_R}{\xi} \right)^{2g^2} \exp\left(2g^2 \log\left(\frac{\xi}{E_R} \right) \right) = 1 \ . \end{aligned} \tag{2.108}$$

Studying the convolutions, one can also extract the leading behaviour of $\mathcal{A}_h(0,\epsilon)$ for $\epsilon \lesssim \xi$ (of course for $\epsilon > 0$, $\mathcal{A}_h(0,\epsilon) = \mathcal{A}_h^i(0,\epsilon)$). We study $\epsilon < \xi$, since $\mathcal{A}_h(\epsilon)$ will have a discontinuity at $\epsilon = \xi$ due to the term $\theta(\xi - \epsilon)$ in $B(\epsilon)$.
The first order contribution from (2.105) reads:

$$\mathcal{A}_h(0,\epsilon)^{(1)} = (E_R/\xi)^{2g^2} B(\epsilon) = 2\pi (E_R/\xi)^{2g^2} \cdot \frac{2g^2}{\epsilon} \ . \tag{2.109}$$

Using $\xi \gg E_R$, the second order contribution reads:

$$\mathcal{A}_h(0,\epsilon)^{(2)} = (E_R/\xi)^{2g^2} \frac{1}{4\pi} (B * B)(\epsilon) \simeq (E_R/\xi)^{2g^2} \pi (2g^2)^2 \int_{E_R}^{\epsilon - E_R} d\omega \frac{1}{\omega} \frac{1}{\epsilon - \omega} \ , \tag{2.110}$$

where we only used the high-frequency form of $B(\epsilon)$, which will dominate the convolution integral. A partial fraction expansion then shows that:

$$\mathcal{A}_h(0,\epsilon)^{(2)} \simeq 2\pi (E_R/\xi)^{2g^2} \cdot \frac{(2g^2)^2}{\epsilon} \log(\epsilon/E_R) \ . \tag{2.111}$$

The third order contribution reads:

$$\mathcal{A}_h(0,\epsilon)^{(3)} = (E_R/\xi)^{2g^2} \cdot \frac{1}{24\pi^2}(B * B * B)(\epsilon) \tag{2.112}$$

$$\simeq (E_R/\xi)^{2g^2} \frac{1}{3}\pi(2g^2)^3 \int_{E_R}^{\epsilon-2E_R} d\omega_1 \int_{E_R}^{\epsilon-\omega_1-E_R} d\omega_2 \frac{1}{\omega_1}\frac{1}{\omega_2}\frac{1}{\epsilon-\omega_1-\omega_2} \tag{2.113}$$

$$\simeq 2\pi(E_R/\xi)^{2g^2} \cdot \frac{(2g^2)^3}{2\epsilon}\log^2(\epsilon/E_R)$$

In the last step we again used a partial fraction expansion and took the most divergent parts of the ω_1-integral.

One can extrapolate this series, which yields:

$$\mathcal{A}_h(\epsilon) = 2\pi(E_R/\xi)^{2g^2} \cdot \frac{1}{\epsilon}(\epsilon/E_R)^{2g^2} \sim \frac{1}{\xi} \cdot \left(\frac{\epsilon}{\xi}\right)^{2g^2-1} . \tag{2.114}$$

compare (2.44). This means that for energy scales much larger than E_R we recover the $(M = \infty)$-behaviour, as expected.

Due to the discontinuity at $\epsilon = \xi$ mentioned above, the detailed form of the UV cutoff of the spectral function is different than in the infinite mass case, but this is of no physical relevance.

A summary of our results for the $(Q = 0)$ hole spectral function is sketched in Fig. 7.6.

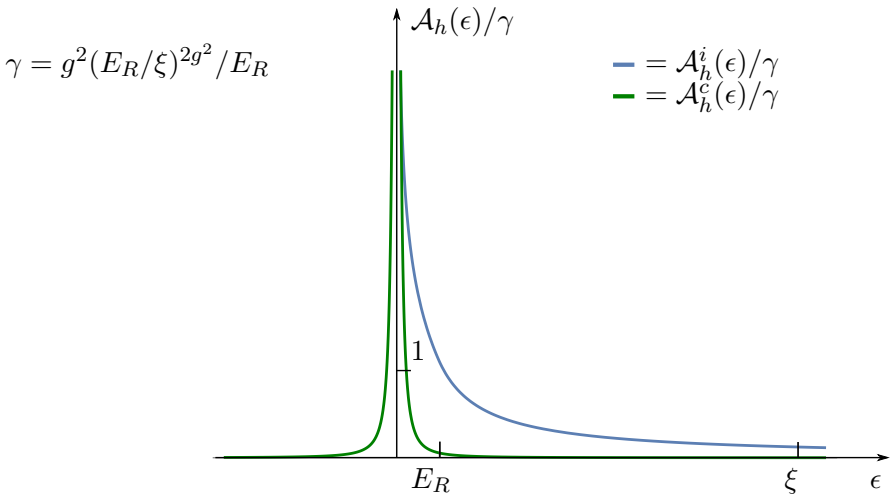

Figure 2.12.: Sketched plot of the $Q = 0$ hole spectral function. Coherent part is shown with a finite width. Scale on the vertical axis reflects the correct order of magnitude for $\mathcal{A}_h(E_R)$.

For better comparison of the different power laws, Fig. (2.13) shows a sketched double logarithmic plot of the spectrum.

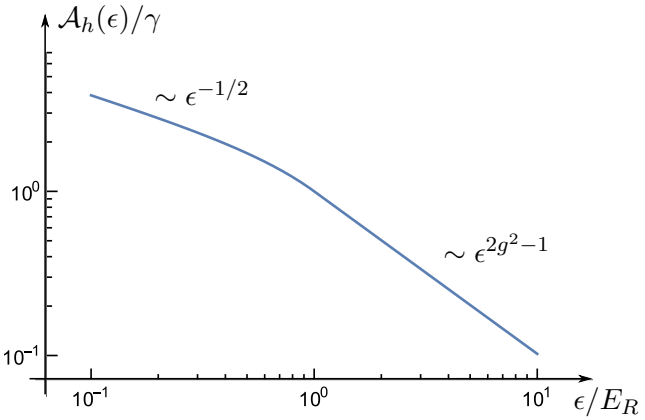

Figure 2.13.: Sketched double logarithmic plot of the $Q = 0$ hole spectral function. Used parameter: $g = 0.1$.

To summarize, we have found that in the low-frequency regime the hole spectral function $\mathcal{A}_h(0, \epsilon)$ is more particle-like due to the reduced scattering phase space.

2.2.3. Hole spectral function for $Q = k_F$

Let us now discuss the hole spectral function for $Q = k_F$. We choose this special value, since the momenta close to k_F will dominate the physics of the cavity absorption in the Fermi-edge regime, as discussed in the next chapter.

Starting from the linked cluster approach, now the factor $\Delta_{\mathbf{q}}$ in (2.73) reads:

$$\Delta_{\mathbf{q}} = E_{\mathbf{Q}-\mathbf{q}} - E_{k_F} \ , \qquad Q = |\mathbf{Q}| = k_F \ . \tag{2.115}$$

The corresponding scattering phase space factor then reads, in analogy to (2.76):

$$N(\nu) = V_0^2 \sum_{\mathbf{p},\mathbf{q}} n_F(\epsilon_{\mathbf{p}})(1 - n_F(\epsilon_{\mathbf{p}+\mathbf{q}}))\delta(\nu - \Delta_{\mathbf{q}} + \epsilon_{\mathbf{p}} - \epsilon_{\mathbf{p}+\mathbf{q}}) \ . \tag{2.116}$$

The behaviour of $N(\nu)$ now has a major difference to the cases discussed before: $N(\nu)$ vanishes at $\nu = -E_{k_F}$, not at $\nu = 0$ as before. This is easily seen: In (2.116) we have $\nu - \Delta_{\mathbf{q}} > 0$, but as seen from (2.115), $\min(\Delta_{\mathbf{q}}) = -E_{k_F}$. This can be understood in terms of scatterings (compare also Ref. [38]): For $Q = k_F$, there can be scatterings which lower the energy. The extremal case of such a scattering is shown in Fig. 2.14.

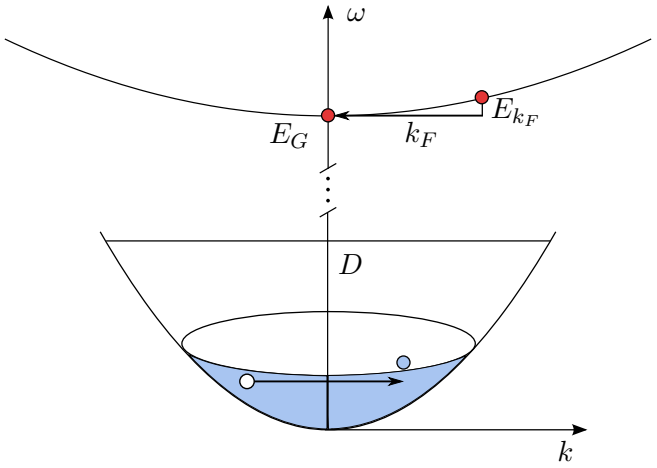

Figure 2.14.: Scattering of a VB hole with $Q = k_F$ which lowers the energy. In the CB, the 2D dispersion paraboloid is indicated.

Thus, the minimal energy for the creation of a hole with momentum k_F is actually E_G instead of $E_G + E_{k_F}$. We can therefore assume that the onset of the hole spectral function is at E_G. Such a threshold mediated by scatterings is called *indirect*.

Is is clear that the appearance of this threshold also leads to a nonsingular spectral function: The spectral weight of the particle delta-peak at $E_G + E_{k_F}$ is now distributed over the interval $[E_G, E_G + E_{k_F}]$, s.t. no singularity remains.

In principle we could now proceed with the linked cluster evaluation. For the high-frequency behaviour we do not expect any changes, in complete analogy to the $(Q = 0)$-case:

$$\mathcal{A}_h(k_F, \epsilon) \sim \frac{1}{\xi}(\epsilon/\xi)^{2g^2-1} , \qquad \epsilon \lesssim \xi . \tag{2.117}$$

In the low-frequency regime, however, the evaluation is difficult, since the resulting function $F_2(t)$ is complicated. The Fourier-transform needed for the spectral function is then hard to do analytically.

Let us therefore make use of the Dyson equation approach discussed in section 2.1.4 for the infinite mass case. In doing so, we restrict ourselves to the evaluation of all quantities to order $\mathcal{O}(g^2)$.

The generalization of the Dyson approach to finite masses is straightforward. A similar calculation (or rather the result) can be found in Ref. [27], but in 3D instead of 2D.

Let us redraw the important self-energy diagram corresponding to Fig. 2.5 for finite hole mass:

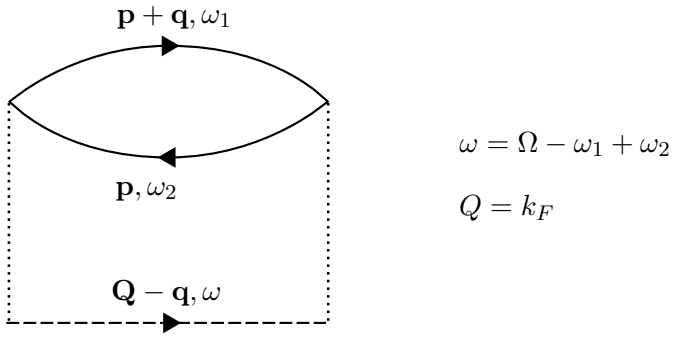

Figure 2.15.: Self-energy used for the hole propagator for finite mass and $Q = k_F$.

For finite hole mass, the bare propagator now reads:

$$D^{(0)}(\mathbf{k},\Omega) = \frac{1}{\Omega - E_G - E_{\mathbf{k}} + i0^+} \ . \tag{2.118}$$

The self-energy diagram gives:

$$\Sigma(k_F,\Omega) = \frac{2V_0^2}{(2\pi)^6}\int\int d\mathbf{p}\ d\mathbf{q}\ d\omega_1\ d\omega_2 \frac{1}{\omega - E_G - E_{\mathbf{Q}-\mathbf{q}} + i0^+}\cdot \\ \frac{1}{\omega_1 - \epsilon_{\mathbf{p}+\mathbf{q}} + i0^+\mathrm{sign}(\epsilon_{\mathbf{p}+\mathbf{q}} - \mu)} \cdot \frac{1}{\omega_2 - \epsilon_{\mathbf{p}} + i0^+\mathrm{sign}(\epsilon_{\mathbf{p}} - \mu)} \ . \tag{2.119}$$

The frequency integrals are easily performed with contour integration. This also fixes the determination of the signum-functions: for a wrong sign, both poles lie in the same half plane and closing the contour gives zero. This type of frequency integration will always occur in the FER.

The result reads, in terms of detuning from the gap ϵ:

$$\Sigma(k_F,\epsilon) = \frac{2V_0^2}{(2\pi)^4}\int d\mathbf{p}\ d\mathbf{q}\ \frac{n_F(\epsilon_{\mathbf{p}})(1-n_F(\epsilon_{\mathbf{p}+\mathbf{q}}))}{\epsilon - E_{\mathbf{Q}-\mathbf{q}} - \epsilon_{\mathbf{p}+\mathbf{q}} + \epsilon_{\mathbf{p}} + i0^+} \ . \tag{2.120}$$

Let us first compute $\Im[\Sigma](k_F,\epsilon)$. It reads:

$$\Im[\Sigma](k_F,\epsilon) = -\frac{V_0^2}{(2\pi)^3}\int d\mathbf{p}\ d\mathbf{q}\ n_F(\epsilon_{\mathbf{p}})(1-n_F(\epsilon_{\mathbf{p}+\mathbf{q}}))\delta(\epsilon - E_{\mathbf{Q}-\mathbf{q}} - \epsilon_{\mathbf{p}+\mathbf{q}} + \epsilon_{\mathbf{p}}) \ . \tag{2.121}$$

As in (2.80) ff. we can calculate this using the Lindhard function:

$$\Im[\Sigma](k_F,\epsilon) = \frac{V_0^2}{(2\pi)^2}\int d\mathbf{q}\ \chi_2(q,\epsilon - E_{\mathbf{Q}-\mathbf{q}})\theta(\epsilon - E_{\mathbf{Q}-\mathbf{q}}) \tag{2.122}$$

We now restrict ourselves to the limit of small ϵ:

$$\epsilon \leq \frac{k_F^2}{2M} = \beta\mu \ . \tag{2.123}$$

Note that $\epsilon = \beta\mu$ corresponds to the pole of the noninteracting hole spectral function at $\Omega = E_G + k_F^2/2M$.

We introduce dimensionless variables:

$$\alpha = \epsilon/\mu \ , \qquad x = q/k_F \tag{2.124}$$

and consider the resulting factor $\chi_2\left(x, \alpha - \beta(\mathbf{e_Q} - \mathbf{x})^2\right)\theta\left((\alpha - \beta(\mathbf{e_Q} - \mathbf{x})^2)\right)$, where $\mathbf{e_Q}$ is the unit vector in $\mathbf{Q}$ - direction.

(2.83) shows that for any frequency ω we can write

$$\chi_2\left(x, \omega\right) = \chi_2^a(x, \omega) \qquad \text{for} \quad 0 < \omega < -x^2 + 2x \ , \tag{2.125}$$

where we just have rewritten the boundaries for $\chi_2^a(x, \omega)$. A consideration of higher derivatives in ω further shows that for $\omega \ll -x^2 + 2x$ the approximation of $\chi_2^a(x, \omega)$ by it's leading expansion in ω as in (2.88) is justified.

In our case of interest we can estimate the maximum value of $\alpha - \beta(\mathbf{e_Q} - \mathbf{x})^2$ as:

$$\alpha - \beta(\mathbf{e_Q} - \mathbf{x})^2 \leq \beta - \beta(1 - x)^2 = \beta(-x^2 + 2x) \ll -x^2 + 2x \ . \tag{2.126}$$

Thus, we can replace χ_2 by the leading term of χ_2^a in (2.122). Changing variables:

$$\mathbf{y} = \mathbf{e_Q} - \mathbf{x} \ , \tag{2.127}$$

we obtain:

$$\Im[\Sigma](k_F, \alpha) = \tag{2.128}$$
$$-\theta(\alpha) \cdot \frac{2g^2\mu}{\pi} \int_0^{2\pi} d\phi \int_0^{\sqrt{\alpha/\beta}} dy \frac{y(\alpha - \beta y^2)}{\sqrt{4 - (1 - 2y\cos(\phi) + y^2)}} \cdot \frac{1}{\sqrt{(1 - 2y\cos(\phi) + y^2)}} \ .$$

First, we calculate the leading behaviour of $\Im[\Sigma](k_F, \alpha)$ in α for $\alpha \ll \beta$. This is easily done, since we can then approximate the square roots as constants. The result then reads:

$$\Im[\Sigma](k_F, \epsilon) = -\theta(\epsilon) \cdot \frac{1}{\sqrt{3}} g^2 \beta\mu \frac{\epsilon^2}{(\beta\mu)^2} \ , \qquad \epsilon \ll \beta\mu \ . \tag{2.129}$$

Numerical integration of (2.128) shows that the Ansatz (2.129) is actually relatively accurate even for $\epsilon \lesssim \beta\mu$. A comparison of the two methods is shown in Fig. 2.16.

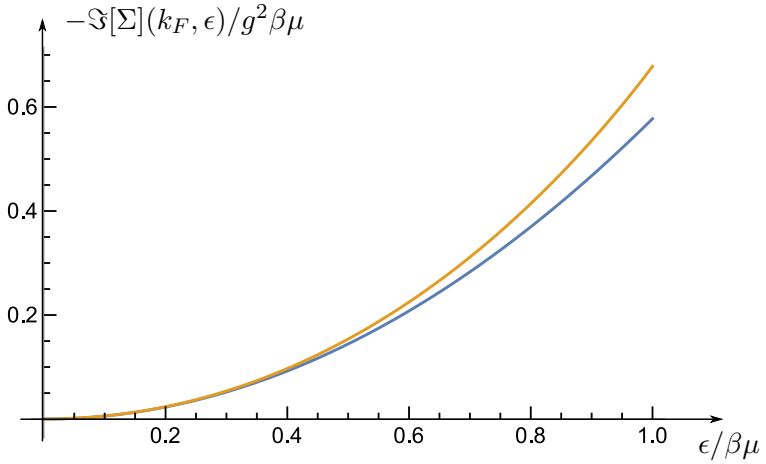

Figure 2.16.: Evaluation of $\Im[\Sigma](k_F, \epsilon)$. Blue curve: perturbative Ansatz (2.129). Yellow curve: numerical integration of (2.128).

As an important result we will use later on, we note that

$$\Im[\Sigma](k_F, \beta\mu) \simeq -\frac{1}{\sqrt{3}} g^2 \beta\mu \ . \tag{2.130}$$

This means that the hole-propagator for $Q = k_F$ has a finite life-time (which is also true for any $Q > 0$): A hole with $Q = k_F$ is no longer the ground state, it can decay into electron-hole excitations and a hole with $Q < k_F$.

We will not attempt a proper evaluation of $\Im[\Sigma](k_F, \epsilon)$ for $\epsilon > \beta\mu$. Of course, since in the limit $Q \to 0$ we must recover the results of section 2.2.2, the power law in $\Im[\Sigma](k_F, \epsilon)$ should change for $\beta\mu < \epsilon < E_R = 4\beta\mu$. However, this change will be only marginal since there is no clear separation of scales.

In the limit $\epsilon \gg \beta\mu$ it is also clear that $\Im[\Sigma](k_F, \epsilon)$ approaches the infinite mass result (2.53).

Now we have to calculate $\Re[\Sigma](k_F, \epsilon)$. There will be two contributions. The constant part $\Re[\Sigma](k_F, 0)$ can only renormalize the gap and the VB hole mass, and we assume that this is already accounted for. The frequency dependent part, which we can obtain applying Kramers-Kronig relations on $\Im[\Sigma](k_F, \epsilon)$, for small enegies will approximately vary as:

$$\Re[\Sigma](k_F, \epsilon) \simeq g^2 \frac{\epsilon^2}{\beta\mu} \log(\epsilon/\xi) \qquad \epsilon < \beta\mu \ . \tag{2.131}$$

For $\epsilon \ll \beta\mu$ this term is clearly irrelevant. For $\epsilon \simeq \beta\mu = k_F^2/2M$, the pole of the bare hole spectral function, it can have a sizeable contribution. Effectively, it shifts the pole by

$$\Delta E = \beta\mu \cdot g^2 \log(\beta) + \mathcal{O}([g^2 \log(\beta)]^2 \cdot \beta\mu) \ . \tag{2.132}$$

We will now restrict ourselves to the regime where

$$|g^2 \log(\beta)| \ll 1 \ . \tag{2.133}$$

In this regime, the shift of the pole is negligble; most importantly, the maximal value and the width of the spectral function $\mathcal{A}_h(k_F, \epsilon)$ are unaffected by $\Re[\Sigma](k_F, \epsilon)$.

Finally, if ϵ becomes large, as in the infinite mass case the inclusion of $\Re[\Sigma](k_F, \epsilon)$ can only lead to $\mathcal{O}(g^4)$ corrections for $\mathcal{A}_h(k_F, \epsilon)$, which we do not take into account (c.f. (2.57)). Thus, in the regime under consideration we can consistently disregard $\Re[\Sigma](k_F, \epsilon)$ alltogether. Our general expression for the spectral function therefore reads:

$$\mathcal{A}_h(k_F, \epsilon) = \frac{-2\Im[\Sigma](k_F, \epsilon)}{(\epsilon - \beta\mu)^2 + (\Im[\Sigma](k_F, \epsilon))^2} \ , \tag{2.134}$$

Inserting the low-energy form (2.129) then immediately shows the properties

$$\mathcal{A}_h(k_F, \epsilon) = \theta(\epsilon) \frac{g^2}{\sqrt{3}} \frac{\epsilon^2}{(\beta\mu)^3} \qquad \epsilon \ll \beta\mu \tag{2.135}$$

$$\max(\mathcal{A}_h(k_F, \epsilon)) = \mathcal{A}_h(k_F, \beta\mu) = 2\sqrt{3}/(g^2 \beta\mu) \ . \tag{2.136}$$

If we use a self-energy expression which continuously interpolates between the low-energy limit (2.129) and the high-energy limit (2.53), we obtain a spectral function as shown in Fig. 2.17.

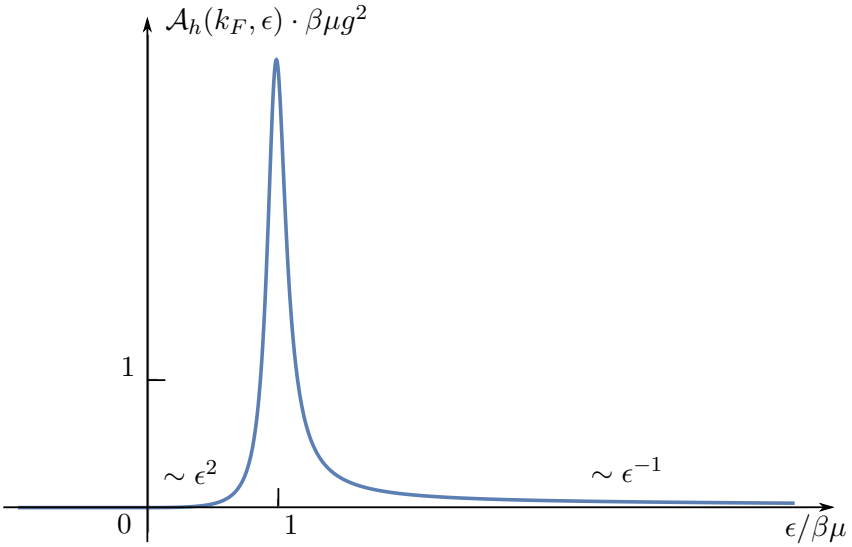

Figure 2.17.: Dyson equation result for the hole spectral function with $Q = k_F$. Used parameter: $g = 0.4$.

To summarize, we have found that the hole spectral function $\mathcal{A}_h(k_F, \epsilon)$ is of finite height due to the decay into CB electron-hole excitations, and it vanishes at $\epsilon = 0$, which is the minimal energy for hole creation.

3. Absorption in the Fermi-edge regime: Mahan approach

3.1. Historical overview

Having obtained an understanding of the underlying physics of the hole propagator, let us now proceed with the calculation of the absorption in the Fermi-edge regime. This has been a major problem of interest since the late sixties, studied with a large variety of methods, both analytical and numerical. However, usually it was considered under the simplifying assumption of infinite VB hole mass, which we are going to lift.

Let us first give a short overview over the theoretical state of the art and give some references; detailed evaluations will be shown in subsequent sections.

In the infinite mass case, the first seminal contribution was made by Mahan [6] in 1967, who already correctly identified the leading behaviour. Near the threshold $\omega_T := E_G + \mu$, the absorption behaves as a power law:

$$A(\omega) \sim (\omega - \omega_T)^{-2g} \ . \tag{3.1}$$

Mahan used a diagrammatical method; an extended and more self-consistent diagrammatical calculation using so-called *Parquet equations* was achieved in 1969 by Nozières et al. [7], [8] in the first two of a series of three outstanding papers. In the third paper [9], Nozières and de Dominicis were able to reduce the question to a one-body problem, similar as shown in section 2.1.3 when we erased the hole lines. They then calculated the power law exponent in terms of the scattering phase shift δ, obtaining:

$$A(\omega) \sim (\omega - \omega_T)^{(\delta/\pi - 1)^2 - 1} \ . \tag{3.2}$$

In honor of Mahan, Nozières and De Dominicis the *x-ray-edge*-problem is also frequently called *MND-problem*.

A useful interpretation of the power law in (3.2) was given by Hopfield [39] (1969): As for the hole propagator, the term δ/π describes the number of electrons displaced by the hole potential according to Friedel's sum rule as we discussed starting from (2.15). In addition, in a photon absorption process an electron is excited from the VB to the CB; this additional electron is accounted for by the extra term -1 added to the phase-shift. This rule of counting electrons has also been applied with success to other situtions. More examples for the applications of this so-called *Hopfield rule of thumb* can be found in Ref. [29].

As discussed before, for small couplings g one has $\delta/\pi = g + \mathcal{O}(g^3)$, therefore in second order in g (3.2) reads:

$$A(\omega) \sim (\omega - \omega_T)^{g^2 - 2g} \ , \tag{3.3}$$

disregarding spin. The term g^2 can be seen as a remainder of the Anderson orthogonality discussed in the previous chapter; it is therefore often called *Anderson contribution*,

while the term $-2g$ is called *Mahan contribution*. Our perturbative calculation will be restricted to the latter.

There have been many further important results for the x-ray-edge problem. Of these we want to mention the bosonization treatment by Schotte and Schotte [33] (1969) and the approach of Combescot and Nozières [40] (1971), who tranformed the problem to a calculation of Slater-determinants, and were able to go beyond the FER, allowing μ to be small, but finite.

It should be noted that the analytical methods are mainly concerned with a spectral region asymptotically close to the threshold; for the full absorption line-shape numerical methods are needed. Such calculations and a detailed review of many further results can be found in Ref. [41] (1990) by Othaka and Tanabe.

Now let us mention the treatments in the case of finite VB hole mass. First, there is the diagrammatic treatment of Gavoret, Nozières et al. [27] (1969) in 3D. This treatment was further discussed and extended by Ruckenstein and Schmitt-Rink [42] (1987), also adding some results in 2D. We will present a detailed calculation of the absorption in 2D based on these two papers in chapter 4. To anticipate the result, the major effect of the finite mass is to cut and wash out the edge singularity. A short physical discussion of this outcome is found in a late paper by Noziéres [38] (1994).

Furthermore, there are some numerical approaches. The first relevant one is by Uenoyama and Sham [43] (1990), based on a concise semianalytical functional integration. The resulting absorption, however, is only shown at very strong magnetic fields and is rather featureless.

The second important study we are aware of is by Hawrylak [44] (1990). He also accounted for effects beyond our treatment, like band gap renormalization and a more realistic electron-hole interaction. The effects of these modifications are difficult to estimate; however, the major point that the finite mass will cut the singularity is confirmed in his paper.

3.2. Mahan approach for the infinite mass case

We will now begin our evaluation, starting from the original approach by Mahan [6]. As we will see, this treatment has to be regarded only as a first guess. However, it will allow for a straightforward generalization to final masses, that already contains the most important physical ingredients. A more elaborate treatment, based on Ref. [27], will be presented in the next chapter.

Let us first sketch the calculation in the infinite mass case, following Ref. [21], section 9.3.2. We will not show the calculations in detail, since the infinite mass case can be easily recovered from the finite mass case we will calculate afterwards.

We switch back to the VB electron picture, starting from the Hamiltonian with the simple form of interaction (2.5). In momentum space, our Hamiltonian then reads:

$$H_\infty = -E_G b^\dagger b + \sum_{\mathbf{k}} \epsilon_{\mathbf{k}} a^\dagger_{\mathbf{k}} a_{\mathbf{k}} - \frac{V_0}{\mathcal{S}} \sum_{\mathbf{k},\mathbf{p}} a^\dagger_{\mathbf{k}} a^\dagger_{\mathbf{p}} b b^\dagger \ . \tag{3.4}$$

We will now calculate the photon self-energy in linear response. As announced in section (1.6), we will set the photon momentum $\mathbf{q}$ to zero. Then we have to evaluate

(see (1.33)):

$$\Pi(\Omega) = -iM_0^2 \int dt \exp(i\Omega t) \sum_{\mathbf{p}_1,\mathbf{p}_2} \langle 0|\hat{T}\left\{b^\dagger(t)a_{\mathbf{p}_1}(t)a^\dagger_{\mathbf{p}_2}(0)b(0)\right\}|0\rangle \ . \tag{3.5}$$

Exactly as in section 1.5, the zeroth order result corresponds to the bare electron-electron-bubble shown in Fig. 3.1.

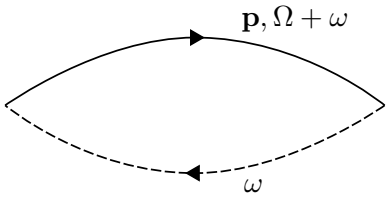

Figure 3.1.: Zeroth order electron-hole bubble.

The bare VB propagator in the FER for infinite hole mass reads:

$$G_v^{(0)}(\omega) = \frac{1}{\omega + E_G - i0^+} \ . \tag{3.6}$$

We note that in the electron picture VB propagators must be purely advanced, which will also be the case for finite mass.

Using this Green's function and carrying out the frequency integration as discussed in section 2.2.3, $\Pi^{(0)}(\Omega)$ reads:

$$\begin{aligned}\Pi^{(0)}(\Omega) =& M_0^2 \sum_{\mathbf{p}} \frac{1 - n_F(\epsilon_{\mathbf{p}})}{\Omega - E_G - \epsilon_{\mathbf{p}} + i0^+} = M_0^2 \mathcal{S}\rho \int_\mu^{\mu+\xi} d\epsilon_{\mathbf{p}} \frac{1}{\Omega - E_G - \epsilon_{\mathbf{p}} + i0^+} \\ =& \gamma_0 \rho \log\left(\frac{\Omega - E_G - \mu + i0^+}{\Omega - E_G - \mu - \xi + i0^+}\right) \ ,\end{aligned} \tag{3.7}$$

where we used the definition of $\gamma_0 = M_0^2\mathcal{S}$ as in (1.53).

We now concentrate on the energy regime $\Omega \gtrsim E_G + \mu$. It is clear e.g. from the FER bandstructure picture of Fig. 1.11, that the absorption $A(\Omega)$ will set in at $E_G + \mu$ in the noninteracting case. For reasons to be explained later, we will call $\Omega_I = E_G + \mu$ the *indirect threshold* . From now on we will phrase all expressions in terms of the detuning ϵ from this threshold, which we assume to be small. More precisely, we will use that

$$\epsilon = \Omega - \Omega_I \ll \xi \ . \tag{3.8}$$

Thus, for $\Pi^{(0)}(\Omega)$ we obtain in terms of ϵ:

$$\Pi^{(0)}(\epsilon) = \gamma_0 \rho \log\left(\frac{-\epsilon - i0^+}{\xi}\right) \ , \tag{3.9}$$

which leads to a zeroth order absorption

$$A^{(0)}(\epsilon) = \gamma_0 \pi \rho \cdot \theta(\epsilon) \ . \tag{3.10}$$

Let us proceed with higher orders. First, there are the ladder diagrams which appeared in the calculation of the Wannier-exciton. Let us redraw them:

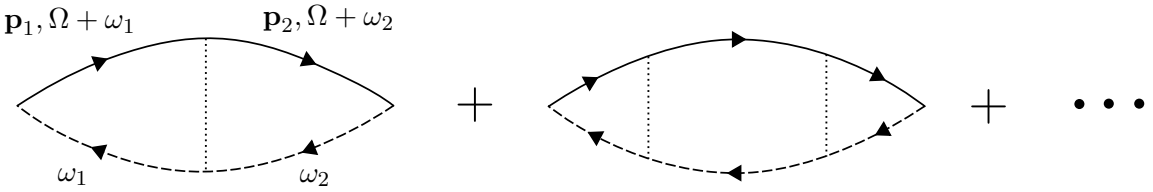

Figure 3.2.: The series of ladder diagrams

Using our momentum-independent interaction, their calculation is simple since all integrals just factorize. Fixing the signs with Wick's theorem, the resulting contribution of an n-th order ladder diagram reads:

$$\Pi^{(n)}_{\text{Ladder}}(\epsilon) = \gamma_0 \rho \cdot (-g)^n \log\left(\frac{-\epsilon - i0^+}{\xi}\right)^{n+1} . \tag{3.11}$$

A first guess for the absorption can be obtained by just taking into account the series of ladder diagrams, as was first done by Mahan [45]. Accordingly, this Ansatz is called *ladder approximation*. Keeping the decay rate 0^+ finite troughout the ladder summation, one arrives at the following expression for the absorption:

$$A_{\text{Ladder}}(\epsilon) = -\Im\left[\sum_{n=0}^{\infty} \Pi^{(n)}_{\text{Ladder}}(\epsilon)\right] = \frac{\gamma_0 \rho B}{(1+gC)^2 + (gB)^2} , \tag{3.12}$$

where

$$B(\delta) = \left(\pi/2 + \arctan\left(\frac{\epsilon}{0^+}\right)\right) \qquad \text{and} \qquad C(\epsilon) = \frac{1}{2}\log\left(\frac{\epsilon^2 + (0^+)^2}{\xi^2}\right) . \tag{3.13}$$

One can check that $A_{\text{Ladder}}(\epsilon)$ has a singularity below treshold for

$$\epsilon = -\xi \exp(-1/g) =: -E_B . \tag{3.14}$$

This pole corresponds to a bound state and is a remainder of the Wannier-excitons in our simplified interaction. It is called *Mahan-exciton* in the literature. Furthermore, $A_{\text{Ladder}}(\epsilon)$ has a a continuous onset at $\epsilon > 0$. A typical plot of A_{Ladder} is shown in Fig. 3.3.

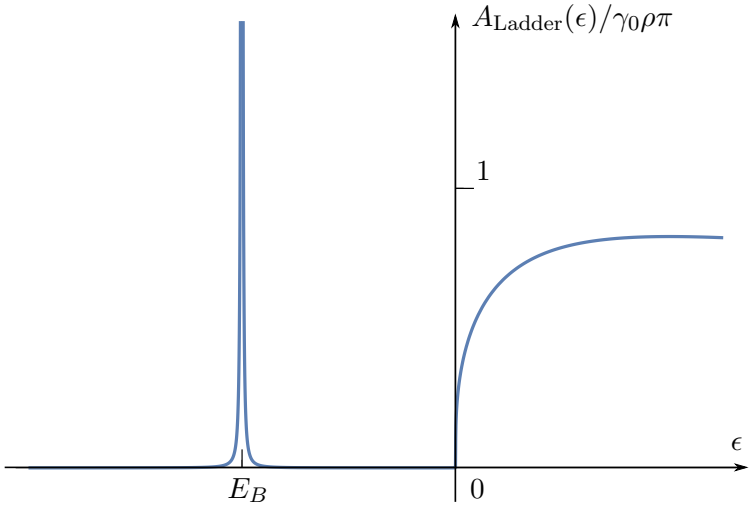

Figure 3.3.: Absorption in the ladder approximation.

One should compare this plot to the Wannier-exciton case shown in Fig. 1.8.

For nonzero μ, keeping only the ladder diagrams is unphysical: As was discussed in section 1.5, the ladder diagrams only contain CB electrons propagating forwards in time, thus no particle-hole excitations of the CB Fermi-sea are taken into account. As μ is increased, these scatterings become more and more important, blurring the thresholds; therefore, the frequency space between the Mahan-exciton and the continuous threshold is gradually filled in. This is sketched in Fig. 3.4.

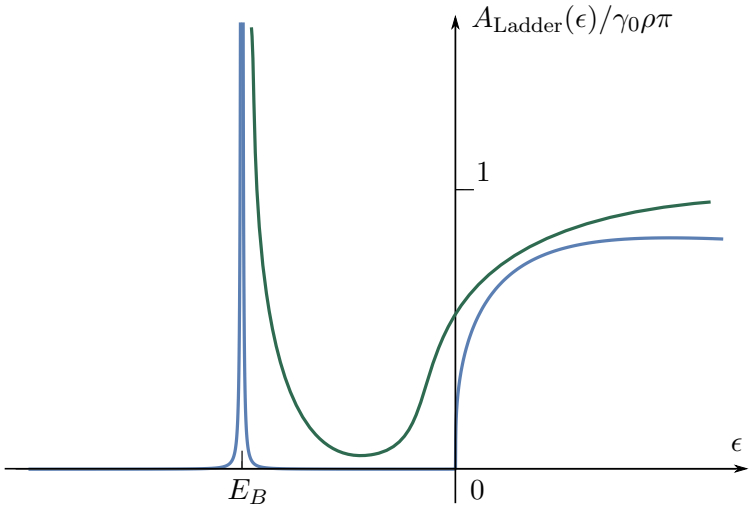

Figure 3.4.: Qualitative change of the absorption as μ is increased. The threshold shift is disregarded. This picture was adapted from Ref. [40].

Finally, in the FER, which corresponds to $\mu \gg E_B$, one can expect that no remainder of two separate thresholds is left, and the exciton pole is turned into a power law, in the same way as was the case for infinite mass holes.

A detailed discussion of the absorption in the presence of an exciton in an intermediate regime $\mu \simeq E_B$ is found in Ref. [40] .

Due to it's simplicity, the ladder approximation is sometimes used for the calculation of finite hole mass absorption spectra even for large chemical potentials (c.f. Refs. [46], [47]). However, in the FER this procedure is questionable, since excitonic effects are strongly overestimated (see also below).

Let us now extend the treatment beyond the ladder approximation. From (3.11) we infer that the quantity controlling the perturbative expansion is

$$g \log\left(\frac{-\epsilon - i0^+}{\xi}\right) =: gL \ , \tag{3.15}$$

which is divergent as $\epsilon \to 0$.

Mahan [6] proposed the following procedure, called *leading log summation*: In the calculation of $\Pi(\epsilon)$ for small ϵ, to each given order in the interaction we keep only the terms of the largest appearing power in gL: In n-th order, these will be of the form

$$(gL)^n \cdot L \ . \tag{3.16}$$

As elucidated in the first of the three seminal papers by Nozières [7], such a procedure can only be valid in a strict sense for not to small ϵ s.t. $gL \simeq 1$. Namely, for $gL \gg 1$, i.e $L \gg 1/g$, a quantity like e.g. g^3L^3 can be of the same order as gL^2, s.t. disregarding it makes no sense. An extension of the leading-log summation all the way down to $\epsilon = 0$ was accomplished in the second paper by Nozières, [8], via a consistent treatment of unknown divergent parameters. We will, however, not employ this method here.

Assuming $gL \simeq 1$ and keeping only the leading terms already excludes VB self-energy diagrams: As shown in the previous chapter in second order, c.f. (2.51), the contribution of the self-energy diagram of Fig. 2.15 is $g^2L \cdot \epsilon$, which is subleading as compared to the term ϵ that appears in the denominator of the VB-Green's function. This statement also holds to all orders [7]. Therefore, within the Mahan treatment we only take into account vertex corrections.

Lastly, we remark that in the leading-log summation it is difficult to keep track of the phases of the complex logarithm, since calculations are done with logarithmic accuracy; However, the phases can be restored (which we will do implicitly) using the same arguments as were discussed starting from (2.54) ff.

Let us apply the leading-log summation. The first diagram that contributes as $(gL)^n \cdot L$ and is not a ladder diagram, is the so-called crossed diagram shown in Fig. 3.5. It corresponds to the standard hole-hole channel.

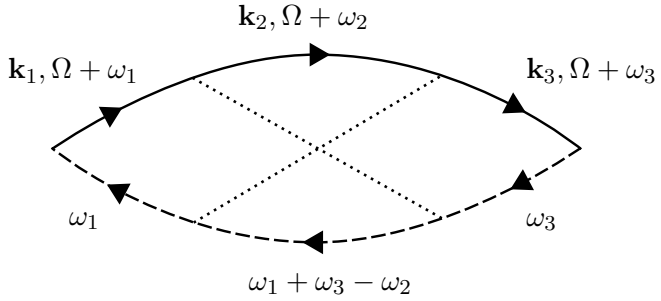

Figure 3.5.: Second order crossed diagram.

Since the interactions are instantaneous, in the time-domain it is straightforwardly seen that this diagram contains a CB hole; Thus, the crossed diagram involves a CB Fermi-sea electron-hole excitation, which is also called *Fermi-sea shakeup*.

This diagram can be calculated with logarithmic accurracy, as will be shown for the finite mass case in appendix A. In this calculation, one crucial technical trick is employed: When dealing with logarithms of the form $\log(x+y)$, $x, y > 0$, with logarithmic accuracy one can write:

$$\log(x + y) \simeq \log(\max(x, y)) \ , \tag{3.17}$$

which significantly simplifies all integrals. With this simplification, the contribution of the crossed diagram is found to be:

$$\Pi_{\text{cross}}(\epsilon) = -\frac{1}{3}\gamma_0\rho \cdot g^2L^3 \ , \tag{3.18}$$

which is $(-1/3)$ times the contribution of the second order ladder diagram.

Now we have obtained all diagrams that contribute to second order. Following Mahan (he actually also calculated the third order), we can guess the full series for $\Pi(\epsilon)$ from these terms:

$$\Pi(\epsilon) = \frac{\gamma_0\rho}{g} \cdot \left(gL - (gL)^2 + 2/3 \cdot (gL)^3 + ...\right) \overset{\text{guess}}{=} \frac{\gamma_0\rho}{2g} \left(1 - \exp(-2gL)\right) \ . \tag{3.19}$$

In the series of papers by Nozières and by many other authors it was later found that this guess is indeed correct. For later use, let us explicitly denote the real part:

$$\Re\left[\Pi\right](\epsilon) = \frac{\gamma_0\rho}{2g} \left(1 - \left(\frac{|\epsilon|}{\xi}\right)^{-2g}\right) \ . \tag{3.20}$$

The absorption, as found from (3.19), then reads:

$$A(\epsilon) = -\Im[\Pi](\epsilon) = \frac{\gamma_0\rho}{2g} \cdot \exp\left[-2g \log\left(\epsilon/\xi\right)\right] \cdot \sin(2\pi g) \cdot \theta(\epsilon) \simeq \gamma_0\rho\pi \left(\epsilon/\xi\right)^{-2g} \cdot \theta(\epsilon) \ . \tag{3.21}$$

As expected, the exciton pole has been turned into a power law, and the two thresholds (bound state and continuous onset) have merged. This power law is commonly referred to as *Fermi-edge singularity*.

3.3. Mahan approach for the finite mass case

3.3.1. VB Green's function renormalization

Let us now discuss the finite mass case. A first possible modification is to take into account the renormalization of the VB electron propagator. This is also consistent with the leading-log scheme: For finite momenta, the self-energy at the pole of the VB Green's function will not vanish, and thus will be the leading term.

As apparent e.g. from the integral in (3.7), the Fermi-edge absorption is dominated by momenta close to k_F. Thus, the results of section 2.2.3 are of relevance. As simplest Ansatz, we can substitute the formula (2.130) as inverse lifetime:

$$i\Gamma = ig^2\beta\mu \ , \tag{3.22}$$

where we have disregarded the numerical prefactors, and a change of sign occurs due to the switch to the electron picture. Within this simple treatment, higher order self-energy diagrams can only further modify the lifetime with prefactors that are at least $\mathcal{O}(g^3)$, s.t. the Ansatz (3.22) will be sufficient for us.

Let us also recall that the Ansatz (3.22) is only reliable for $|g^2 \log(\beta)| \ll 1$. (see discussion on page 57).

Substituting $i\Gamma$ into the general formula for Green's functions (1.42), we obtain:

$$G_v(\mathbf{k}, \omega) = \frac{1 - n_F(\omega)}{\omega + E_G + E_\mathbf{k} + i\Gamma} + \frac{n_F(\omega)}{\omega + E_G + E_\mathbf{k} - i\Gamma} \ . \tag{3.23}$$

(3.23) has a retarded and advanced component; however, as remarked before, G_v should be purely advanced.

Introducing a small but finite constant hole self-energy $i\Gamma$ violates this property. But this violation is only negligibly small. Namely the retarded part

$$G_v^{\mathrm{R}}(\mathbf{k},\omega) = \frac{1-n_F(\omega)}{\omega + E_G + E_{\mathbf{k}} + i\Gamma} \tag{3.24}$$

consists of two factors. Firstly $1-n_F(\omega) = \theta(\omega-\mu)$. Secondly we have $(\omega + E_G + E_{\mathbf{k}} + i\Gamma)^{-1}$. It's absolute value reads:

$$\mathrm{Abs}(\omega) := \left|(\omega + E_G + E_{\mathbf{k}} + i\Gamma)^{-1}\right| = \frac{1}{\sqrt{(\omega + E_G + E_{\mathbf{k}})^2 + \Gamma^2}} \ , \tag{3.25}$$

which is peaked in the interval $[-E_G - E_{\mathbf{k}} - \Gamma, -E_G - E_{\mathbf{k}} + \Gamma]$. We have

$$\Gamma \ll \mu, \xi \ll E_G \ .$$

Hence, we can savely ignore the retarded part alltogether, since the support of the two factors is practically disjunct (see Fig. 3.6 below).

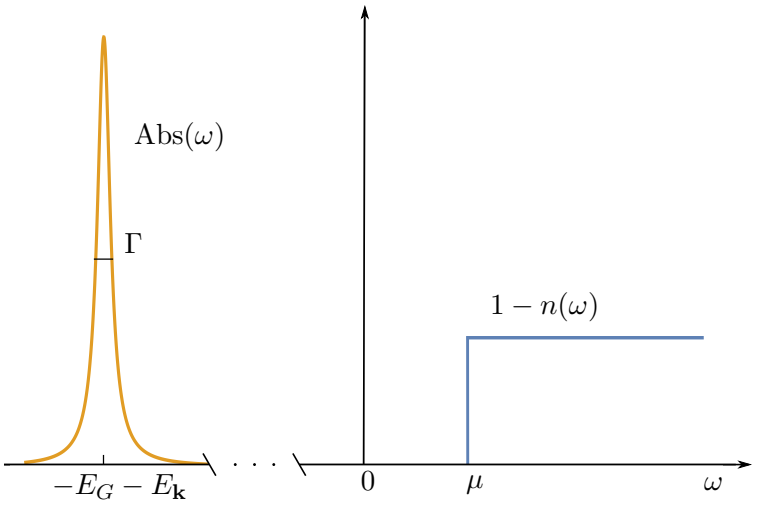

Figure 3.6.: Sketch of the factors $\mathrm{Abs}(\omega)$ and $1-n_F(\omega)$ appearing in G_v^R.

By the same argument we can set $n_F(\omega) = 1$ in the advanced part of G_v, obtaining:

$$G_v(\mathbf{k},\omega) \simeq G_v^A(\mathbf{k},\omega) \simeq \frac{1}{\omega + E_G + E_{\mathbf{k}} - i\Gamma} \ . \tag{3.26}$$

Using this formula, we can first calculate the basic bubble of Fig. 3.1. Since the external momentum is zero, the CB and VB electron must have the same momentum, s.t. the momentum angular integration is again trivial. As a result, we obtain the following expression:

$$\Pi^{(0)}(\Omega) \simeq \gamma_0 \rho \log\left(\frac{\Omega - \mu(1+\beta) - E_G + i\Gamma}{\Omega - \xi(1+\beta) - E_G + i\Gamma}\right) \ , \tag{3.27}$$

where we have disregarded a prefactor of $1/(1+\beta)$.

We now observe that the real part of the logarithm will be maximal for

$$\Omega = E_G + \mu(1+\beta) := \Omega_D \ , \tag{3.28}$$

with the *direct threshold* Ω_D, also called *Burstein-edge* [48].

The appearance of this direct threshold has to be understood as follows: If we let the decay rate Γ go to zero, the noninteracting absorption will set in for $\Omega = \Omega_D$ due to Pauli-blocking of the electron lifted to the CB. This means that, in a noninteracting picture, the lowest possible momentum of the VB hole created via photon absorption is $Q = k_F$. However, due to scatterings, such a VB hole will decay into holes with lower momentum and low-energy CB electron-hole excitations, as was discussed in the previous chapter. This decay actually lowers the threshold for the absorption to

$$\Omega = E_G + \mu := \Omega_I \ , \tag{3.29}$$

which is therefore called the *indirect threshold* Ω_I, analogous to the hole propagator case. A sketch of these thresholds is shown in Fig. 3.7.

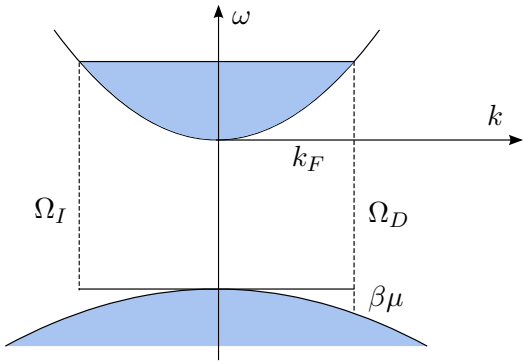

Figure 3.7.: Sketch of the two thresholds of the absorption.

However, within our present treatment with a constant self-energy, we will not recover the onset of the absorption at Ω_I; this will be left to the more refined method of the next chapter. Our current simple approach will only yield the correct behaviour near Ω_D. Thus, in this section it will be convenient to measure energies in terms of the small detuning from Ω_D:

$$\Omega = \Omega_D + \nu \ , \qquad \nu \ll \xi \ . \tag{3.30}$$

In terms of this detuning, the zeroth order absorption coming from (3.27) reads (by zeroth order we of course actually mean zeroth order vertex correction):

$$A^{(0)}(\nu) = \gamma_0 \rho \left(\frac{\pi}{2} + \arctan\left(\frac{\nu}{\Gamma}\right)\right) =: \gamma_0 \rho \pi \cdot \theta_\Gamma(\nu) \ . \tag{3.31}$$

It is a θ-function of width Γ. A plot of this function will be shown in Fig. 3.11.

3.3.2. Regimes of the coupling constant

We can now continue with the calculation of the ladder diagrams. Since the integrations again simply factorize, we immediately obtain:

$$\Pi^{(n)}_{\text{Ladder}}(\nu) = \gamma_0 \rho \cdot (-g)^n \log\left(\frac{-\nu - i\Gamma}{\xi}\right)^{n+1} \ . \tag{3.32}$$

This expression shows that the maximal value of the parameter controlling the leading-log summation is now

$$g \log\left(\beta\mu g^2/\xi\right) \simeq g \log\left(\beta g^2\right) \ , \tag{3.33}$$

as opposed to the infinite mass case, where the logarithms are divergent at the threshold.

Let us consider different regimes of this parameter. A similar discussion is also found in Ref. [27]. There are three cases of interest:

- $\left|g \log(\beta g^2)\right| \ll 1$ corresponds to a perturbative regime: We do not have to sum up series of diagrams, just the lowest order diagrams will suffice.
- In the case $\left|g \log(\beta g^2)\right| \simeq 1$, however, a consistent summation of diagrams is needed, i.e. we are in a nonperturbative regime.
- Lastly, in the regime where $g|\log\left(\beta g^2\right)| \gg 1$, the absorption behaviour at the direct threshold is not within our reach, since in this regime the comparison of orders of g is meaningless, as discussed in the infinite mass case. We will then be limited to detunings $\nu \gg g^2\beta\mu$ s.t. $|g \log(\nu/\xi)| \gtrsim 1$. To enlarge the spectral range under control, one could attempt an analysis as in the second paper by Nozières [8], which however seems difficult for finite masses.

We now regard β as a fixed parameter, and see what happens as we increase g. Experimentally, g can be be tuned by a change of the chemical potential or by a variation of the external screening in the system.

The two regimes under control are therefore separated by a value of the coupling constant $g_1(\beta)$ s.t

$$|g_1 \log(\beta {g_1}^2)| = 1 \qquad \Rightarrow \qquad \beta = \exp(-1/g_1)/g_1^2 \ . \tag{3.34}$$

$g_1(\beta)$ can be found numerically as depicted in Fig. 3.8.

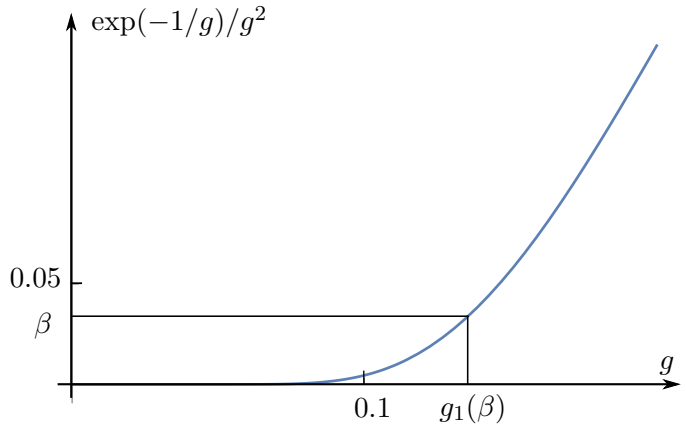

Figure 3.8.: Evaluation of the separating value $g_1(\beta)$.

This leads to a function $g_1(\beta)$ as shown in Fig. 3.9.

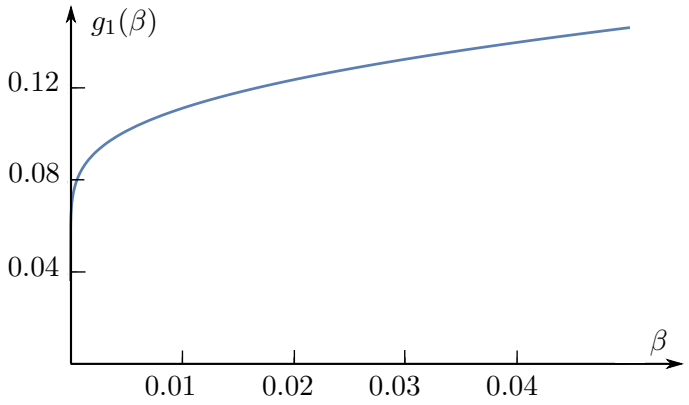

Figure 3.9.: Plot of $g_1(\beta)$ for very small values of β.

Thus, a sketch of the different regimes looks as follows:

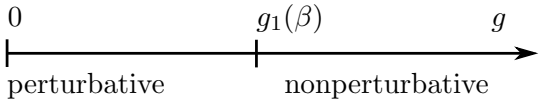

Figure 3.10.: The two regimes under consideration.

Clearly, the larger β, the larger the range $g < g_1(\beta)$ where a perturbative treatment is applicable: the appearing logarithmic singularities are renormalized by the hole decay rate Γ, which increases for increasing β.

3.3.3. Perturbative regime

For $g \ll g_1$, i.e. for very weak interactions, we have $g\left|\log(\beta g^2)\right| \ll 1$. Restoring μ, ξ in (3.34), we can also phrase this as

$$g^2\beta\mu \gg \xi \exp(-1/g) = E_B \ . \tag{3.35}$$

This means that the scattering-induced linewidth of the hole is much larger than the binding energy E_B of the Mahan exciton. It will therefore immediately decay, and no peak-structure is left. Since E_B is exponentially small in g, this will be the case for weak interactions.

A good approximation to the absorption in the perturbative regime $A_p(\nu)$ is already given by the zeroth order result (3.31). A typical plot is shown in Fig. 3.11.

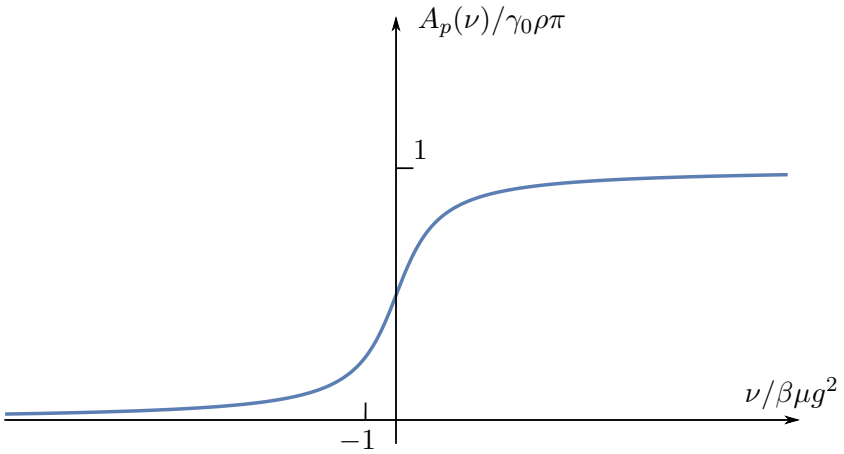

Figure 3.11.: Absorption in the perturbative regime in the Mahan approach.

3.3.4. Non-perturbative regime

Let us now continue with the second regime under control, where $|g\log(\beta g^2)| \simeq 1$ respectively $g \simeq g_1$, i.e. strong interactions. This regime is of course in perfect agreement with the assumption $g^2\log(\beta) \ll 1$ used for the definition of Γ.

We aim to reuse our leading-log approach. Thus, we have to calculate the crossed diagram. It is redrawn for finite mass in Fig. 3.12.

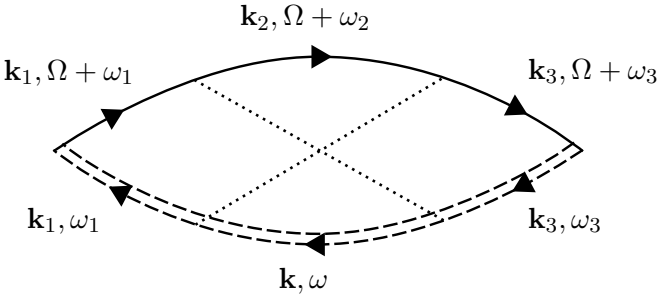

Figure 3.12.: Crossed diagram for finite hole mass. The dressed hole propagator is shown as a double line.

The three frequency integrals are easily calculated. As a result one obtains:

$$\Pi_{\text{cross}}(\Omega) = \frac{-\gamma_0 V_0^2}{(2\pi)^6} \int d\mathbf{k}_1 \int d\mathbf{k}_2 \int d\mathbf{k}_3 \, (1-n_F(\mathbf{k}_1))\, n_F(\mathbf{k}_2)\, (1-n_F(\mathbf{k}_3)) \tag{3.36}$$
$$\cdot \frac{1}{(\Omega + i\Gamma - \Omega_I - (\epsilon_{\mathbf{k}_1} - \mu) - E_{\mathbf{k}_1})\,(\Omega + i\Gamma - \Omega_I - (\epsilon_{\mathbf{k}_3} - \mu) - E_{\mathbf{k}_3})}$$
$$\cdot \frac{1}{(\Omega + i\Gamma - \Omega_I - (\epsilon_{\mathbf{k}_1} - \mu) - (\epsilon_{\mathbf{k}_3} - \mu) + (\epsilon_{\mathbf{k}_2} - \mu) - E_{\mathbf{k}_1+\mathbf{k}_3-\mathbf{k}_2})} \, .$$

We notice that the $\mathbf{k}_2$-integration runs over the occupied states, which again shows why this diagram was absent for a vanishing chemical potential μ.

The actual calculation of the crossed diagram is complicated due to the term $E_{\mathbf{k}_1+\mathbf{k}_3-\mathbf{k}_2}$. It is presented in appendix A. As an intermediate result, calculating the k_2 integral and

the two non-trivial angular integrals, one obtains a logarithm of the form:

$$\log\left(\frac{\nu-(\epsilon_{\mathbf{k}_1}-\mu)-(\epsilon_{\mathbf{k}_3}-\mu)+i\beta\mu}{-\mu}\right) , \tag{3.37}$$

again in terms of detuning ν.

The major difference in comparison to the ladder diagrams discussed before is the different type of cutoff for the logarithm: $\beta\mu$ instead of $\Gamma = g^2\beta\mu$. The reason for this new, stronger cutoff is the term $E_{\mathbf{k}_1+\mathbf{k}_3-\mathbf{k}_2}$; a logarithm which is only cut off by Γ would require this term to be of order Γ for most angles, which is clearly not the case.

The maximal value of the logarithm (3.37), for $k_1 = k_3 = k_F$ and $\nu = 0$, therefore reads $\log(\beta)$. The logarithms of the ladder diagrams, however, took the maximal value $\log(\beta g^2)$ at the direct treshold. To procede analogous to the infinite mass case, we need the two cutoffs to coincide. This will be the case with logarithmic accuracy as long as $\beta \ll g^2$. Thus, for a simple Mahan-type argument to work, we also need

$$g \gg \sqrt{\beta} = g_2(\beta) , \tag{3.38}$$

in addition to $g \simeq g_1$.

In principle, for $g_1(\beta) \simeq g \ll g_2(\beta)$, the ladder diagrams will be dominant as compared to the crossed diagrams in a narrow spectral range $\nu \simeq g^2\beta\mu$; for $\nu \simeq \beta\mu$ the diagrams will again be of the same order. To describe this regime, one could attempt a ladder approximation for small ν which continuously crosses over to the full series for larger ν. Let us call this method *consistent ladder approximation* (CLA). However, it will be shown below that the range of applicability for this method is very limited.

The discussed lower bounds and a rough sketch of the accessible regimes is shown in Fig. 3.13:

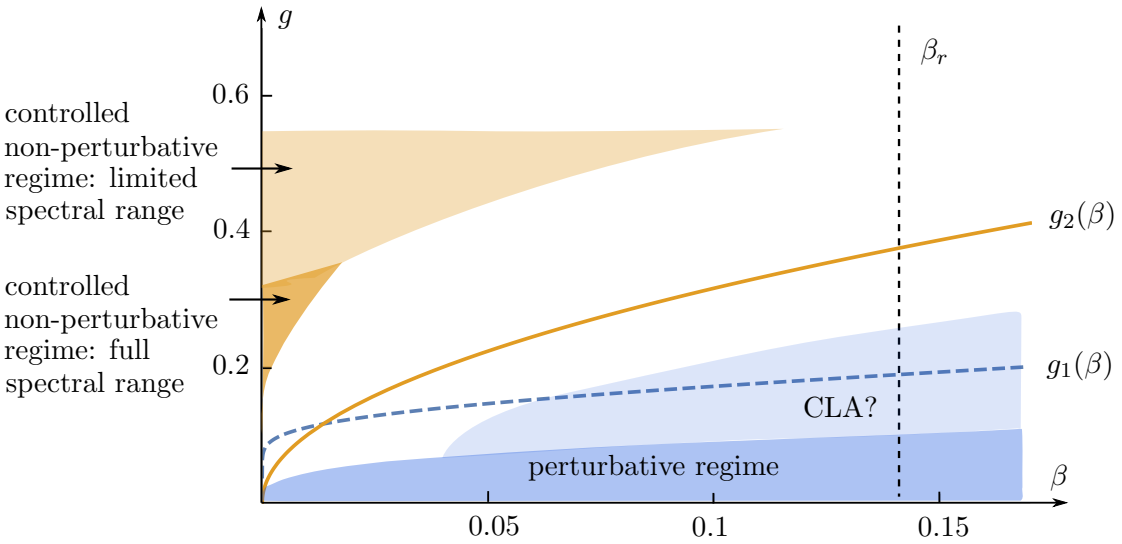

Figure 3.13.: Lower bounds on g. The blue dashed line corresponds to $g_1(\beta)$, the full yellow line to $g_2(\beta)$. $\beta_r \simeq 0.14$ corresponds to a realistic value of β in high-mobility GaAs samples.

If $g \ll g_1(\beta)$, we are in the perturbative regime discussed before. If $g_1(\beta) \simeq g \ll g_2(\beta)$, the CLA could be applied. However, as seen from Fig. 3.13, there is actually no clear theoretical regime for this method.

If $g_1(\beta), g_2(\beta) \simeq g$, the Mahan approach will be limited to frequencies $\nu > \beta\mu$, for which the ladder and crossed diagrams are of the same order. This "trivial" regime, in which we effectively cannot account for mass effects, is not depicted in Fig. 3.13.

If $g_1(\beta) \simeq g \gg g_2(\beta)$, we can apply the Mahan approach in the whole spectral range. Finally, if $g_1(\beta), g_2(\beta) \ll g$, the Mahan approach will be limited to frequencies ν s.t. $|g \log(\nu/\xi)| \simeq 1$.

It should be noted that we do not face any problems as long as g is small enough.

Unfortunately, the full range of applicability of the Mahan approach does not extend to realistic values of $\beta \simeq \beta_r$ in high-mobility GaAs samples as indicated in Fig (3.13). However, one can argue that there are several effects we have disregarded, which will further decrease the VB hole life-time. Among these are ([21], page 605):

- *Auger processes*: An electron from a higher band falls into the VB hole, transferring it's excess energy to other electrons.
- *photo-recombination*: Again the hole is filled by a higher band electron, but accompanied by the emission of a photon.
- *temperature effects*, especially phonon-coupling.

We can assume that this extra life-time decrease will enlarge the range of applicability of the perturbative regime; furthermore, for a smaller lifetime and thus higher self-energy Γ, one can expect that the cutoffs of the ladder and crossed diagrams coincide in a larger region in g-space, thus also increasing the suitable range for the Mahan approach.

Let us now continue with the regime where Mahan's approach does work, meaning that $\log(\beta g^2) \simeq \log(\beta)$. In this regime we can carry out the remaining integrals over k_1, k_3 in (3.36) without further difficulties. This calculation, shown in appendix A, leads to

$$\Pi_{\text{cross}}(\nu) = -\gamma_0 \rho g^2 \cdot \frac{1}{3} \log^3 \left(\frac{-\nu - i\beta\mu}{\xi} \right) . \tag{3.39}$$

We can then proceed in line with the infinite mass approach. As a result, the non-perturbative absorption A_{np} reads:

$$\begin{aligned} A_{np}(\nu) &= \frac{\gamma_0 \rho}{2g} \left(\frac{\xi}{\sqrt{\nu^2 + (\beta\mu)^2}} \right)^{2g} \sin \left[2g \left(\frac{\pi}{2} + \arctan \left(\frac{\nu}{\beta\mu} \right) \right) \right] \\ &\simeq \gamma_0 \rho \pi \left(\frac{\xi/(\beta\mu)}{\sqrt{(\nu/\beta\mu)^2 + 1}} \right)^{2g} \cdot \theta_{\beta\mu}(\nu) . \end{aligned} \tag{3.40}$$

Thus, we find that in the non-perturbative regime where the Mahan exciton binding energy is larger than the scattering induced linewidth Γ, an absoprtion peak remains, which is cut off by the typical hole kinetic energy $\beta\mu$. An exemplary plot of $A_{np}(\nu)$ is shown in Fig. 3.14:

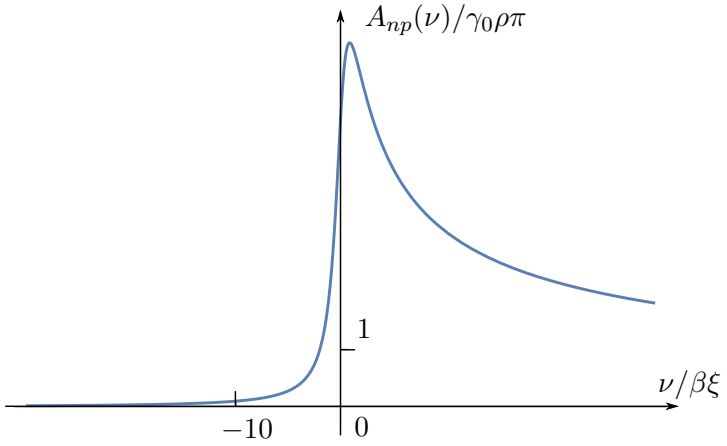

Figure 3.14.: Absorption as given by (3.40). Used parameters: $\beta = 0.01,\ g = 0.2,\ \xi = \mu$.

It should be noticed that on the ν-axis the scale is much larger that in Fig. 3.11. Furthermore, we want to emphasize again that the behaviour for $\nu < 0$ is inaccurate due to our choice of the constant hole self-energy. Therefore, we will postpone further plots to the next chapter where this inaccuracy will be corrected .

Let us make a final remark concerning the dimensional dependence: Actually, in the Mahan approach all calculations are independent of the space dimension except for the parameter g. This can be checked elementarily in the perturbative regime. In the non-perturbative regime under control, this is also seen easily: We proceeded as in the infinite mass problem, which is effectively one-dimensional, only taking into account the final hole linewidth. With logarithmic accuracy, the latter is proportional to $\beta\mu \simeq E_R$, i.e. the recoil energy, which is again independent of the dimension.

4. Absorption in the Fermi-edge regime: Nozières approach

Let us now improve on the simplistic Mahan approach, carrying over the treatment of Ref. [27] to 2D. This will involve two major points: First, we will compute the behaviour of the absorption near the indirect threshold $E_G + \mu$, which can be done perturbatively. For the absorption A this will yield a smeared theta-function with the correct asymptotic behaviour near the indirect threshold Ω_I: $A(\Omega) \sim g^2(\Omega - \Omega_I)^3$.

Second, we will actually calculate the power law at the direct threshold $E_G + \mu(1+\beta)$, solving a Bethe-Salpeter vertex equation.

4.1. Perturbative regime

The distinction between the perturbative and non-perturbative regimes made in the last chapter is still valid: our constant self-energy $i\Gamma$ was correct near the direct threshold, and, therefore, the maximal value attained by the logarithms which we used to distinguish the regimes is correct.

Let us first consider the perturbative-regime $\Gamma \gg E_B$, where no exciton-like peak remains. Near the direct threshold Ω_D, the only diagram contributing is the basic bubble with the VB propagator dressed with the self-energy of Fig. 2.15, for it contains the minimal number of occurences of the small parameter $g\log(\beta g^2)$. Near the indirect threshold Ω_I, in leading order g^2, also the bare crossed diagram of Fig. 3.5 has to be taken into account.

4.1.1. Absorption close to the indirect theshold

To begin with, we consider energies very close to Ω_I. In terms of detuning ϵ from Ω_I, we thus aim to find the leading behaviour of $A(\epsilon)$ in ϵ for $\epsilon \ll \beta\mu$. Similar calculations were also performed in [42], in 3D and 2D, where also electron-electron interactions were taken into account. Their contribution is found to be smaller by a factor of β, which allows us to disregard them.

There are two relevant diagrams. First, we have the crossed diagram with bare VB electron lines. Computing the frequency integrals, we obtain (3.36) with $i\Gamma$ replaced by $i0^+$.

The second contribution comes from the diagram shown in Fig. 4.1.

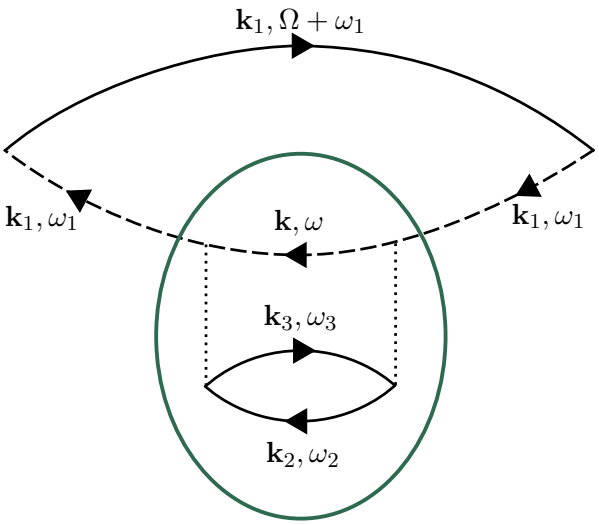

Figure 4.1.: Self-energy-type diagram contributing to the absorbtion at the indirect threshold. The green ellipsis marks the self-energy part.

For later reference we first denote the self-energy part, which is the same as in (2.120), except for the general incoming momentum $\mathbf{k}_1$ and the fact that we are working in the electron picture now. After two frequency integrations, it reads:

$$\Sigma(\mathbf{k}_1, \omega_1) = \frac{2V_0^2}{(2\pi)^4} \int\int d\mathbf{k}_2 \; d\mathbf{k}_3 \frac{(1 - n_F(\epsilon_{\mathbf{k}_3}))n_F(\epsilon_{\mathbf{k}_2})}{\omega_1 + E_{\mathbf{k}} + E_G + \epsilon_{\mathbf{k}_3} - \epsilon_{\mathbf{k}_2} - i0^+} \; . \tag{4.1}$$

Then, performing the last frequency integral, for the contribution of the whole diagram we obtain:

$$\Pi_{\text{self}}(\Omega) = \frac{2\gamma_0 V_0^2}{(2\pi)^6} \int\int\int d\mathbf{k}_1 \; d\mathbf{k}_2 \; d\mathbf{k}_3 \frac{(1 - n_F(\epsilon_{\mathbf{k}_1})) \cdot (1 - n_F(\epsilon_{\mathbf{k}_3}))}{(\Omega + i0^+ - \Omega_I - (\epsilon_{\mathbf{k}_1} - \mu) - E_{\mathbf{k}_1})^2} \tag{4.2}$$

$$\cdot \frac{n_F(\epsilon_{\mathbf{k}_2})}{(\Omega + i0^+ - \Omega_I - (\epsilon_{\mathbf{k}_1} - \mu) - (\epsilon_{\mathbf{k}_3} - \mu) + (\epsilon_{\mathbf{k}_2} - \mu) - E_{\mathbf{k}})} \; .$$

We now introduce the notation:

$$B^+(\mathbf{k}_i) = \frac{1}{\epsilon + i0^+ - (\epsilon_{\mathbf{k}_i} - \mu) - E_{\mathbf{k}_i}} \; , \qquad \epsilon = \Omega - \Omega_I \ll \beta\mu \; . \tag{4.3}$$

Then we can combine the two relevant diagrams as follows:

$$\Pi(\epsilon) = \frac{\gamma_0 V_0^2}{(2\pi)^6} \int\int\int d\mathbf{k}_1 \; d\mathbf{k}_2 \; d\mathbf{k}_3 \; \left[2B^+(\mathbf{k}_1)^2 - B^+(\mathbf{k}_1)B^+(\mathbf{k}_3)\right] \tag{4.4}$$

$$\cdot \frac{(1 - n_F(\epsilon_{\mathbf{k}_1})) \cdot (1 - n_F(\epsilon_{\mathbf{k}_3})) \cdot n_F(\epsilon_{\mathbf{k}_2})}{(\epsilon + i0^+ - (\epsilon_{\mathbf{k}_1} - \mu) - (\epsilon_{\mathbf{k}_3} - \mu) + (\epsilon_{\mathbf{k}_2} - \mu) - E_{\mathbf{k}})} \; . \tag{4.5}$$

We want to calculate the leading behaviour in ϵ of $A_I(\epsilon) = -\Im[\Pi](\epsilon)$. In our energy regime of interest the only contribution will come from the product of the real parts of the factors in (4.4) and of the imaginary part of (4.5). This can be seen as follows:

$$\Im\left[B^+(\mathbf{k}_i)\,(1 - n_F(\epsilon_{\mathbf{k}_i}))\right] = -i\pi\delta\left(\epsilon - (\epsilon_{\mathbf{k}_1} - \mu) - E_{\mathbf{k}_i}\right)\theta(\epsilon_{\mathbf{k}_i} - \mu) \tag{4.6}$$

Due to the θ-function, $(\epsilon_{\mathbf{k}_i} - \mu) > 0$ and $E_{\mathbf{k}_i} > \beta\mu$, hence the δ-function will necessarily vanish for $\epsilon < \beta\mu$. Only the imaginary part of (4.5) describes a Fermi-sea shake-up and contributes to the absorption at the indirect threshold.

With this consideration, and using the notation:

$$B(\mathbf{k}_i) = \frac{1}{\epsilon - (\epsilon_{\mathbf{k}_i} - \mu) - E_{\mathbf{k}_i}} \ , \tag{4.7}$$

we obtain:

$$A_I(\epsilon) = \mathcal{P}\ \frac{\pi\gamma_0 V_0^2}{(2\pi)^6} \int d\mathbf{k}_1 \int d\mathbf{k}_2 \int d\mathbf{k}_3 \left[2B(\mathbf{k}_1)^2 - B(\mathbf{k}_1)B(\mathbf{k}_3)\right] \cdot \tag{4.8}$$

$$\theta(\epsilon_{\mathbf{k}_1} - \mu)\theta(\epsilon_{\mathbf{k}_3} - \mu)\theta(\mu - \epsilon_{\mathbf{k}_2}) \cdot \delta\left(\epsilon - (\epsilon_{\mathbf{k}_1} - \mu) - (\epsilon_{\mathbf{k}_3} - \mu) + (\epsilon_{\mathbf{k}_2} - \mu) - E_{\mathbf{k}}\right) \ . \tag{4.9}$$

Since all summands in the delta-function are negative, $A_I(\epsilon)$ vanishes at $\epsilon = 0$, as expected.

The principal value $\mathcal{P}$ in (4.8) can actually be dropped since the factors do not have poles. Furthermore, the δ-function in (4.9) shows that $k_i \simeq k_F,\ i = 1, 2, 3$. Therefore, in leading order in ϵ, we can write:

$$B(\mathbf{k}_i) \simeq \frac{1}{-\beta\mu} \ . \tag{4.10}$$

This leads to:

$$A_I(\epsilon) \simeq \frac{\pi\gamma_0 V_0^2}{(2\pi)^6(\beta\mu)^2} \int d\mathbf{k}_1 \int d\mathbf{k}_2 \int d\mathbf{k}_3 \tag{4.11}$$

$$\theta(\epsilon_{\mathbf{k}_1} - \mu)\theta(\epsilon_{\mathbf{k}_3} - \mu)\theta(\mu - \epsilon_{\mathbf{k}_2}) \cdot \delta\left(\epsilon - (\epsilon_{\mathbf{k}_1} - \mu) - (\epsilon_{\mathbf{k}_3} - \mu) + (\epsilon_{\mathbf{k}_2} - \mu) - E_{\mathbf{k}}\right) \ .$$

We substitute

$$\mathbf{x} = \frac{\mathbf{k}_1}{\sqrt{2m}} \ , \qquad \mathbf{y} = \frac{\mathbf{k}_3}{\sqrt{2m}} \ , \qquad \mathbf{z} = \frac{\mathbf{k}_2}{\sqrt{2m}} \ . \tag{4.12}$$

This results in:

$$A_I(\epsilon) = \frac{\rho^3}{\pi^2} \frac{\gamma_0 V_0^2}{(\beta\mu)^2} \int_{x^2>\mu} d\mathbf{x} \int_{y^2>\mu} d\mathbf{y} \int_{z^2<\mu} d\mathbf{z} \tag{4.13}$$

$$\delta\left(\epsilon - \left(x^2 - \mu\right) - \left(y^2 - \mu\right) + \left(z^2 - \mu\right) - \beta\left(\mathbf{x} + \mathbf{y} - \mathbf{z}\right)^2\right) \ .$$

In the δ-function in (4.11) all summands are negative and cannot cancel each other. Thus, each summand must be individually smaller than ϵ, which simplifies the calculation: We can evaluate the integral step by step, keeping all but one summands fixed to values of $\mathcal{O}(\epsilon)$. With this kind of approach we will not be able to correctly account for the numerical prefactor of $A_I(\epsilon)$, which is only of minor importance.

We shortly sketch the main points of the calculation, which is performed in detail in appendix B : In the argument of the delta function of (4.13) we have the summands $(x^2 - \mu), (y^2 - \mu), (z^2 - \mu)$. All of these contribute a factor of ϵ to A_I. One factor is fixed by the δ-function, s.t. we obtain ϵ^2. In addition, we have the term $\beta\left(\mathbf{x} + \mathbf{y} - \mathbf{z}\right)^2$.

For this to be of order ϵ, the angles $\phi = \measuredangle(\mathbf{x}+\mathbf{y}, \mathbf{z})$ and $\theta = \measuredangle(\mathbf{x}, \mathbf{y})$ have to be fixed as depicted in Fig. 4.2.

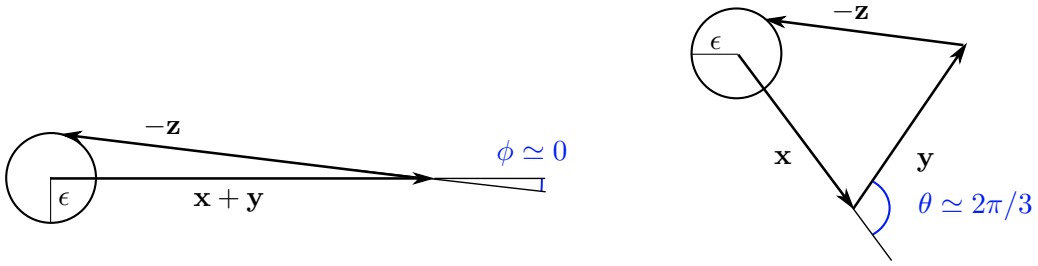

Figure 4.2.: Angles contributing to the indirect threshold. The ϵ-circles indicate smallness in ϵ, but not the exact power law or prefactor.

It is shown in appendix B that in 2D each angle-restriction gives an additional factor of $\sqrt{\epsilon}$, s.t. in total we obtain $A_I \sim \epsilon^3$. The calculation also gives the 3D result, which is found to be $A_I \sim \epsilon^{7/2}$. Restoring the correct non-numerical prefactors as obtained in appendix B, the results read:

$$A_I(\epsilon) \sim \gamma_0 \rho g^2 \left(\frac{\epsilon}{\beta\mu}\right)^3 \cdot \theta(\epsilon) \qquad \text{in} \quad 2D \tag{4.14}$$

$$A_I(\epsilon) \sim \gamma_0 \rho g^2 \left(\frac{\epsilon}{\beta\mu}\right)^{7/2} \cdot \theta(\epsilon) \qquad \text{in} \quad 3D\ , \tag{4.15}$$

which conicides with the findings in Ref. [42], c.f. formulas (7a), (7b) .

It should be noted that this behaviour is not restricted to the perturbative regime; however, in the non-perturbative regime the range of applicability for these power laws will be very small, since higher order diagrams can no longer be disregarded.

4.1.2. Calculation of the dressed bubble

Having obtained the absorption at Ω_I, let us calculate the dressed bubble shown in Fig 4.3, again specializing to 2D.

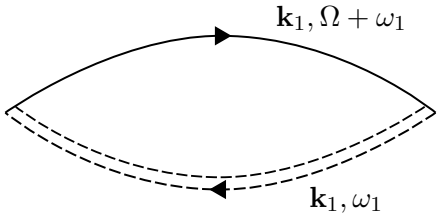

Figure 4.3.: The CB-VB bubble, where the VB Green's function is dressed with the self-energy $\Sigma(\mathbf{k}_1, \omega_1)$ shown in Fig. 4.1.

Close to Ω_I, this diagram reduces to the diagram of Fig. 4.1. Since we have seen in (4.8) - (4.11) that the absorption is given by 1/2 times the contribution of the diagram 4.1, a detailed evaluation of the dressed bubble in principle also gives the prefactor for the absorption; however, since the prefactor is not of interest to us, we will not further pursue this point.

Close to Ω_D, the absorption in the perturbative regime is solely determined by the dressed bubble.

Let us start the evaluation. The contribution of the dressed bubble reads:

$$\Pi_{\mathrm{db}}(\Omega) = \tag{4.16}$$
$$\frac{-i\gamma_0}{(2\pi)^3}\int d\omega_1\; d\mathbf{k}_1 \frac{1}{\Omega+\omega_1-\epsilon_{\mathbf{k}_1}+i0^+\mathrm{sign}(\epsilon_{\mathbf{k}_1}-\mu)}\cdot\frac{1}{\omega_1+E_{\mathbf{k}_1}+E_G-i\Im\left[\Sigma\right](\mathbf{k}_1,\omega_1)} \quad ,$$

where we have disregarded $\Re[\Sigma](k_1,\epsilon)$ as was discussed on page 57. Closing the contour gives, in terms of detuning:

$$\Pi_{\mathrm{db}}(\epsilon) = \frac{\gamma_0}{(2\pi)^2}\int d\mathbf{k}_1 \frac{1-n_F(\epsilon_{\mathbf{k}_1})}{\epsilon-(\epsilon_{\mathbf{k}_1}-\mu)-E_{\mathbf{k}_1}+i\Im\left[\Sigma\right](\mathbf{k}_1,-\epsilon-\Omega_I+\epsilon_{\mathbf{k}_1})} \; . \tag{4.17}$$

Thus, we only need to calculate :

$$\Sigma(\mathbf{k}_1,\tilde{\omega}_1) \qquad \text{with} \qquad \tilde{\omega}_1 = -\epsilon-\Omega_I+\epsilon_{\mathbf{k}_1} \; . \tag{4.18}$$

Inserting this into (4.1), and substituting momenta $\mathbf{k}_3=\mathbf{k}_2+\mathbf{q}$, we obtain:

$$\Im[\Sigma](\mathbf{k}_1,\tilde{\omega}_1] = \frac{2V_0^2}{(2\pi)^4}\int d\mathbf{q}\int d\mathbf{k}_2\; n_F(\epsilon_{\mathbf{k}_2})\cdot(1-n_F(\epsilon_{\mathbf{k}_2+\mathbf{q}}))\cdot \tag{4.19}$$
$$\delta(\epsilon-E_{\mathbf{k}_1+\mathbf{q}}-(\epsilon_{\mathbf{k}_1}-\mu)-\epsilon_{\mathbf{k}_2+\mathbf{q}}+\epsilon_{\mathbf{k}_2}) \; .$$

We can now proceed in analogy to the Lindhard-type evaluation of (2.121) ff. The only difference is that now the energy-argument of the Lindhard-function reads $\epsilon-E_{\mathbf{k}_1+\mathbf{q}}-(\epsilon_{\mathbf{k}_1}-\mu)$. Using $k_1>k_F$ as seen from (4.17), and for $\epsilon<\beta\mu$, we obtain:

$$\Im[\Sigma](\mathbf{k}_1,\tilde{\omega}_1) \simeq \theta(\alpha)\cdot\frac{1}{\sqrt{3}}g^2\beta\mu\frac{\alpha^2}{(\beta\mu)^2} \; , \qquad \alpha=\epsilon-(\epsilon_{\mathbf{k}_1}-\mu) \; , \tag{4.20}$$

which holds exactly in the limit $\epsilon\to 0$, and has the correct order of magnitude for $\epsilon\lesssim\beta\mu$. Having obtained the self-energy, we can evaluate (4.17), starting from the real part. It reads:

$$\Re\left[\Pi_{\mathrm{db}}\right](\epsilon) = \frac{\gamma_0}{(2\pi)^2}\int_{k_1>k_F} d\mathbf{k}_1 \frac{\epsilon-(\epsilon_{\mathbf{k}_1}-\mu)-E_{\mathbf{k}_1}}{(\epsilon-(\epsilon_{\mathbf{k}_1}-\mu)-E_{\mathbf{k}_1})^2+\left(\Im\left[\Sigma\right](\mathbf{k}_1,\tilde{\omega}_1)\right)^2} \; . \tag{4.21}$$

This integral will be dominated by momenta close to k_F for $0<\epsilon<\beta\mu$. This allows us to replace k_1 by k_F in the term $\Im\left[\Sigma\right](\mathbf{k}_1,\tilde{\omega}_1)$. In this way we obtain:

$$\Re\left[\Pi_{\mathrm{db}}\right](\epsilon) \simeq \frac{\rho\gamma_0}{2}\log\left(\frac{(\epsilon-\beta\mu)^2+\left(\frac{1}{\sqrt{3}}g^2\beta\mu\frac{\epsilon^2}{(\beta\mu)^2}\right)^2}{\xi^2}\right) \; . \tag{4.22}$$

We can further simplify this expression substituting $\epsilon=\beta\mu$ in the g^2-term. This will be inaccurate near $\epsilon=0$, but there the summand $(\epsilon-\beta\mu)^2$ is much larger than the g^2-term anyway. Therefore, we arrive at:

$$\Re\left[\Pi_{\mathrm{db}}\right](\epsilon) \simeq \frac{\rho\gamma_0}{2}\log\left(\frac{(\epsilon-\beta\mu)^2+\left(\frac{1}{\sqrt{3}}g^2\beta\mu\right)^2}{\xi^2}\right) \; . \tag{4.23}$$

It should be noted that with logarithmic accuracy this is exactly the logarithm cut by $g^2\beta\mu$ we have used in the previous chapter. (4.23) will serve as the real part of the photon self-energy in the perturbative regime.

Let us continue with the imaginary part of (4.17): Again simplifying $\Im[\Sigma](\mathbf{k}_1, \tilde{\omega}_1)$ in the denominator, and switching to an energy-integration, we obtain:

$$\Im[\Pi_{\mathrm{db}}](\epsilon) = -\frac{\gamma_0 \rho g^2}{\sqrt{3}\beta\mu} \int_0^\epsilon dx \; \frac{(\epsilon - x)^2}{(\epsilon - x(1+\beta) - \beta\mu)^2 + (\frac{g^2}{\sqrt{3}\beta\mu} \cdot \epsilon^2)^2} \; , \tag{4.24}$$

$$x = \epsilon_{\mathbf{k}_1} - \mu \; .$$

For $\epsilon \ll \beta\mu$ we can approximate the denominator of (4.24) by $(\beta\mu)^2$, which leads to:

$$\Im[\Pi_{\mathrm{db}}](\epsilon) \simeq -\frac{\gamma_0 \rho g^2}{3\sqrt{3}(\beta\mu)^3} \cdot \epsilon^3 \cdot \theta(\epsilon) \; , \qquad \epsilon \ll \beta\mu \; . \tag{4.25}$$

As discussed in the beginning of this section, $-\Im[\Pi_{\mathrm{db}}]$ coincides with the absorption close to $\epsilon = 0$ except for numerical prefactors (c.f. (4.14)).

For $\epsilon \lesssim \beta\mu$, integrating (4.24) and keeping only the leading terms in g and β results in:

$$\Im[\Pi_{\mathrm{db}}](\epsilon) \simeq -\frac{\gamma_0 \rho (\beta\mu)^2}{\epsilon^2} \arctan\left(\frac{g^2}{\sqrt{3}\beta\mu} \cdot \frac{\epsilon^2}{\beta\mu - \epsilon}\right) \; , \qquad \epsilon \lesssim \beta\mu \; . \tag{4.26}$$

We now combine both limits into a form that has the correct power law for $\epsilon \ll \beta\mu$ and is of the correct order for $\epsilon \lesssim \beta\mu$. Introducing the dimensionless variable

$$y = \frac{\epsilon}{\beta\mu} \; , \tag{4.27}$$

we arrive at:

$$\Im[\Pi_{\mathrm{db}}](y) \simeq -\gamma_0 \rho \cdot y \cdot \arctan\left(\frac{g^2}{\sqrt{3}} \cdot \frac{y^2}{1-y}\right) \cdot \theta(y) \; , \qquad 0 < y < 1 \; . \tag{4.28}$$

To approximately find the behaviour for $y > 1$, we can invoke the following arguments: To begin with, for $\epsilon \gg E_R \simeq \beta\mu$, we should recover the infinite mass behaviour, which is simply $-\gamma_0\rho\pi$, as found in (3.10) (Note that the absorption is given by $-\Im[\Pi]$). We also disregard the cutoff at scales $\epsilon > \xi$. Furthermore, in the limit $g \to 0$, $\Im[\Pi_{\mathrm{db}}](y)$ should approximate $-\gamma_0\rho\pi \cdot \theta(y-1)$. The simplest way to take these points into account, is just to attach a "mirrored" form of (4.28) at $y = 1$, which also gives a smooth extension. For now, this will be sufficient for us. As a result, we obtain:

$$\Im[\Pi_{\mathrm{db}}(y)] \simeq -\gamma_0 \rho \cdot f(y) \tag{4.29}$$

$$f(y) = \theta(2-y) \cdot [g(y) + \theta(y-1) \cdot (-g(2-y) + \pi)] + \pi \cdot \theta(y-2) \tag{4.30}$$

$$g(y) = y \cdot \arctan\left(\frac{g^2}{\sqrt{3}} \cdot \frac{y^2}{1-y}\right) \cdot \theta(y) \; . \tag{4.31}$$

The perturbative absorption $A_p(y)$ resulting from (4.29) is then approximately correct in the whole spectral range, except for the prefactor at small y. A plot for two values of g is shown in Fig. 4.4.

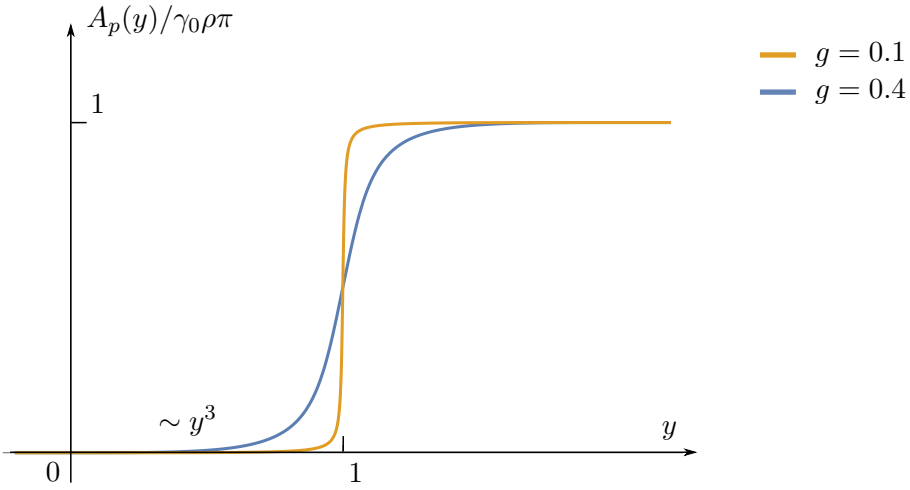

Figure 4.4.: Absorption in the perturbative regime for two values of g. The large value of $g = 0.4$, beyond the perturbative regime, is shown for illustrative purposes. This result was obtained by computing the contribution of the diagram of Fig. 4.3 only.

Essentially we have recovered the smeared θ-function we had found with the Mahan approach (c.f. Fig. 3.11); in addition, we have obtained the correct behaviour near Ω_I.

4.2. Non-perturbative regime

4.2.1. Nozières infinite mass treatement

Let us now consider the controlled non-perturbative regime, i.e $g \simeq g_1(\beta)$ and $g \gg g_2(\beta)$. We want to reproduce the findings of section 3.3.4, but without "guessing" as in the Mahan-approach. This can be achieved by solving a Bethe-Salpeter equation for the vertex.

To begin with, we will very shortly sketch the main points of the infinite mass treatment that will be necessary for us, as found in Refs. [7], [8]. A summary is furthermore presented in Ref. [28], section 26 VII.

The main idea of the Nozières approach is again to sum the leading logarithmic diagrams contributing as $(gL)^n \cdot L$, as discussed on page 63. There are several simplifications for infinite hole mass. First of all, only the CB Green's functions are momentum dependent. One can integrate these over the internal momenta, which leads to effective CB Green's functions which only depend on frequency, as well as all other objects. This again shows that the infinite mass problem is effectively one-dimensional. Futhermore, as discussed on page 64, the self-energy diagrams can be disregarded. Thus, one needs to find the full frequency-dependent vertex function γ, shown in Fig. 4.5.

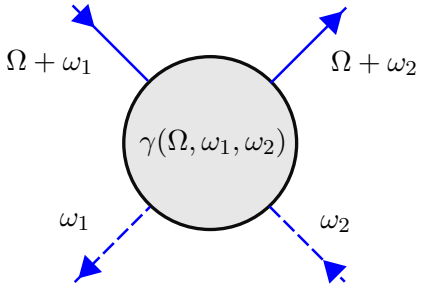

Figure 4.5.: Full frequency-dependent vertex function. Full lines represent effective CB propagators, dashed lines VB propagators. Amputated propagators are shown in blue.

Inserting γ, the diagrams representing the photon self-energy $\Pi(\Omega)$ are those shown in Fig. 4.6.

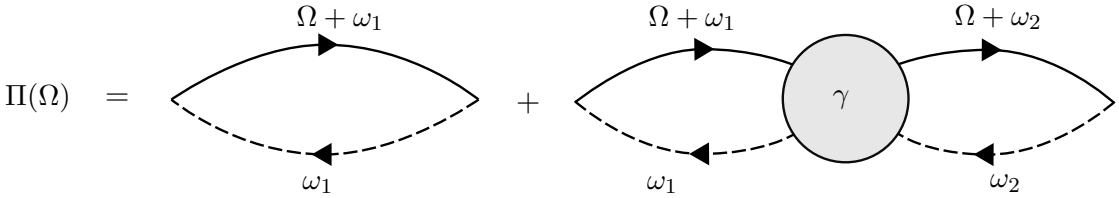

Figure 4.6.: The photon self-energy $\Pi(\Omega)$ in terms of the full vertex γ.

The basic ingredients for γ are the ladder and crossed diagrams. The ladder diagrams are formed by bubbles of antiparallel lines; In accordance with Ref. [7] we will call this channel 2. By contrast, the crossed diagrams comprise parallel bubbles. This is easiest seen twisting the interaction lines of the standard second order crossed diagram, which results in Fig. 4.7.

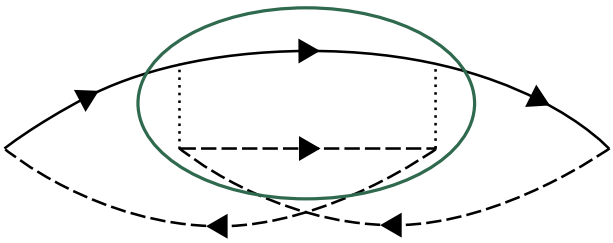

Figure 4.7.: Twisted version of the crossed diagram that contains a bubble with parallel lines, marked by the green ellipsis.

Bubbles with parallel lines will be called channel 1.
The key concept of the treatment by Nozières is the reducibility: A diagram is called reducible in channel 1(2), if it splits into two parts upon cutting two parallel (antiparallel) VB-CB-lines. The set of all reducible vertex diagrams of channel i will be called γ_i, while the irreducible diagrams will be called I_i. The first obvious equation resulting from these definitions is

$$\gamma = \gamma_1 + I_1 = \gamma_2 + I_2 \ , \tag{4.32}$$

since every diagram is either reducible or irreducible.

One can write down two coupled Bethe-Salpeter equations for the reducible vertices γ_i. We will content ourselves with the diagrammatic representation, shown in Fig. 4.8 for channel 2:

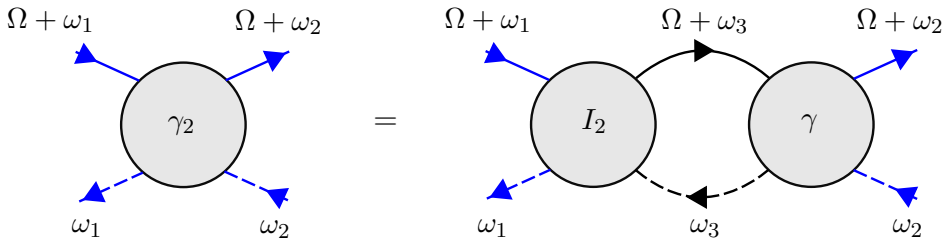

Figure 4.8.: Bethe-Salpeter equation for channel 2.

The equation for channel 1 looks analogous, only with parallel lines in the intermediate bubble of the right hand side.

It is important to notice that there is no diagram simultaneously reducible in channel 1 and 2:

$$\gamma_1 \cap \gamma_2 = \emptyset \ . \tag{4.33}$$

Essentially every such diagram would violate particle conservation. Introducing the totally irreducible interaction $R = I_1 \cap I_2$, we have the following vertex relations:

$$\begin{aligned} I_1 &= R + \gamma_2 \\ I_2 &= R + \gamma_1 \\ \gamma &= R + \gamma_1 + \gamma_2 \ , \end{aligned} \tag{4.34}$$

where (4.33) is necessary to avoid double counting of diagrams.

Together with the two Bethe-Salpeter equations, one of which was represented in Fig. 4.8, (4.34) form the so-called *parquet equations*. An approximate solution for these can be found relying on the leading logarithmic approximation. The latter allows to simplify the irreducible interaction R to the bare vertex:

$$R \simeq V_0. \tag{4.35}$$

The reason for this enormous simplfication is that higher order vertex diagrams which are totally irreducible only contribute subleading logarithms and therefore can be disregarded. The lowest order diagram which is ruled out in this manner is shown in Fig. 4.9.

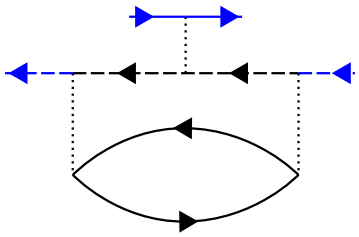

Figure 4.9.: Third order irreducible vertex diagram, contributing as $V_0 g^2 L$, which is subleading.

Within the approximation (4.35) all graphs are summed, where a single vertex is replaced by parallel or antiparallel bubbles any number of times. These diagrams are called *parquet graphs*.

Essentially, these approximations are sufficient to solve the parquet-equations, which however still is a highly non-trivial task. For the purpose of illustration we will present an exemplary solution of a finite-mass Bethe-Salpeter equation in Appendix C. For the moment, let us just quote an intermediate result of Ref. [7] which is of relevance for us: It is found that the reducible vertex γ_1 involved in the calculation of $\Pi(\Omega)$ is just given by the single parallel bubble marked in Fig. 4.7. This means that in all diagrams contributing to $\Pi(\Omega)$ no more than two interaction lines cross. All other diagrams cancel each other. In third order, this statement can already be found in Mahan's original paper [6]: He showed that the sum of the leading logarithms of the diagrams presented in Fig. 4.10 vanishes.

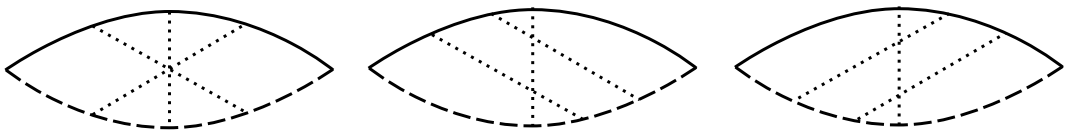

Figure 4.10.: Third order diagrams where more than two interaction lines cross, canceling each other.

The reducible vertex γ_2, however, has a complicated non-perturbative form. With these vertices found, $\Pi(\Omega)$ can then be calculated, reproducing Mahan's infinite mass result (3.40).

4.2.2. Finite mass treatement

Let us now advance to the finite mass calculation, carrying over the calculations of Ref. [27] to 2D. As in the infinite mass case, we have to find the vertex function, but now with VB propagators dressed by the self-energy of (4.1). Since now the momentum dependence will be nontrivial again, from the momentum-integrated CB propagators of the last section we switch to normal ones. It will furthermore be convenient to use a different type of vertex function with only two legs, which we will call $\Lambda(\mathbf{k}, \Omega, \omega_1)$. In terms of Λ, $\Pi(\Omega)$ is shown in Fig. (4.11).

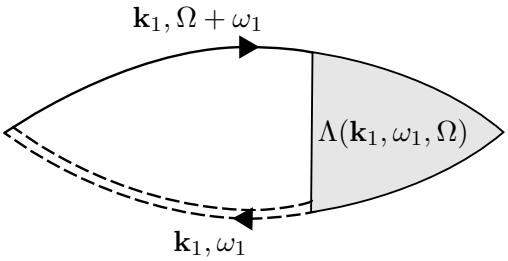

Figure 4.11.: $\Pi(\Omega)$ in terms of the full two-legged vertex Λ. The double dashed line respresents the dressed VB propagator.

The corresponding formula reads

$$\Pi(\Omega) = -\frac{i\gamma_0}{(2\pi)^3} \int d\omega_1 \; d\mathbf{k}_1 \; \Lambda(\mathbf{k}_1, \Omega, \omega_1) \; G_c(\mathbf{k}_1, \Omega + \omega_1) \; G_v(\mathbf{k}_1, \omega_1) \; . \tag{4.36}$$

From the fact that $\Pi(\Omega)$ is retarted we can conclude that also Λ is retarded in both frequency variables. Thus, we can carry out the ω_1-integral, which results in:

$$\Pi(\Omega) = -\frac{\gamma_0}{(2\pi)^2} \int_{k_1 > k_F} d\mathbf{k}_1 \; \Lambda(\mathbf{k}_1, \Omega, \tilde{\omega}_1) \; G_v(\mathbf{k}_1, \tilde{\omega}_1) \tag{4.37}$$

$$\tilde{\omega}_1 = -\Omega + \epsilon_{\mathbf{k}_1} \; , \tag{4.38}$$

which shows that it is sufficient to find $\Lambda(\mathbf{k}_1, \Omega, \tilde{\omega}_1)$. To this aim, we write down a Bethe-Salpeter-equation for Λ, phrasing everything in terms of channel 2 as defined in the previous section. Diagrammatically, it is shown in Fig. 4.12.

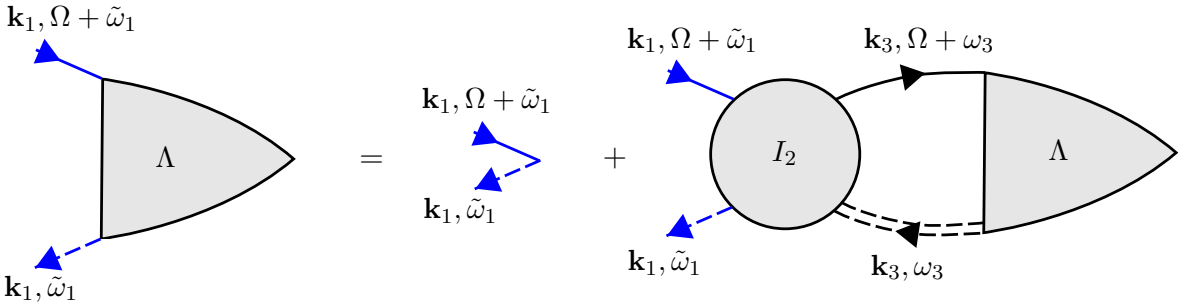

Figure 4.12.: Bethe-Salpeter equation for the two-legged vertex Λ. We have written ω_3 rather than ω_2 to match earlier notations.

We aim to solve this equation with logarithmic accuracy. Expressing it mathematically, we obtain:

$$\Lambda(\mathbf{k}_1, \Omega, \tilde{\omega}_1) = 1 + \frac{i}{(2\pi)^3} \int d\mathbf{k}_3 \int d\omega_3 \; I_2(\mathbf{k}_1, \mathbf{k}_3, \Omega, \tilde{\omega}_1, \omega_3) \cdot \tag{4.39}$$
$$G_c(\mathbf{k}_3, \Omega + \omega_3) \; G_v(\mathbf{k}_3, \omega_3) \; \Lambda(\mathbf{k}_3, \Omega, \omega_3) \; .$$

With the same argument as above, we can take the ω_3-integral, which yields:

$$\Lambda(\mathbf{k}_1, \Omega, \tilde{\omega}_1) = 1 + \frac{1}{(2\pi)^2} \int_{k_3 > k_F} d\mathbf{k}_3 \; I_2(\mathbf{k}_1, \mathbf{k}_3, \Omega, \tilde{\omega}_1, \tilde{\omega}_3) \; G_v(\mathbf{k}_3, \tilde{\omega}_3) \; \Lambda(\mathbf{k}_3, \Omega, \tilde{\omega}_3) =$$
$$1 + \frac{1}{(2\pi)^2} \int_{k_3 > k_F} k_3 \; dk_3 \; G_v(k_3, \tilde{\omega}_3) \; \Lambda(k_3, \Omega, \tilde{\omega}_3) \int_0^{2\pi} d\theta \; I_2(k_1, k_3, \theta, \Omega, \tilde{\omega}_1, \tilde{\omega}_3) \tag{4.40}$$

$$\tilde{\omega}_3 = -\Omega + \epsilon_{\mathbf{k}_3} \; , \qquad \theta = \measuredangle(\mathbf{k}_1, \mathbf{k}_3) \; . \tag{4.41}$$

We now use the relation $I_2 = R + \gamma_1$ from (4.34) in combination with the simple results of the infinite mass treatement for R and γ_1. In our current regime where $gL \simeq 1$, we can assume that these results are still valid. Therefore, we have

$$I_2 \simeq V_0 + \gamma_1^0 \; , \tag{4.42}$$

where γ_1^0 is the diagram redrawn in Fig. 4.13.

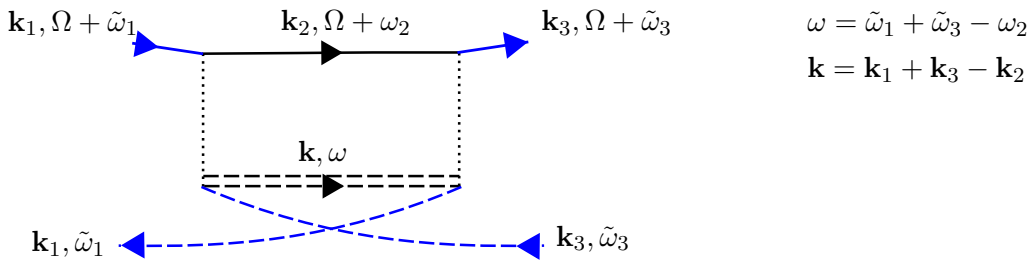

Figure 4.13.: Channel 1 reducible vertex γ_1^0.

The diagram γ_1^0 is just a part of the second order crossed diagram, and we have already calculated it, c.f. Appendix A, using a constant self-energy. This remains correct with logarithmic accuracy. The angular integral over γ_1^0 appearing in (4.40) was evaluated as well, with the result (A.14) up to prefactors $V_0, 2\pi$. Introducing the notation:

$$x_i = \Omega_D - \Omega + \frac{k_i^2}{2m} - \mu \ , \qquad i = 1, 2 \ , \tag{4.43}$$

and restoring the correct prefactors, we can then rewrite (4.40) as:

$$\Lambda(x_1, \Omega) = 1 + \int_{\Omega_D - \Omega}^{\xi} dx_3 \ I_2(x_1, x_3, \Omega) \ G_v(x_3, \Omega) \ \Lambda(x_3, \Omega) \tag{4.44}$$

$$G_v(x_3, \Omega) = \frac{1}{(1+\beta)x_3 + \beta(\Omega - \Omega_D) - \Sigma(x_3, \Omega)} \tag{4.45}$$

$$I_2(x_1, x_3, \Omega) = g + g^2 \log\left(\max\left\{\frac{|x_1 + x_3 + \Omega - \Omega_D|}{\xi}, \beta\right\}\right) \ , \tag{4.46}$$

where we have also modified (A.14) with logarithmic accuracy. Again with logarithmic accuracy, eq. (4.44) - (4.46) coincide with the intermediate results given in Ref. [27], c.f. (22)f., s.t. we can continue in line with their further calculations. The only dimensional dependence is contained in the parameter g, exactly as discussed for the Mahan approach on page 73.

To have a complete description, let us sketch the remaining steps of the calculation. To begin with, the self-energy appearing in (4.45) is inserted from (4.20):

$$\Sigma(x_3, \Omega) = \Sigma(\mathbf{k}_3, \tilde{\omega}_3) \simeq i\Im\left[\Sigma\right](\mathbf{k}_3, \tilde{\omega}_3) \simeq i\theta(\beta\mu - x_3) \cdot \frac{1}{\sqrt{3}} g^2 \frac{(\beta\mu - x_3)^2}{(\beta\mu)} \ . \tag{4.47}$$

From (4.45) it is seen that, accounting for the leading behaviour only, $\Sigma(x_3, \Omega)$ is only relevant for $x_3 < g^2\beta\mu$. Thus, the correct leading behaviour of (4.44) is reproduced by the simplified form:

$$\Lambda(x_1, \Omega) \simeq 1 + \int_{\max\{|\Omega - \Omega_D|, g^2\beta\mu\}}^{\xi} dx_3 \ \frac{1}{x_3} I_2(x_1, x_3, \Omega) \ \Lambda(x_3, \Omega) \ . \tag{4.48}$$

Since I_2 can only grow logarithmically, the lower boundary of (4.48) will show up in the argument of a logarithm. In our energy regime under control where $g \gg g_2(\beta)$, we can

thus replace $g^2\beta\mu$ by $\beta\mu$. Applying the same manipulations on (4.37) results in

$$\Pi(\Omega) = -\gamma_0\rho \int_{\max\{|\Omega-\Omega_D|,\beta\mu\}}^{\xi} dx_1 \; \frac{1}{x_1}\Lambda(x_1,\Omega) \; . \tag{4.49}$$

These equations are solved in Ref. [27]. We will only present the calculation in the simplest case, c.f. Appendix C. As a result, in terms of detuning from the indirect treshold ϵ, one finds:

$$\begin{aligned}\Pi(\epsilon) &\simeq -\frac{\gamma_0\rho}{2g}\left(\exp\left[-2g\log\left(\frac{\max\{|\epsilon-\beta\mu|,\beta\mu\}}{\xi}\right)\right]-1\right) \\ &= -\frac{\gamma_0\rho}{2g}\left(\left(\frac{\xi}{\max\{|\epsilon-\beta\mu|,\beta\mu\}}\right)^{2g}-1\right) \; .\end{aligned} \tag{4.50}$$

Of course, with logarithmic accuracy we have actually only found $\Re[\Pi](\epsilon)$. In principle, we can recover $\Im[\Pi](\epsilon)$, adding the relevant imaginary part to the logarithm appearing in (4.50) with help of Kramers-Kronig relations. Alas, in a strict mathematical sense this procedure is obviously flawed, since the analytical continuation of a locally constant function is a constant. This means that just the logarithmic-accuracy result (4.50) is not sufficient for the determination of $\Im[\Pi](\epsilon)$. We can, however, invoke the following additional arguments:

1. In the infinite mass limit, the full logarithm appearing in the exponent was the contribution of one basic electron-hole bubble. This should be still fulfilled in the non-perturbative finite mass calculation, since the two limits should be continuously connected. The basic self-energy dressed bubble was calculated in section 4.1.2. Comparing with (4.23), we see that with logarithmic accuracy it's real part $\Re[\Pi_{db}]$ conincides with the logarithm of (4.50) in our energy regime of interest except for the prefactor $\rho\gamma_0$. Thus, as relevant imaginary part we should add the expression $\Im[\Pi_{db}]$ respectively $f(y)$ given in (4.29), (4.30).

2. This choice will also lead to the correct power law behaviour of the absorption close to the indirect threshold as found in section 4.1.1.

Proceeding in this manner, and furthermore rewriting $\Re[\Pi]$ as a smooth function, in terms of renormalized detuning $y = \epsilon/\beta\mu$ our final result reads:

$$\Re[\Pi](y) = -\frac{\gamma_0\rho}{2g}\left(\left(\frac{\xi/\beta\mu}{\sqrt{1+(y-1)^2}}\right)^{2g}-1\right) \tag{4.51}$$

$$\Im[\Pi](y) = -\gamma_0\rho\left(\frac{\xi/\beta\mu}{\sqrt{1+(y-1)^2}}\right)^{2g}\cdot f(y) \; , \tag{4.52}$$

where $f(y)$ is given in (4.30). In the limit $\beta \to 0$ these formulas correctly reduce to the infinite mass result (3.20), (3.21).

A plot of the corresponding non-perturbative absorption $A_{np}(y)$ for a small value of β and three different values of g is shown in Fig. 4.14.

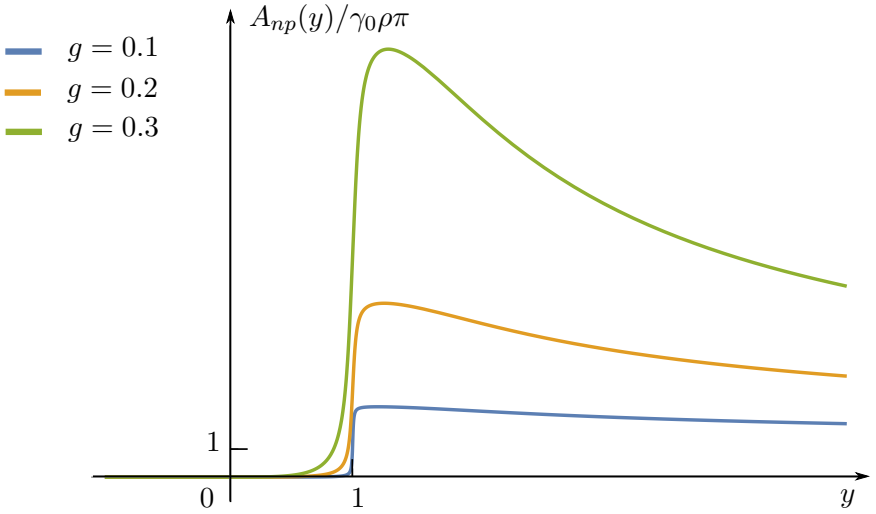

Figure 4.14.: Non-perturbative absorption for different values of g. This result was obtained by solving the Bethe-Salpeter equation of Fig. 4.12 with logarithmic accuracy, using a VB Green's function dressed by the conribution of Fig. 2.15. Used parameters: $\beta = 0.01$, $\xi = \mu$.

It is clearly seen how the absorption develops from a step-like function reminiscent of the perturbative regime for small values of g to a cut-off singularity for larger values of g.

Finally, Fig. 4.15 shows a comparison of two absorption curves for a realistic high-mobility value of $\beta_r \simeq 0.14$. As was discussed on pages 71 f., for such small hole masses the whole spectral range of the non-perturbative regime is only within our reach if we invoke additional arguments beyond our theory.

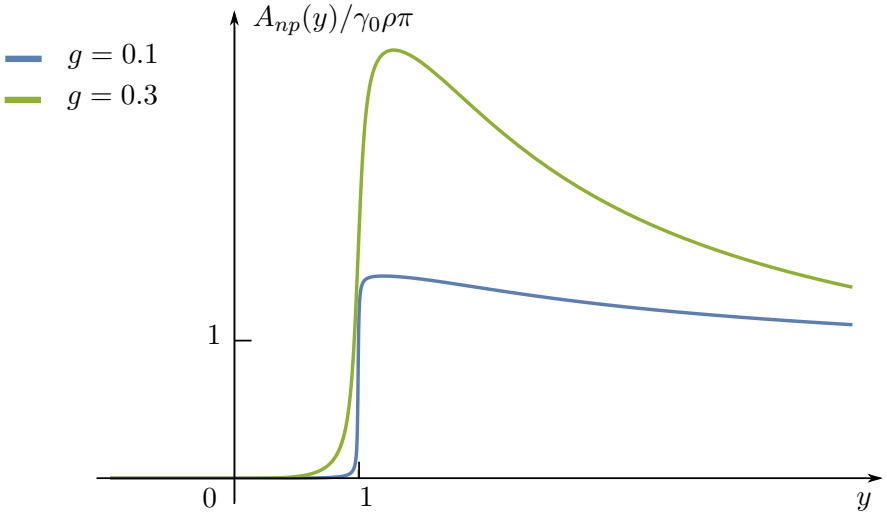

Figure 4.15.: Non-perturbative absorption for two different values of g for a realistic value of $\beta_r = 0.14$ and $\xi = \mu$.

5. Polariton properties

Having obtained the photon self-energy, we can now evaluate polariton properties. To begin with, let us give a short overview over recent theoretical treatments of Fermi-edge polaritons.

First results were obtained by Averkiev and Glazov [49] (2007), who treated polaritons semiclassically, calculating the optical susceptibility of the QW instead of the photon self-energy. The Fermi-edge singularity was taken into account heuristically as enhancement of the optical matrix element near the threshold. They also discussed the case where the absorption becomes non-singular at the theshold, which in principle is similar to our findings for finite hole mass. However, in Ref. [49] no microscopical explanation for this outcome was presented, except for a phenomenological attribution to a dominant Anderson orthogonality exponent (c.f. (3.3)).

Further discussions can be found in two mostly numerical papers by Baeten and Wouters [47] (2013), [50] (2014), who calculated the photon self-energy similar to us. In the first paper, a finite hole mass was considered, in addition to further effects like a more realistic electron-hole interaction. The polariton spectral function was then studied as a function of electron density. However, all calculations were done within the ladder approximation in the whole spectral region, which strongly overestimates excitonic features. As a result, a clear polariton splitting was found for all shown densities, which seems inconsistent with the experimental results of Ref. [1].

In the second paper, an elaborate numerical treatement going back to the method by Combescot and Nozières [40] was employed, again concentrating on the density-dependence of the polariton spectral function, but the hole mass was disregarded alltogether.

5.1. Polariton spectral function: theoretical results

Let us now discuss the spectral function of Fermi-edge polaritons. We start with zero momentum polaritons. Most important features can then be extracted from a density plot of the polariton spectral function as function of energy and cavity detuning, which will also be convenient for comparison to the experiment. Similar plots can be found in [49], where they are phrased as cavity transmission coefficients.

5.1.1. Exciton regime

To familiarize ourselves with the physics, let us first regress to excitons, and consider the same simple exciton-polariton model as in section 1.6:

$$G_{\mathrm{ep}}(\epsilon,\delta) = \frac{1}{\epsilon - \delta + i\Gamma_c - \Pi_{\mathrm{ep}}(\epsilon)} \tag{5.1}$$

$$\Pi_{\mathrm{ep}}(\epsilon) = g_{\mathrm{ep}}^2 \cdot \frac{1}{\epsilon + i0^+} \ . \tag{5.2}$$

Here, δ is the detuning of the cavity energy from the exciton pole as defined in (1.68), and ϵ is the energy measured from the exciton pole. Matching a realistic setup, the cavity mode has a linewidth (which we define as 1/2 FWHM) Γ_c e.g. due to cavity loss, while the exciton linewidth is disregarded. g_{ep} is the exciton-photon coupling defined in (1.67).

The resulting spectral function $\mathcal{A}_{\mathrm{ep}}(\epsilon)$ then has the following general form:

$$\mathcal{A}_{\mathrm{ep}}(\epsilon,\delta) = -2\Im\left[G_{\mathrm{ep}}\right](\epsilon,\delta) = \frac{2\left(\Gamma_c - \Im[\Pi_{\mathrm{ep}}](\epsilon)\right)}{\left(\epsilon - \delta - \Re[\Pi_{\mathrm{ep}}(\epsilon)\right)^2 + \left(\Gamma_c - \Im[\Pi_{\mathrm{ep}}](\epsilon)\right)^2} \,. \tag{5.3}$$

A typical density plot of $\mathcal{A}_{\mathrm{ep}}$ is shown in Fig. 5.1.

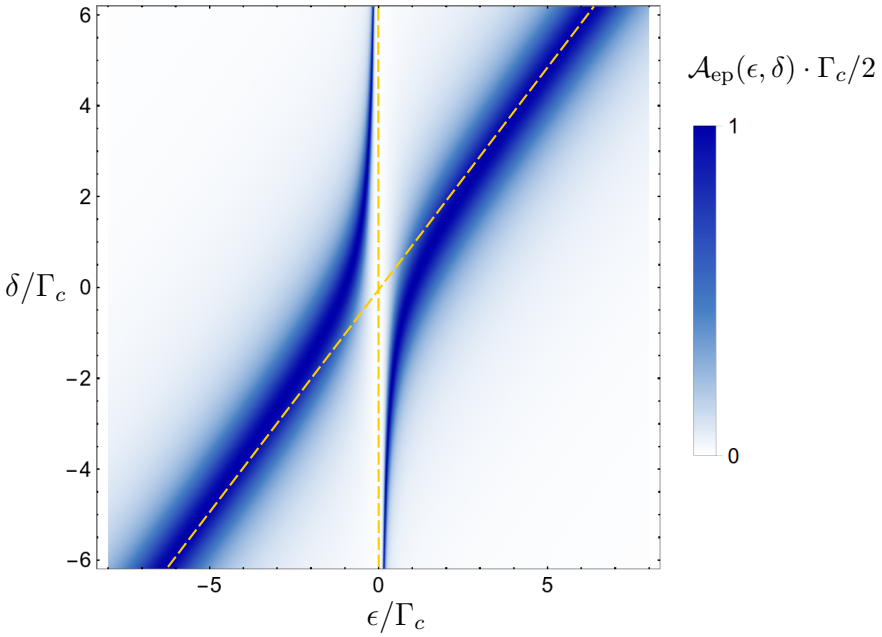

Figure 5.1.: Exciton-Polariton spectral function. The dashed yellow lines show the bare photon and exciton modes, respectively. Used parameter: $g_{\mathrm{ep}} = \Gamma_c$.

In this and forthcoming graphs we choose the parameters approximately as in Ref. [1] if possible, measuring energies in units of Γ_c. For $\Gamma_c = 1$ meV as in Ref. [1], in this way we effectively mimic meV as energy unit.

Fig. 5.1 has a transparent interpretation: The exciton mode (which would correspond to the yellow vertical line at $\epsilon = 0$) and the cavity photon mode (corresponding to the yellow diagonal line) repell each other, resulting in an avoided crossing, and the formation of two polariton modes. In the simplified exciton model, evaluating the maxima of the spectral function, the polariton mode maxima as a function of detuning are found to be (as in (1.65)):

$$\epsilon_{\mathrm{UP/LP}} = \frac{1}{2}(\delta \pm \sqrt{\delta^2 + 4g_{\mathrm{ep}}^2}) \,. \tag{5.4}$$

It is clearly seen that the upper polariton approaches the exciton branch $\epsilon = 0$ at large negative detunings, i.e. is matter-like, and the photon branch $\epsilon = \delta$ at large positive

detunings, i.e. is light-like. For the lower polariton one has the exact opposite behaviour. An evaluation of Hopfield coefficents via spectral integration can be found in Ref. [50].

At zero detuning the polaritons are half-light-half-matter. Their linewidth is found to be $\Gamma_c/2$, i.e. the average of photon and exciton linewidth. The splitting of the polaritons at zero detuning, called *normal mode splitting*, is $2g_{\mathrm{ep}}$. Thus, with the parameters of the plot above we are clearly in the strong coupling regime.

For strong detunings, the linewidth of the photon-like branch approaches Γ_c while the linewidth of the exciton-like branch approaches zero.

It should be noted, that within this simple treatment the lower and upper polariton are perfectly symmetric. In reality this of course is not quite true even in a pure excitonic regime, since the upper polariton can decay in the lower one, thus having a larger linewidth.

5.1.2. Fermi-edge regime

Let us now proceed with the Fermi-edge regime. To begin with, we consider the case of infinite mass. As photon self-energy $\Pi(\epsilon)$ we insert the formulas (3.20), (3.21) into the spectral function (5.3) instead of Π_{ep}. ϵ, δ are now measured from the indirect threshold $E_G + \mu$. We introduce the effective Fermi-edge-photon coupling:

$$g_{\mathrm{fp}} = \gamma_0 \rho \ . \tag{5.5}$$

where γ_0 is the light-matter coupling strength for zero momentum photons as defined in (1.53). g_{fp} and the exciton-photon coupling g_{ep} used in the last section are the prefactors of the photon self-energy in the different regimes. Effectively, they measure the weight of the pole in absorption, and are different due to the different models used in the derivation of the Wannier-exciton and the Fermi-edge singularity (e.g. g_{ep} is proportional to the hydrogenic-type eigenfunction of Wannier excitons). We will fix these couplings in such a way that the normal mode splitting of the polariton branches has the right order of magnitude as compared to the measurements of Ref. [1].

To summarize, our parameters for $\Pi[\epsilon]$ are g_{fp}, ξ and g. For the following plot, we fix these as follows:

1. In our model, $\xi \simeq \mu$. In [1], the low-mobility sample roughly fulfills $\mu \simeq 4$ meV. In energy units of Γ_c (in [1], $\Gamma_c \simeq 1$ meV), we thus use $\xi = 4$.

2. For illustrative purposes we will use the large value $g = 0.5$, which will also simplify evaluations since the Fermi-edge power law reads $-2g$. In addition, this value is approximately correct for the description of [1] where $\mu \simeq E_0$ (c.f (2.17)). We will comment on the g-dependence below.

3. We will fix $g_{\mathrm{fp}} = 1/3$, which will result in a lower polariton branch detuned from the threshold by Γ_c (as in the exciton case), as shown below.

We again want to emphasize that these choices shall only reproduce a realistic order of magnitude, we do not attempt to fit the parameters precisely to [1]. The resulting infinite mass Fermi-edge polariton spectral function $\mathcal{A}_\infty$ is shown in Fig. 5.2.

In this plot, the lower polariton is still seen as a well defined quasi-particle, it looks very similar to the exciton-polariton case: Since the light-matter interaction pulls the polariton below the absorption threshold, no decay into matter excitations is possible.

At $\delta = 0$, the lower polariton peak for $g = 0.5$ is detuned from the threshold to $1/2 \cdot (g_{\mathrm{fp}} - \sqrt{g_{\mathrm{fp}} \cdot (g_{\mathrm{fp}} + 4\xi)})$. We used this fact to fix $g_{\mathrm{fp}} = 1/3$, s.t. the detuning is Γ_c. For larger (smaller) values of g this detuning is larger (smaller). Thus, the red-shift of the lower polariton mode as compared to the photonic mode increases with increasing weight of the Fermi-edge close to the threshold, i.e. when the Fermi-edge is exciton-like, and with larger light-matter interactions. In other words, the larger the weight of the the excitonic pole, the stronger the photon-exciton repulsion.

The linewidth of the lower polariton also roughly behaves as in the exciton case, determined mostly by the photonic content of the lower polariton.

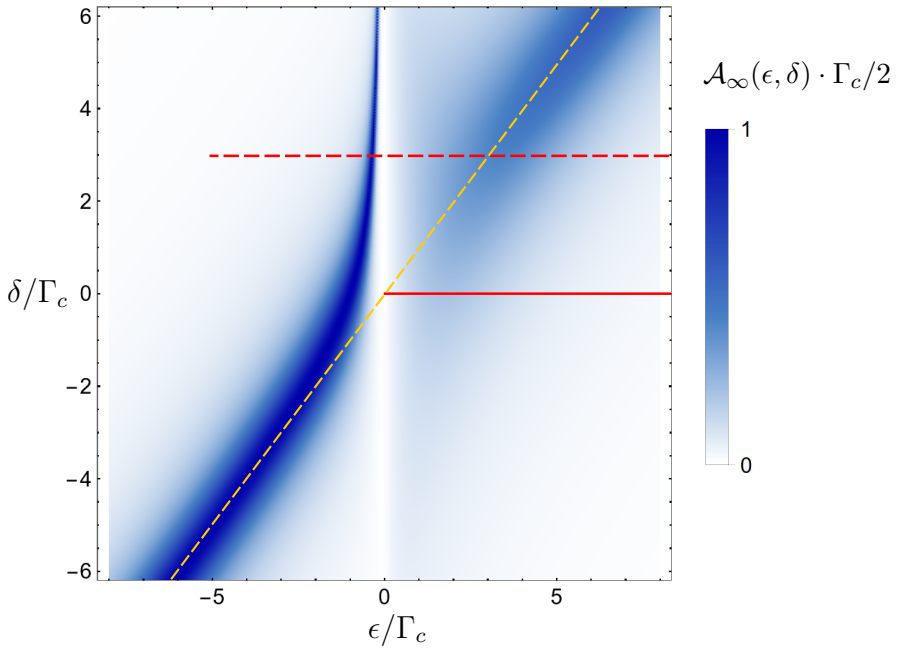

Figure 5.2.: Fermi-edge polariton spectral function for infinite hole mass. This plot was generated by inserting the infinite hole mass photon self-energy of (3.20), (3.21) into the spectral function of (5.3). The full/dashed red lines indicate the spectral ranges shown in detail in Fig. 5.3/Fig 5.5. The dashed yellow line shows the bare photon mode. Used parameters: $g_{\mathrm{fp}} = 0.33\Gamma_c$, $\xi = 4\Gamma_c$, $g = 0.5$.

However, the behaviour of the upper polariton has completely changed in comparison to the exciton case: Since the photon can decay into the incoherent continuum of matter excitations for $\epsilon > 0$, the effective linewidth of the upper polariton is strongly increased.

The spectral weight of the upper polariton is determined by the absorption $\Im[\Pi](\epsilon)$ at the maximum of $\mathcal{A}_\infty(\epsilon, \delta)$ defining the polariton. For negative cavity detunings, $\delta < 0$, the maximum lies at $\epsilon \gtrsim 0$. Since $\Im[\Pi](\epsilon \gtrsim 0)$ is infinite (c.f. (3.21)), the upper polariton never has a significant spectral weight for negative detunings. As δ increases, the polariton pole gets shifted to larger ϵ as well. Due to the power law absorption decay, the polariton spectral weight increases. Finally, at large positive detunings, when the absorption is cut off by finite bandwidth-effects (contained in the decay of $\Im[\Pi](\epsilon)$), the photonic mode with full spectral weight reappears with in the spectrum (as seen in the upper right corner of Fig. 5.2).

For smaller values of g, when changing the detuning δ from negative to positive values, the spectral weight of the polariton increases faster for $\delta < \xi$ (and slower for $\delta > \xi$, but the behaviour beyond the UV cut-off is of course not within our reach).

The infinite mass spectral function $\mathcal{A}_\infty$ contains a clear trace of the Fermi-edge power law, as seen from it's general form (5.3): For any detuning, for $\epsilon \gtrsim 0$ the power laws contained in $\Re[\Pi]$, $\Im[\Pi]$ will dominate, and $\mathcal{A}_\infty$ is found to behave like

$$\mathcal{A}_\infty(\epsilon,\delta) \simeq \underbrace{\frac{2\pi}{g_{\mathrm{fp}}\,(2g^{-2}+\pi^2)}}_{:=\alpha_1} \cdot \left(\frac{\epsilon}{\xi}\right)^{2g}, \qquad \epsilon \ll \xi\cdot(\Gamma_c/g_{\mathrm{fp}})^{-2g},\ \xi\cdot(\delta/g_{\mathrm{fp}})^{-2g}\ . \quad (5.6)$$

This statement is born out in Fig. 5.3 , which shows a double logarithmics plot of (5.6), and $\mathcal{A}_\infty(\epsilon,0)$ along the cut indicated by the full red line in Fig. 5.2.

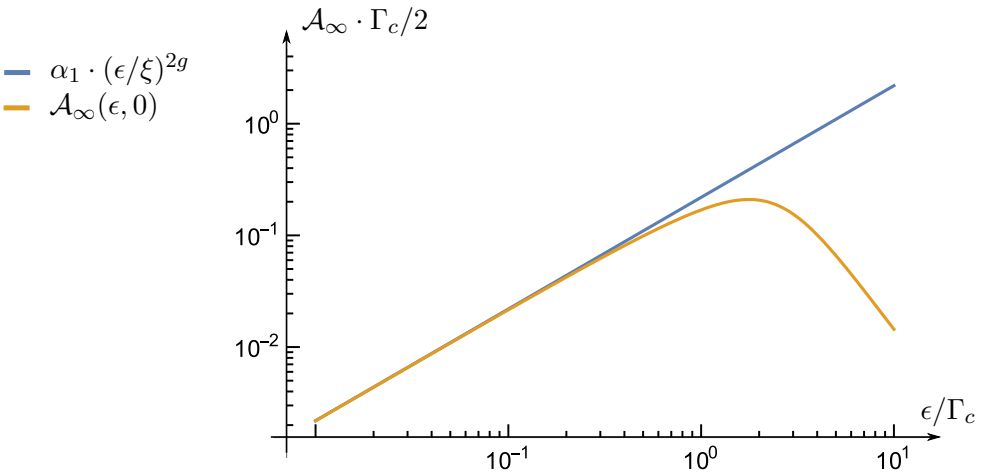

Figure 5.3.: Comparison of the power law formula (5.6), and $\mathcal{A}_\infty(\epsilon,0)$. Parameters as in Fig. 5.2.

We continue with the finite mass regime. The additional parameters are now β,μ. For the plots we will use $\mu = \xi$ (half-filling), and a value of $\beta = 0.14$. To begin with, we will keep the other parameters (especially g_{fp}) as for the previous plots, and consider the non-perturbative regime, i.e use (4.51), (4.52) for the photon self-energy. In doing so, we overestimate the range of applicability of the non-perturbative regime, in the same spirit as in Fig. 4.15. A plot of the resulting spectral function $\mathcal{A}_{\mathrm{np}}(\epsilon,\delta)$ is shown in Fig. 5.4.

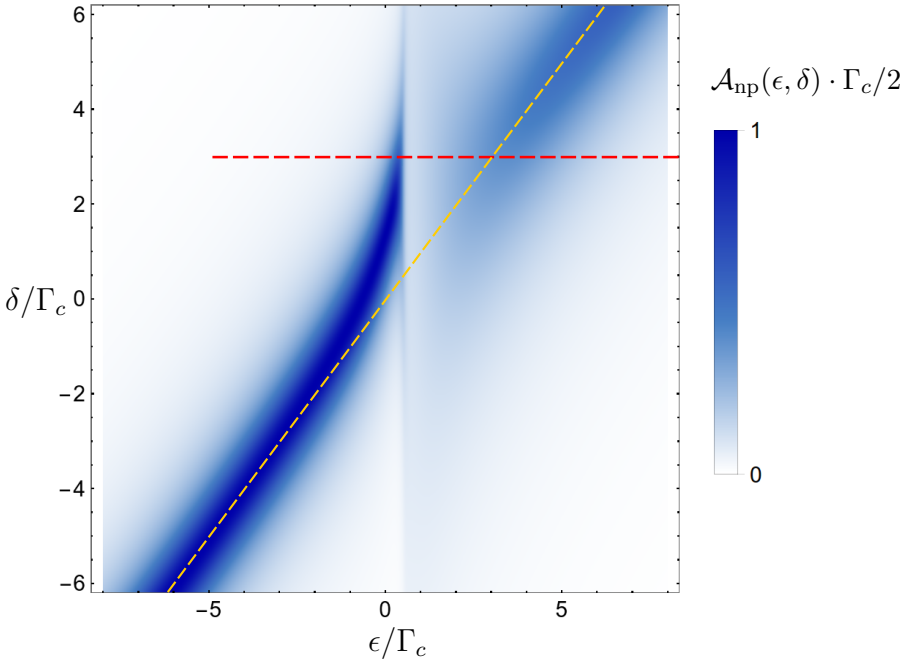

Figure 5.4.: Fermi-edge polariton spectral function $\mathcal{A}_{\mathrm{np}}(\epsilon,\delta)$ for finite masses, and in the non-perturbative regime. This plot was generated by inserting the non-perturbative photon self-energy for finite hole masses of (4.51), (4.52) into the spectral function of (5.3). The dashed red line indicates the spectral range shown in detail in Fig. 5.5. The dashed yellow line shows the bare photon mode. Used parameters: $g_{\mathrm{fp}} = 0.33\Gamma_c$, $\xi = 4\Gamma_c$, $g = 0.5$, $\mu = \xi$, $\beta = 0.14$.

One can see in comparison to the infinite mass case of Fig. 5.2, that the lower polariton branch is more similar to the bare photon mode; especially the exciton-like behaviour of the lower polariton at large positive detunings δ is cut off. This is further visualized in Fig. 5.5, where the infinite mass and the finite mass spectra at a fixed cavity detuning of $\delta = 3$ are compared.

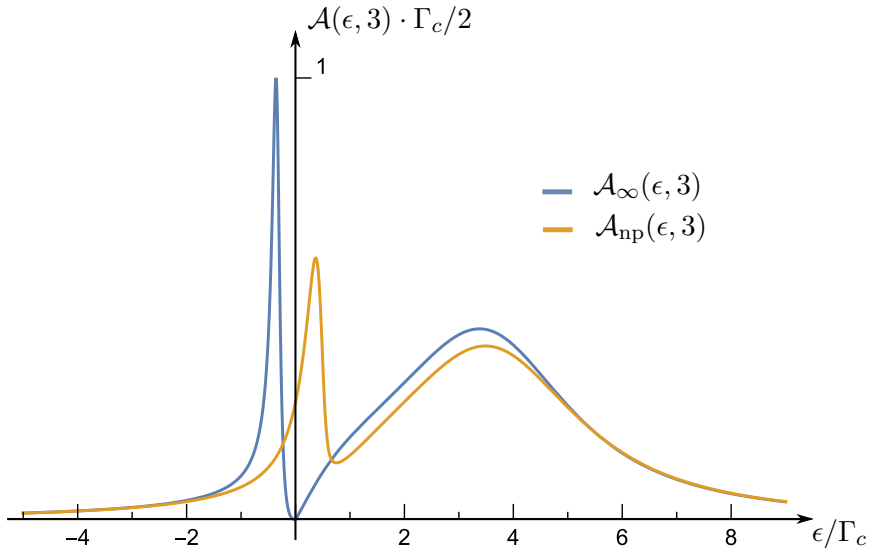

Figure 5.5.: Cut trough Figs. 5.2, 5.4, comparing the polariton spectral functions for the infinite and the finite mass cases at a fixed cavity detuning of $\delta = 3$.

It is seen that the lower, exciton-like polariton peak is sizeably broadened and cut. The reason for this behaviour is transparent: Since for finite masses excitonic features are washed out in the absorption, they are also blurred in the polariton spectral function.

In addition, the spectral weight inbetween the polariton maxima is increased, as clearly seen in Fig. 5.5. Again, this is due to the absorption cut-off. As a result, the effective splitting between the polariton branches is reduced.

Furthermore, one can see that the boundary between the polaritons is shifted from the indirect threshold $\epsilon = 0$ to the direct threshold $\epsilon = \beta\mu$, which is $0.56 \cdot \Gamma_c$ for the chosen parameters.

We continue with the perturbative regime, decreasing g. We will set $g = 0.1$. Actually, for such a small value of g the spectral plots of the finite mass case and of the infinite mass case look very similar, only slightly dependent ot the concrete photon self-energy. To be consistent with our previous evaluations, let us use the perturbative photon self-energy expressions (4.23), (4.29), and keep all other parameters unchanged. The resulting perturbative spectral function $\mathcal{A}_{\mathrm{p}}(\epsilon,\delta)$ is shown in Fig. 5.6.

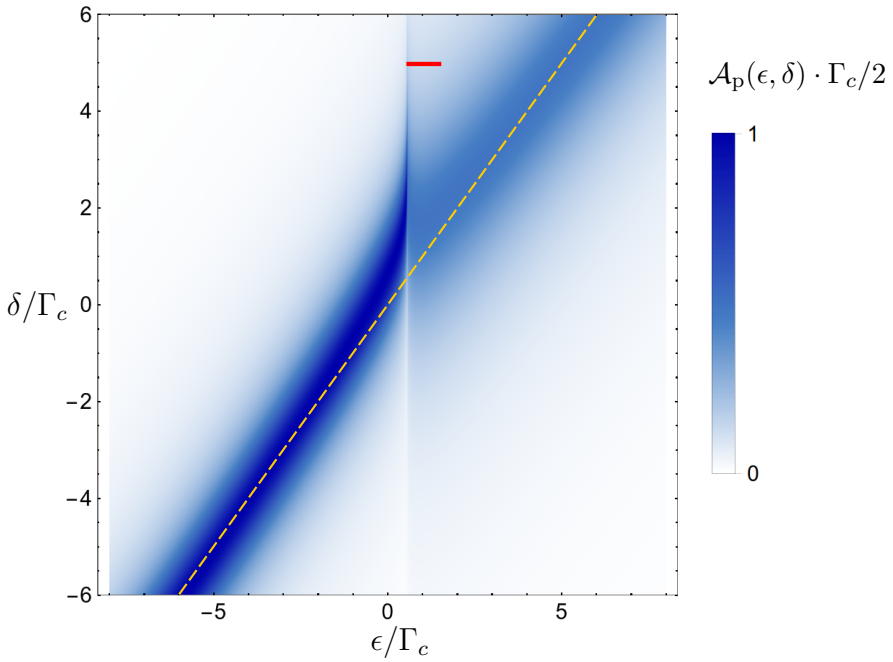

Figure 5.6.: Fermi-edge polariton spectral function $\mathcal{A}_\mathrm{p}(\epsilon,\delta)$ for finite masses, and in the perturbative regime. This plot was generated by inserting the perturbative photon self-energy for finite hole masses of (4.23), (4.29) into the spectral function of (5.3). The dashed yellow line shows the bare photon mode, the red line indicates the spectral range shown in detail in Fig. 5.7. Used parameters: $g_\mathrm{fp} = 0.33\Gamma_c$, $\xi = 4\Gamma_c$, $g = 0.1$, $\mu = \xi$, $\beta = 0.14$.

Since the excitonic enhancement of the absorption is completely cut off by the smallness of g and the finite mass, the lower polariton is almost not red-shifted anymore, it is practically photon-like. The upper polariton has approximately the same weight for all $\epsilon > 0$. Effectively, it is just a photon with an increased linewidth, which stems from the decay into the continuum of matter excitations. As a result, the mode splitting has practically vanished.

Similar to the infinite mass case, one can also try to recover the dimensional-dependent power law at the indirect threshold from Fig. 5.6. Studying the numerator of (5.3), it is however seen that the cavity linewidth Γ_c will dominate over the term $\Im[\Pi]$, containing the power law, which is at most of order $g^2 g_\mathrm{fp}$ in the regime where the power law is valid (c.f. (4.25)). Thus, extracting the power law directly from $\mathcal{A}_\mathrm{p}$ would require $\Gamma_c \ll g^2 g_\mathrm{fp}$, which is far off our current parameter regime (and also far beyond the experimental state of the art). However, we can overcome this difficulty by subtracting

$$\frac{2\Gamma_c}{(\epsilon - \delta - \Re[\Pi](\epsilon))^2 + (\Gamma_c - \Im[\Pi](\epsilon))^2}$$

from $\mathcal{A}_\mathrm{p}$. The resulting function $\tilde{\mathcal{A}}(\epsilon,\delta)$ is a polariton spectral function adjusted for the photon width. For large detunings δ and small energies ϵ, it will effectively probe the

absorption, behaving as

$$\tilde{\mathcal{A}}(\epsilon,\delta) \simeq \underbrace{\frac{2g^2 \cdot g_{\mathrm{fp}}}{\sqrt{3}\cdot\delta^2}}_{:=\alpha_2} \cdot \left(\frac{\epsilon}{\beta\mu}\right)^3 , \qquad \text{for } \epsilon \ll \beta\mu \ , \quad \delta \gg \Gamma_c, \Re[\Pi](\epsilon) \ . \tag{5.7}$$

A visualization of this fact with a double logarithmic plot for the value $\delta = 5\Gamma_c$ is shown in Fig. 5.7.

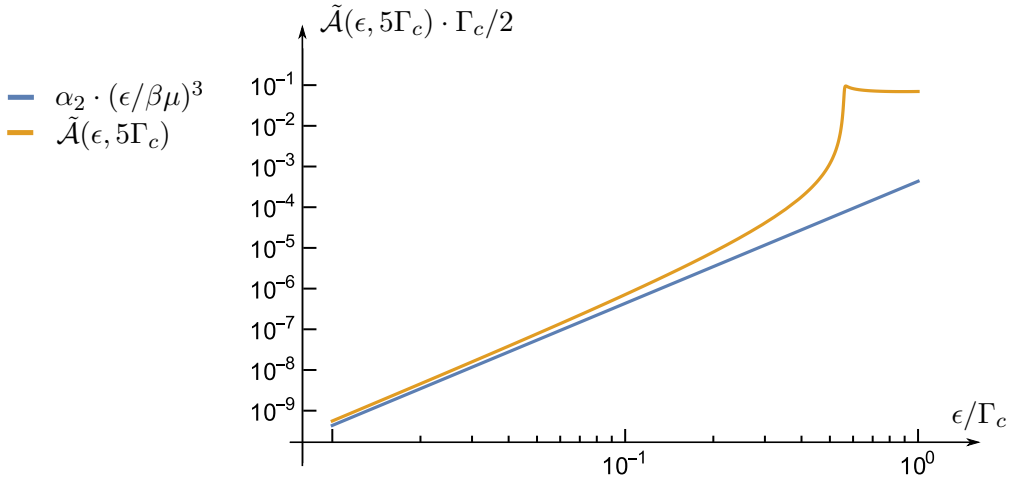

Figure 5.7.: Comparison of the power law (5.7) and the function $\tilde{\mathcal{A}}(\epsilon, 5\Gamma_c)$.

As can be seen from Fig. 5.7, the adjusted absorption $\tilde{\mathcal{A}}(\epsilon, 5\Gamma_c)$ behaves as a power law close to the indirect treshold $\epsilon \gtrsim 0$. The kink for $\epsilon \simeq \beta\mu$ is a trace of the step-like behaviour near the direct treshold.

For very small energies ϵ, this power law should also be found in the non-perturbative regime.

5.2. Polariton spectral function: experimental results

The spectral plots shown in the last section can be compared to experimental data. We will only consider the measurements found in Ref. [1]; the main data of Ref. [5] in principle look similar, but are far less detailed.

In Ref. [1], the spectral properties were studied with a differential reflection (dR) measurement (see [1], supplementary material): One illuminates the cavity with white light and measures the reflection, once tuning the cavity into resonance with the QW-transitions, and once strongly detuning it. The dR data are then given by the difference of the two measurements.

Two samples were analysed. The first one, called sample A, is a low-mobility sample, with $\mu \simeq 4$ meV. The experimental data are shown in Fig. 5.8.

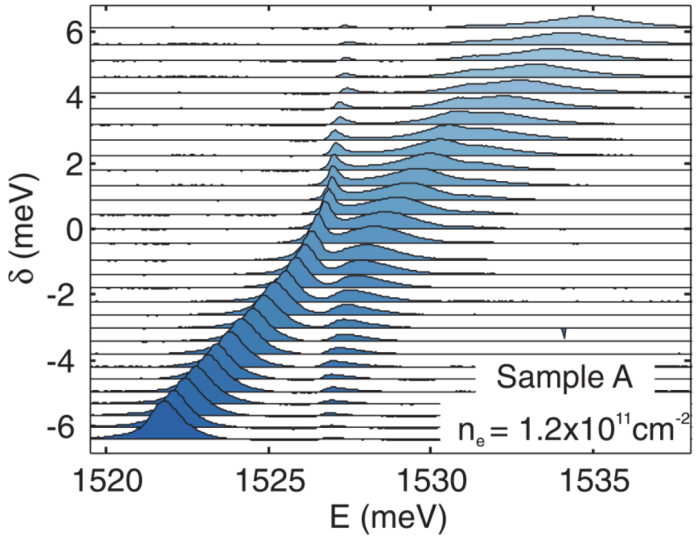

Figure 5.8.: dR measurement of the low-mobility sample A of Ref. [1].

For sample A, an infinite mass description seems to be reasonable. Furthermore, since μ is of order $E_0(\mathrm{GaAs}) \simeq 4$ meV, we assess it to be between the exciton regime and the FER, slightly closer to the exciton regime, since in 2D the exciton binding energy is $4E_0$.

This expectation is also confirmed by comparison with Figs. 5.1, 5.2: The measurement looks more exciton-like (Fig. 5.1), but with a substantial broadening of the upper polariton branch as in the FER case (Fig. 5.2).

The second measured sample (sample B) is a high-mobility one. The chemical potential is increased to roughly 6 meV. The data are presented in Fig. 5.9

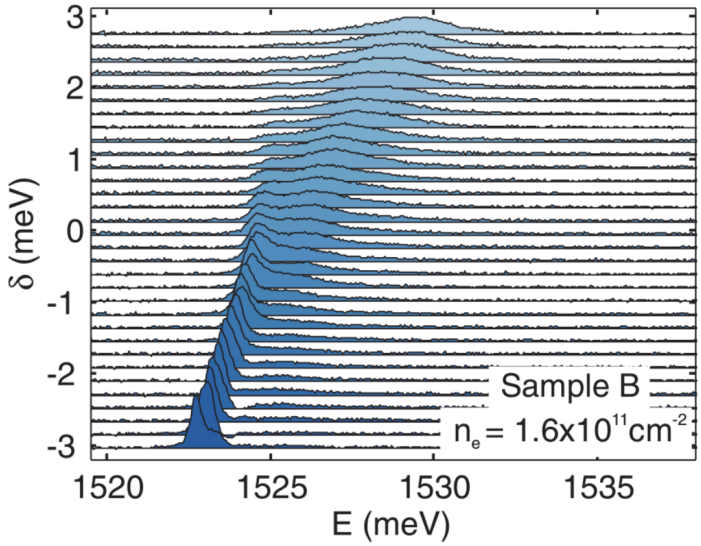

Figure 5.9.: dR measurement of the high-mobility sample B of Ref. [1].

The mode splitting is seen to vanish almost completely; the data are strongly reminiscent of the perturbative FER regime, see Fig. 5.6.
Certainly, since μ is still of order E_0, we cannot hope for a quantitative agreement with our results, and the parameters of sample B are not quite in the perturbative FER regime. However, we believe that the general trend of a vanishing mode splitting, observed when changing from sample A to sample B, is contained in our results, since:

- The chemical potential is increased as compared to sample A, leading to a larger value in the argument of the relevant logarithmic parameter $l := |g \log(g^2 \beta \mu / \xi)|$ (c.f. 3.33)), and thus to a smaller value of l.
- This increase of μ also leads to a smaller value of g (c.f. (2.17)), which is actually the dominant effect regarding polariton spectra.
- One can assume that β changes from 0 (where the logarithms are always diverging at the treshold, thus no perturbative regime exists) to 0.14, which will further increase the cutoff of the logarithm.

All these modifications decrease l, in an extremal case resulting in a perturbative spectrum as in Fig. 5.6.

5.3. Polariton dispersion: theoretical results

Further physical information can be extracted from plots of the polariton dipersion, allowing for a finite photon momentum. Disregarding the momentum for the photon self-energy as was discussed on page 25, and restricting ourselves to small momenta, the only momentum-dependence is then contained in an additional term $k^2/2m_{\mathrm{cav}}$ in the denominator of the photon Green's function, where m_{cav} is the cavity mass (c.f. (1.7)).

5.3.1. Exciton regime

To begin with, let us first present a plot of the dispersion in the exciton regime. We use the formulas and parameters of section 5.1.1, including the momentum term. Following Ref. [1], we plot the exciton-polariton spectral function $\mathcal{A}_{\mathrm{ep}}(k, \epsilon, 0)$, tuning the cavity into resonance with the exciton mode, i.e. $\delta = 0$. The photon momentum k is plotted in units of

$$k_0 := \sqrt{2 m_{\mathrm{cav}} \Gamma_c} \,, \tag{5.8}$$

For typical cavities (restoring a factor of $1/\hbar^2$), $k_0 \simeq 1/\mu\mathrm{m}$. The resulting plot is shown in Fig. 5.10.

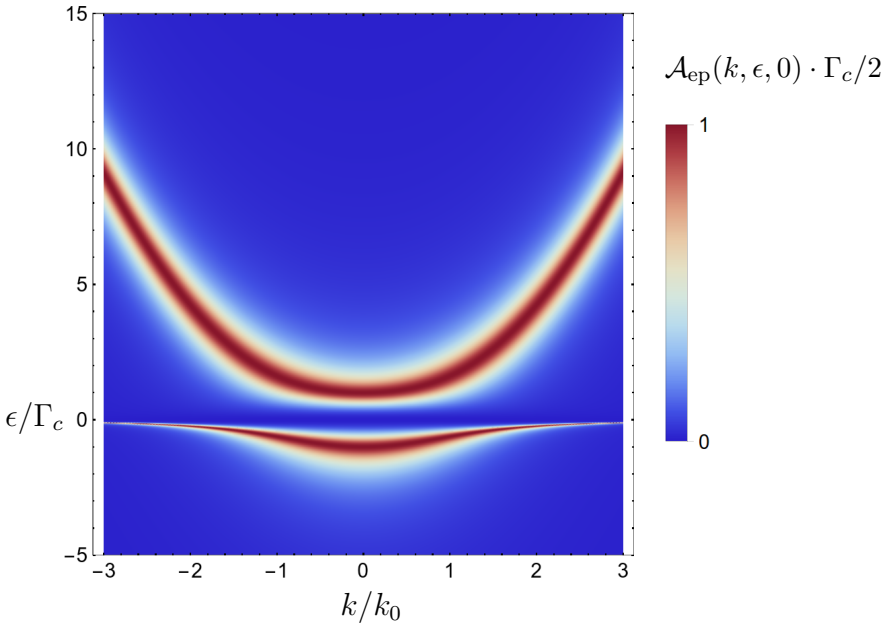

Figure 5.10.: Exciton-polariton dispersion spectrum $\mathcal{A}_{\mathrm{ep}}(k,\epsilon,0)$. The unit k_0 is defined in (5.8).

Two distinct polariton branches are seen, split by $2g_{\mathrm{ep}}$. It can be infered from Fig. 5.10 that the effective mass of the polaritons close to $k=0$ is approximately $2m_{\mathrm{cav}}$, as already apparent from the polariton energies (1.65). For large momenta, where the photon mode is strongly blue-detuned w.r.t. the exciton mode, the lower polariton becomes exciton-like, i.e. flat and with a vanishing linewidth. By contrast, the upper polariton becomes light-like, approaching a parabola with effective mass m_{cav}, and photon linewidth.

5.3.2. Fermi-edge regime

We proceed to the FER. To begin with, we consider the infinite mass case, using the parameters of Fig. 5.2. The resulting plot is shown in Fig. 5.11.

As for the detuning spectra, the lower polaritons in the exciton regime and the infinite mass FER regime look very similar. The upper polariton, however, is not seen as a well defined quasiparticle for small momenta. As discussed before, this is due to the incoherent decay into matter excitations, which manifests itself in a large value of the absorption for $\epsilon \gtrsim 0$.

For large momenta respectively large energies, where the absorption decays as a power law, the photonic mass-parabola revives in the spectrum.

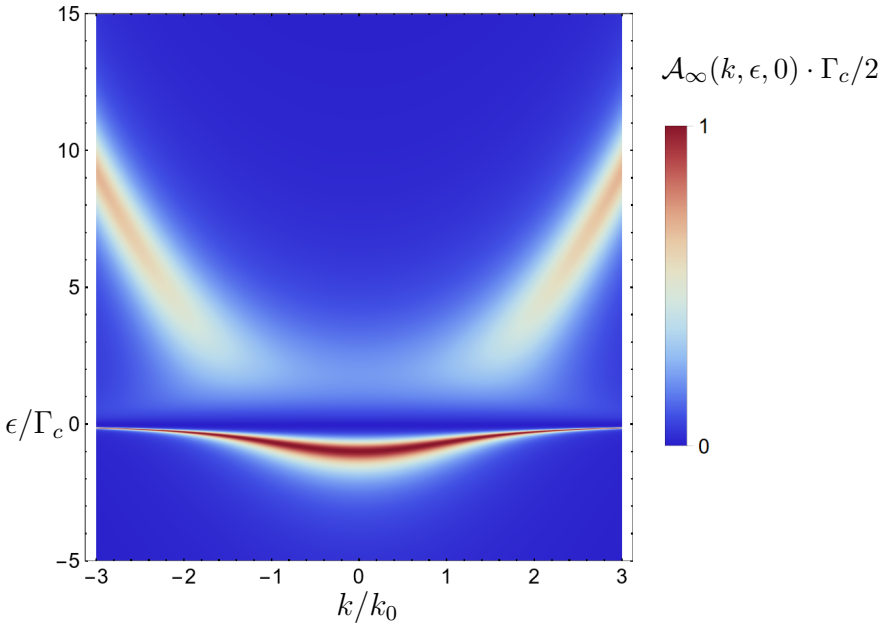

Figure 5.11.: Fermi-edge polariton dispersion spectrum $\mathcal{A}_\infty(k,\epsilon,0)$ for infinite hole mass

Switching on a finite mass ($\beta = 0.14$) in the non-perturbative regime, with the parameters of Fig. 5.4, and tuning the photon mode to the direct threshold at $\delta = \beta\mu$, produces the spectral function $\mathcal{A}_{\mathrm{np}}(k,\epsilon,\beta\mu)$ shown in Fig. 5.12.

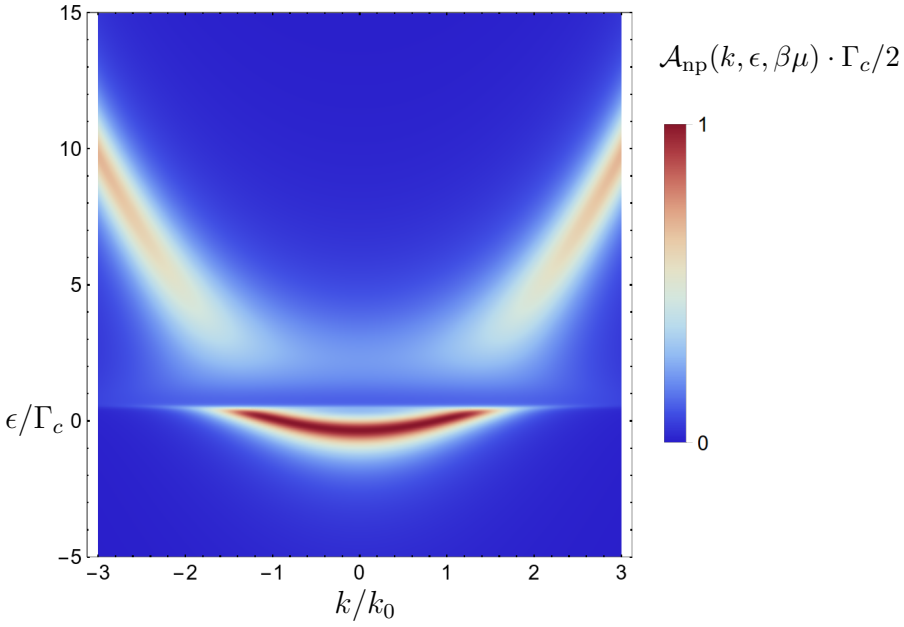

Figure 5.12.: Fermi-edge polariton dispersion spectrum $\mathcal{A}_{\mathrm{np}}(k,\epsilon,\beta\mu)$ for finite masses, and in the non-perturbative regime.

In comparison to Fig 5.11 one can clearly see a threshold shift; furthermore, since the absorption peak is less pronounced compared to the infinite mass case, one observes a sligthly reduced mode-splitting. In addition, the narrow exciton-type tail of the lower

polariton is washed out.

Finally, Fig. 5.13 shows a plot of the polariton dispersion in the perturbative regime, using the parameters of Fig. 5.6.

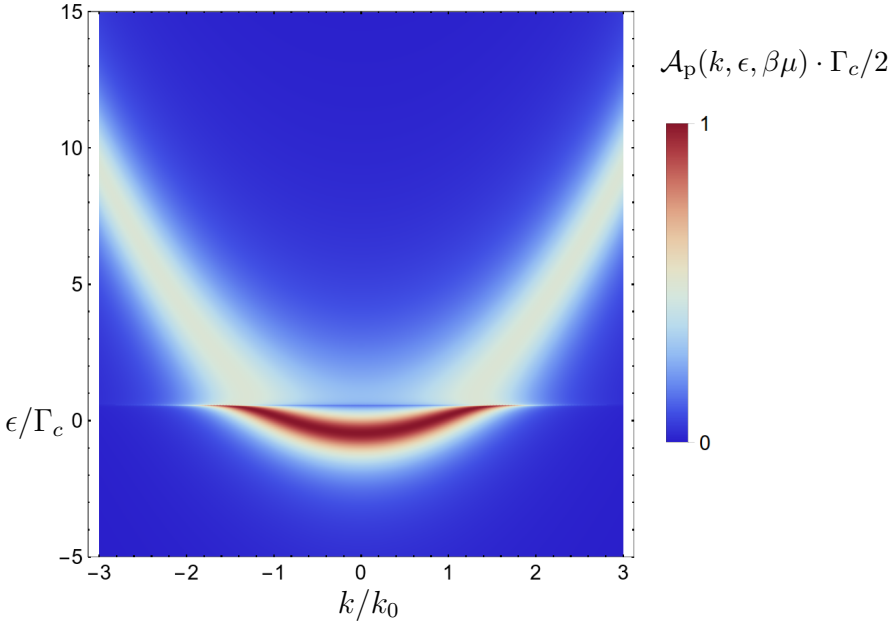

Figure 5.13.: Fermi-edge polariton dispersion spectrum $\mathcal{A}_\mathrm{p}(k,\epsilon,\beta\mu)$ for finite masses, and in the perturbative regime.

The mode splitting has practically vanished; the spectrum is turned into a single mass parabola, but with increased linewidth above the indirect threshold. As distinct from the previous dispersion plots, the upper polariton linewidth is not seen to approach the photon linewidth at large energies, but this is an artefact of our theta-like perturbative self-energy, which is not cut off by finite bandwidth-effects.

5.4. Polariton dispersion: experimental results

We can also compare the dispersion plots to the results of Ref. [1]. Experimentally, the photon momentum can be modified tilting the light-source w.r.t. the quantum well.

The measurement was conducted for the low-mobility sample A only. The data are shown in Fig. 5.8.

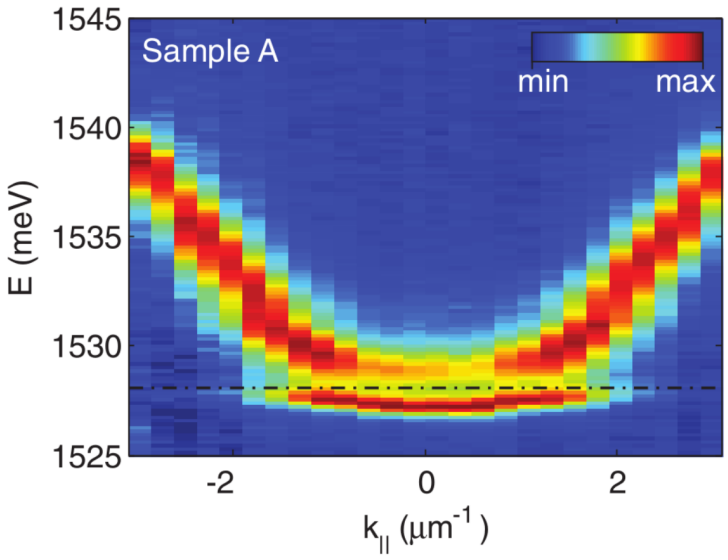

Figure 5.14.: dR dispersion measurement of the low-mobility sample A of Ref. [1].

As discussed on page 97, sample A is expected to be inbetween the exciton and infinite mass FER regime. Comparing the dispersion plot of Fig. 5.14 with Figs. 5.10, 5.11 further confirms this statement. The measurement looks slightly more exciton-like (Fig. 5.10); however, the upper polariton is also washed out for small momenta (as seen in the "hole" of the upper parabola), similar to the FER of Fig. 5.11.

In [1], also the polariton mass is deduced from the measurement, and it is indeed found to be approximately $2m_{\mathrm{cav}}$.

6. Conclusion and outlook

We have investigated the properties of Fermi-edge polaritons in heavily doped semiconductor quantum wells. Our focal point of interest was the description of high-mobililty samples, corresponding to a finite mass of the valence band electrons.

To begin with, we have identified the photon self-energy as the quantity determining the optical properties of the microcavities under consideration. It's imaginary part is of special interest, since it allows one to derive the absorption of the quantum well.

We restricted ourselves to the calculation of the self-energy in linear response, relating it to the dressed electron-hole bubble.

To properly describe heavily doped systems, we considered the theoretical regime of a large Fermi energy, called Fermi-edge regime. In this regime, the effective electron-hole interaction coupling constant g was found to be small, thus allowing for perturbation theory in g.

As a preliminary step in the evaluation of the photon self-energy in the Fermi-edge regime, we then calculated the Green's function of valence band hole for finite hole mass. Two diagrammatical methods were presented and compared: the linked-cluster expansion and the standard Dyson equation. We have used the first method to obtain the spectral function $\mathcal{A}_h$ of the valence band hole for zero hole momentum. $\mathcal{A}_h$ was shown to have an unusual shape, consisting of a coherent and an incoherent part. This result is in agreement with previous works [35].

We identified the phase space function for conduction band electron-hole scattering processes as the main quantity determining the shape of $\mathcal{A}_h$. This allowed for a transparent physical interpretation of our results. Qualitatively, a reduced scattering phase space results in narrower, particle-like spectral features.

The Dyson equation was used to calculate the hole spectral function for incoming Fermi-momentum. We showed that, due to an enlarged scattering phase space, the hole has a finite lifetime.

After these steps, we were in a position to calculate the photon self-energy in the Fermi-edge regime for finite hole mass. To obtain a first understanding, an approach suggested by Mahan [6] was used, guessing the full series from second order in g. The finite hole mass resulted in different cutoffs of logarithms, and in the appearance of two thresholds, the direct and indirect one. We assessed the range of validity for our theory by analysing the cutoffs. In the parametric range of control, the self-energy was then found to have the form of a cut-off power law for energies near the direct threshold Ω_D, which is a consequence of the finite hole lifetime.

We further investigated this result in the following analysis, which was based on a work by Gavoret, Nozières et al. [27]. We computed the behaviour of the photon self-energy near Ω_D, solving a Bethe-Salpeter equation with logarithmic accuracy. Furthermore, the self-energy close to the indirect threshold Ω_I was obtained. It was shown that $\Im[\Pi]$ vanishes at Ω_I with a dimensional-dependent power law, reproducing the results found in Ref. [42].

As the final step, we evaluated polariton properties. Inserting the computed photon self-energy into the photon Greens function, the polariton spectral function $\mathcal{A}$ was evaluated. The physical discussion was developed based on plots of $\mathcal{A}$ as a function of the energy and the cavity detuning. We have found that the resulting two polariton branches are of a completely different nature in the Fermi-edge regime. While the lower polariton is always particle-like, the upper polariton is strongly smeared due to the decay of the photonic mode into the incoherent continuum of matter excitations. Furthermore, the peak splitting between the polaritons was shown to depend strongly on the light-matter-interaction, the electron-hole-interaction, and the hole mass. For a high-mobility sample at high electron densities resulting in weak electron hole interaction, the peak splitting was seen to vanish almost completely. Comparing our results to the experimental data of Ref. [1], we found evidence for such a behaviour.

We also analysed dispersions plots of $\mathcal{A}$ at zero detuning, finding them to support our previous statements.

Our work is only as a first step towards a complete theory of Fermi-edge polaritons. Many further improvements are conceivable. For example, one can try to extend our analysis to a larger parameter range. This could be accomplished via a calculation of first order diagrams beyond logarithmic accuracy, or a consistent ladder approximation (see discussion on page 71). One could also try to go beyond linear response for the photon self-energy and include other classes of diagrams in addition to the dressed electron-hole bubble.

Furthermore, one could attempt to include more realistic electronic interactions. Potential improvements are electron-electron interactions, and a screened Coulombic electron-hole interaction.

A numerical evaluation seems promising to check the analytical results and to gain insight into spectral regions far from the thresholds. We have already made a first step in this direction, applying the method of functional renormalization group; however, we will not present it here.

As we have discussed in detail, the experiment of Ref. [1] does not quite belong to the Fermi-edge regime. If this limitation is removed, our statements can be checked directly, especially in cavities with a smaller photon linewidth. One could also use samples based on materials with a different mass ratio β, in order to analyse the hole mass dependence in detail.

Finally, one could attempt to go beyond the FER analytically. Even if the conduction band is only sligthly populated (i.e. in a pure exciton regime), taking into account the Fermi-sea shake-up in a consistent manner is difficult. Although some results on this are reported in Refs. [40], [51], to our knowledge the mass dependence was not yet taken into consideration in a satisfactory fashion. A first attempt of a perturbative treatment in this regime is presented as a supplement, c.f. chapter 7.

If the implications of the Fermi-sea shake-up for the polariton formation are understood, one could proceed exploring polariton interaction effects, and properties resulting from the quasi-bosonic nature of the polariton. This could open up a wide field of future research.

7. Supplement: calculations in the exciton regime

We will now briefly present a first step in the calculation of spectral properties in the exciton regime, without showing calculations in detail. This part is work in progress, and the results are only preliminary.

Retaining the contact interaction model, the exciton regime is defined by

$$E_B \gg \mu \ , \tag{7.1}$$

where E_B is the binding energy of the Mahan exciton (c.f. (3.14)). An equivalent statement would be

$$1/a_0 \gg k_F \ , \tag{7.2}$$

where a_0 is the excitonic Bohr radius. Restricting ourselves to spinless particles for simplicity, the coupling constant g reads: (c.f. (1.71)):

$$g = \frac{1}{a_0(k_F + 1/a_0)} \lesssim 1 \ . \tag{7.3}$$

Thus, perturbation theory in g is meaningless, since higher order diagrams contribute equally. Following a suggestion by Moshe Goldstein [52], in the following we will show a way to circumvent this obstacle.

To recover the exciton, we have to sum up the series of ladder diagrams, and consider energies close to the exciton binding energy $-E_B$.

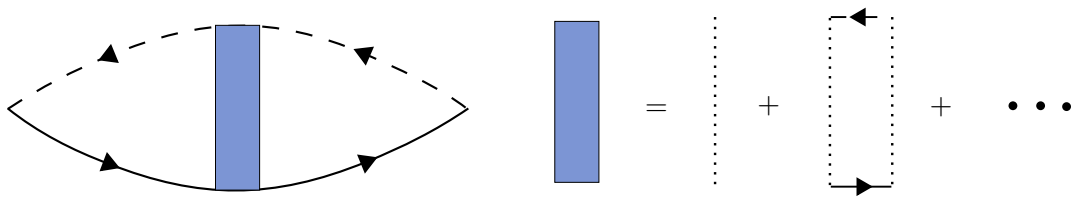

Figure 7.1.: The exciton ladder.

7.1. Exciton spectral function for infinite hole mass

To begin with, we consider the case of infinite hole mass. Disregarding the optical matrix element, a ladder diagram with n interaction lines reads (c.f. (3.11)):

$$\Pi^{(n)}_{\text{Ladder}}(\epsilon) = \rho(-g)^n \log\left(\frac{-\epsilon - i\Gamma}{\xi}\right)^{(n+1)} \ , \tag{7.4}$$

where ϵ is the detuning from $\Omega_I = E_G + \mu$, and Γ is the linewidth which we will let to zero in the end of the calculation. On the other hand, in crossed diagrams, terms of the form

$$\Pi_c = \log\left(\frac{-\epsilon - i\Gamma}{\mu - \epsilon}\right) \tag{7.5}$$

appear. Distinct from the FER regime, now the scales read

$$\xi \gg E_B \gg \mu \ . \tag{7.6}$$

Thus, we do not have to take the crossed diagrams into account for energies close to the exciton binding energy $-E_B$. Summing the whole ladder, we obtain the following expression:

$$\Pi_{\text{Ladder}}(\epsilon) \simeq \underbrace{\frac{\rho E_B}{g^2}}_{:=\alpha} \cdot \frac{1}{\epsilon + E_B + i\Gamma} \ . \tag{7.7}$$

This expression is valid for $\epsilon \simeq -E_B$. It especially breaks down for $\epsilon > 0$, where for the absorption we recover the continuum of states corresponding to a smeared theta-function. The factor α will appear as global prefactor in all diagrams.

We now measure the energy ω from $-E_B$, and define the exciton Green's function:

$$G_{\text{exc}}(\omega) = \frac{1}{\omega + i\Gamma} \ . \tag{7.8}$$

The infinite mass of the hole carries over to the exciton (it's mass is just the sum of electron and hole mass), s.t. the excitons in this section are momentum independent. For a nonvanishing μ, we expect that in the energy regime $\omega < \mu$ the delta function spectrum corresponding to (7.8) will be turned into a power law by scaterrings with CB electrons. In the following we will restrict ourselves to such small detunings $\omega < \mu \ll E_B$.

The powerlaw exponent was calculated in terms of electron scattering phase shift δ in Ref. [40] and can also be deduced from Hopfield's rule of thumb. Let us recall it in this context: The behaviour of spectral functions $\mathcal{A}(\omega)$ in the infinite mass case is

$$\mathcal{A}(\omega) \sim \omega^{\gamma^2 - 1} \ , \qquad \gamma = \delta/\pi - 1; \tag{7.9}$$

γ represents the number of electrons moved from infinity to a finite volume around the local potential, described by δ/π, minus the number of electrons added to the Fermi sea in the process of the hole-potential creation. In the usual picture, the creation of a hole comes with one additional electron in the Fermi sea, thus $\gamma = (\delta/\pi - 1)$. In the limit $g \to 0$ one has $\delta/\pi = g$, which leads to the standard Fermi-edge singularity.

In the excitonic picture, one exciton and no addional electron is created. In terms of the phase shift δ_{exc} of electrons scattering off an exciton, thus $\gamma = \delta_{\text{exc}}/\pi$.

Now we aim to do perturbation theory in the exciton picture, in terms of an effective exciton-electron interaction g_{exc}. Regarding (7.9) as a spectral function for an infinite mass exciton, we expect $g_{\text{exc}} = \delta_{\text{exc}}/\pi = \delta/\pi - 1$. As an Ansatz, we can replace δ/π by g, which leads to:

$$g_{\text{exc}} = g - 1 \ , \tag{7.10}$$

which is a small quantity which we can treat in a perturbative way. Of course, this is not fully accurate, since for $g \lesssim 1$ the replacement of δ/π by g is incorrect. We regard (7.10) as a first step which will show how in the presence of a Fermi-sea the particle-spectrum of (7.8) is converted into a powerlaw; the detailed form of g_{exc} as function of g remains to be found.

Let us try to recover the relation (7.10) diagrammatically. The following two diagrams are relevant:

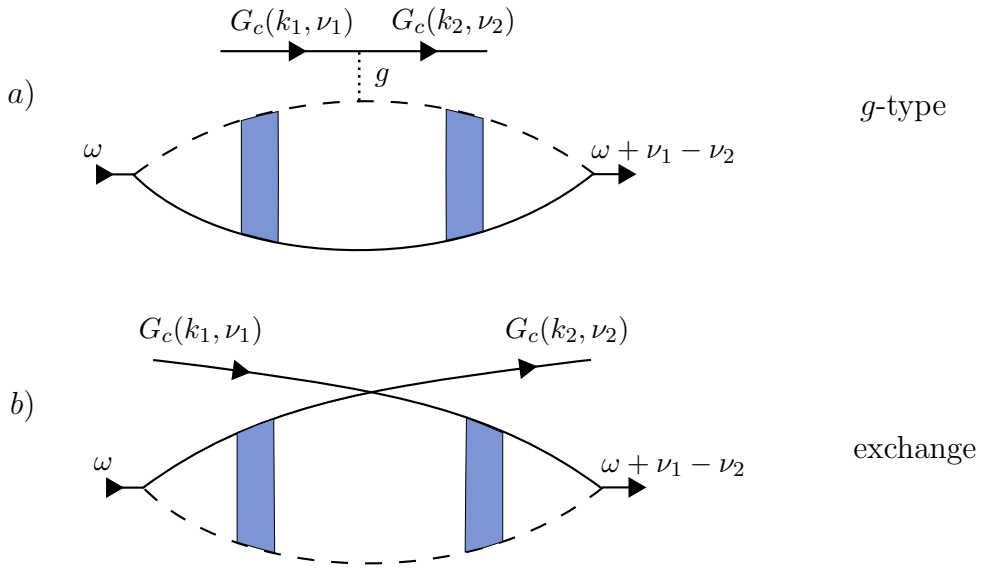

Figure 7.2.: Relevant diagrams for the effective electron-exciton interaction. To emphasize that the first diagram involves an electron-hole interaction, we will call it *g-type*.

We computed these diagrams, assuming that the electron energies fulfill $\nu_1, \nu_2 \ll E_B$. The CB Green's functions factor out, and the exciton part reads

$$a) \qquad -g \cdot \alpha G_{\text{exc}}(\omega) G_{\text{exc}}(\omega+\nu_1-\nu_2) \tag{7.11}$$

$$b) \qquad \alpha G_{\text{exc}}(\omega) G_{\text{exc}}(\omega+\nu_1-\nu_2)\ . \tag{7.12}$$

These expressions can be combined to give an electron-exciton interaction with the coupling constant $g_{\text{exc}} = g - 1$. A sketch of this is shown in Fig. 7.3.

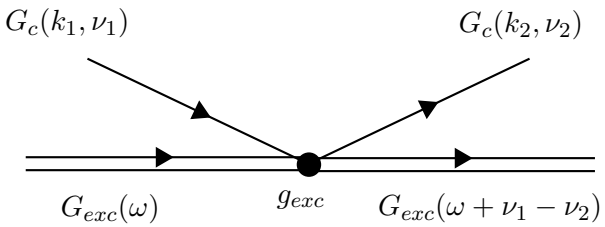

Figure 7.3.: Exciton-electron interaction. The double line represents an exciton.

We will now show that the higher order ladder diagrams correctly reproduce the

spectral function

$$\mathcal{A}_{\mathrm{exc}}(\omega) \sim \omega^{g_{\mathrm{exc}}^2 - 1} \tag{7.13}$$

to lowest order. $\mathcal{A}_{\mathrm{exc}}$ is nothing but the absorption close to the exciton pole.

As was the case for holes (c.f. chapter 2), the first order contribution simply shifts E_B, and the contribution responsible for the Anderson orthogonality arises from second order. Extending the diagrams of Fig. 7.2 to second order and closing the electron loops gives three diagrams. The first one is shown in Fig 7.4.

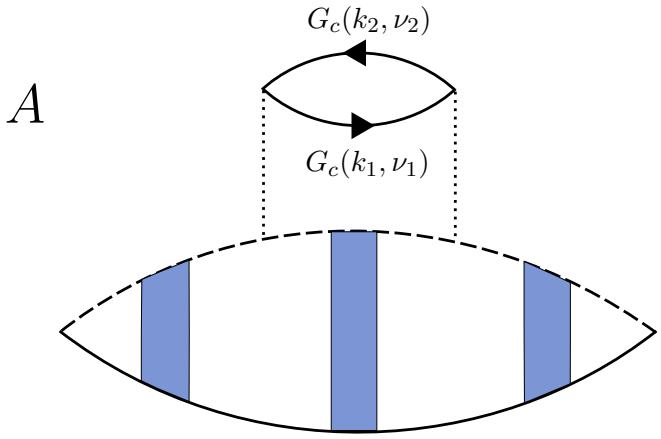

Figure 7.4.: Second order diagram coming from the combination of two g-type diagrams. We will call this diagram A.

The frequency integrals are simple contour integrals. The part relevant for the imaginary part of the exciton self-energy contains two momentum integrals:

$$\Im\left[\Sigma_A\right](\omega) \sim \int_0^{\xi} d\epsilon_1 \int_{-\mu}^{0} d\epsilon_2 \; \Im\left[G_{\mathrm{exc}}(\omega + \epsilon_2 - \epsilon_1)\right] \tag{7.14}$$

$$\epsilon_i = \frac{k_i^2}{2m} \; . \tag{7.15}$$

This expression shows that it was correct to assume that the electronic energies (which are essentially ϵ_1, ϵ_2) are much smaller than E_B: For ϵ_2 this is obvious, and for $\epsilon_1 > \omega$, $\Im\left[G_{\mathrm{exc}}\right]$ will vanish.

For $\omega \ll E_B$ we can use (7.8), and obtain as a result:

$$\Im\left[\Sigma_A\right](\omega) = -\pi\alpha g^2 \theta(\omega) \cdot \omega \; . \tag{7.16}$$

The remaining two diagrams are shown in Fig. 7.5.

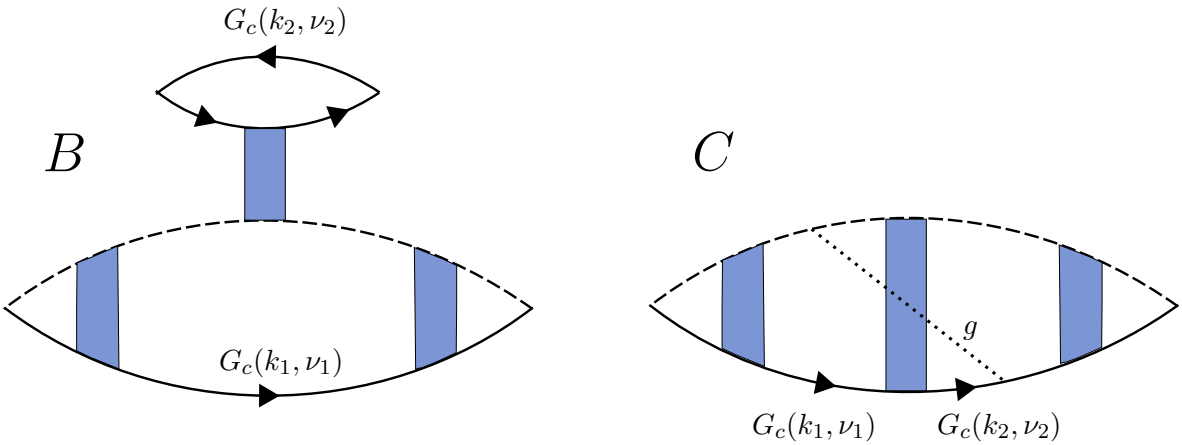

Figure 7.5.: Remaining second order diagrams. Diagram B is a combination of two exchange-diagrams, diagram C is a combination of one g-type and one exchange diagram.

The contributions of Fig. 7.5 are calculated in the same way as for diagram A. They read:

$$\Im\left[\Sigma_B\right](\omega) = -\pi\alpha\theta(\omega)\cdot\omega \tag{7.17}$$

$$\Im\left[\Sigma_C\right](\omega) = +\pi\alpha g\theta(\omega)\cdot\omega\ . \tag{7.18}$$

Combining all three diagrams, and noting that there are two diagrams of type C, leads to:

$$\Im\left[\Sigma\right](\omega) = -\pi(g_{\text{exc}})^2\alpha\theta(\omega)\cdot\omega\ . \tag{7.19}$$

Recovering the real part using Kramers-Kronig relations gives:

$$\Re\left[\Sigma\right](\omega) = \alpha(g_{\text{exc}})^2\omega\log(\omega/\mu)\ . \tag{7.20}$$

This corresponds to the result for the real part of hole self-energy in lowest order (c.f. (2.51)), except for a spin-factor of 2. The main difference is that the full quantity controlling the expansion now reads $g_{\text{exc}}^2\cdot\log(\omega/\mu)$ instead of $g^2\log(\omega/\xi)$.

For the time being, our understanding of the exciton diagrammatic expansion is the following: An n-th order exciton diagram corresponds to a diagram with n distinct ladders. We expect that these diagrams cancel and add up in such a way that a global factor of $(g_{\text{exc}})^n$ can be extracted, which we have shown to second order. An extension of this statement to higher orders or even a general proof remains to be accomplished.

7.2. Exciton spectral function for finite hole mass

Let us advance to the case of finite hole mass. For external momentum Q, the basic logarithm of the ladder diagrams now reads

$$\log\left(\frac{-\nu + Q^2/2M_+ - i\Gamma + \mathcal{O}(\beta\mu/E_B\cdot Q^2/2M_+)}{\xi(1+\beta)}\right)\ , \tag{7.21}$$

where $M_+ = m + M$, and ν is measured from the direct threshold $E_G + \mu(1+\beta)$. Disregarding the terms smaller by the factor $(\beta\mu/E_B)$, we obtain for the exciton Green's function in terms of detuning from $-E_B$:

$$G_{\mathrm{exc}}(Q,\omega) = \frac{1}{\omega - Q^2/2M_+ + i\Gamma} \ . \tag{7.22}$$

7.2.1. Exciton momentum Q = 0

To begin with, we consider zero external momentum for the excitons. Proceeding in the same fashion as in the previous section, the relevant self-energy part coming from the diagram A reads:

$$\Im\left[\Sigma_A(0,\omega)\right] \sim \int_{k_1>k_F} d\mathbf{k}_1 \int_{k_2<k_F} d\mathbf{k}_2 \ \delta(\omega - \epsilon_1 + \epsilon_2 - q^2/2M_+) \tag{7.23}$$

$$\mathbf{q} = \mathbf{k}_1 - \mathbf{k}_2 \ , \qquad \epsilon_i = (k_i)^2/2m \ . \tag{7.24}$$

The leading order in ω of this integral can be calculated in a similar way as shown in section. 4.1.1. To repeat things shortly, in all subsequent calculations $\mathbf{k}_1$ and $\mathbf{k}_2$ have to be close to k_F, which gives a factor of ω. Additional factors pile up due to the restriction of angles in order for q to be small. As a result, for $\omega \ll \beta\mu$, we obtain for a d-dimensional system:

$$\Im\left[\Sigma_A(0,\omega)\right] \sim -\alpha g^2 \omega \cdot \left(\frac{\omega}{\beta\mu}\right)^{(d-1)/2} \cdot \theta(\omega) \ , \qquad d = 2,3 \ . \tag{7.25}$$

up to factors of order 1. We also do not distinguish between β and $m/M_+ = \beta + \mathcal{O}(\beta^2)$. For the other two diagrams the calculation is analogous, s.t. in total we arrive at:

$$\Im\left[\Sigma(0,\omega)\right] \sim -\alpha g_{\mathrm{exc}}^2 \ \omega \cdot \left(\frac{\omega}{\beta\mu}\right)^{(d-1)/2} \cdot \theta(\omega) \ . \tag{7.26}$$

In all following evaluations we will only take into account $\Im[\Sigma]$, disregarding the real part. This approximation will certainly be correct in the limit $\omega \to 0$; in other frequency regimes, it's validity remains to be examined.

In this way, for the exciton spectral function $\mathcal{A}_{\mathrm{exc}}$ we obtain:

$$\mathcal{A}_{\mathrm{exc}}(0,\omega) \sim \alpha g_{\mathrm{exc}}^2 \cdot \frac{1}{\omega} \left(\frac{\omega}{\beta\mu}\right)^{(d-1)/2} \cdot \theta(\omega) \ , \qquad \omega \ll \beta\mu \ . \tag{7.27}$$

The result (7.27) coincides with the $(Q = 0)$ behaviour of the VB hole as found for 2D in section 2.2.2; in 3D it can be checked against the results of Ref. [35]. In 2D we can also expect the spectral function to have a quasi-particle delta peak with the weight missing by the change of the powerlaw from $g_{\mathrm{exc}}^2 - 1 \gtrsim -1$ to $-1/2$.

In the opposite limit $\omega \gg \beta\mu$, i.e. for energies much larger than the characteristic exciton kinetic energy, we recover the infinite mass powerlaw, as is also obvious from (7.23). Again specializing to 2D from now on, a sketch of the $(Q = 0)$ spectral function is shown in Fig. 7.6:

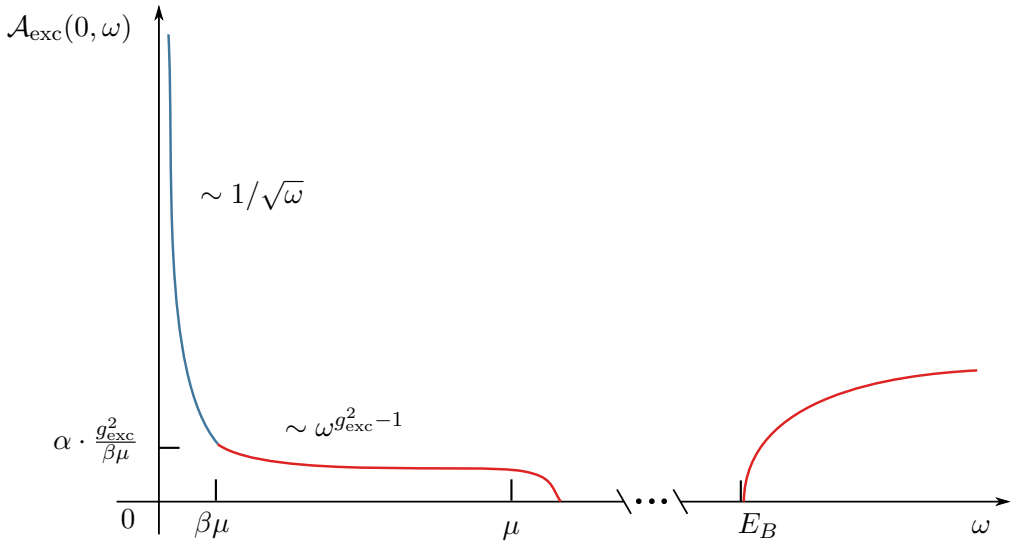

Figure 7.6.: Sketch of the $(Q = 0)$ exciton spectral function.

7.2.2. Exciton momentum $0 < Q \ll k_F$

In this case, the relevant self-energy is found to be:

$$\Im\left[\Sigma_A(Q,\omega)\right] \sim \int_{k_1>k_F} d\mathbf{k}_1 \int_{k_2<k_F} d\mathbf{k}_2 \; \delta(\omega - \epsilon_1 + \epsilon_2 - (Q-q)^2/2M_+) \; . \tag{7.28}$$

Now a new regime opens up: $\omega < Q^2/2M_+$. We also recover the notion of a direct threshold $\omega_D = Q^2/2M_+$ (not to be confused with the direct threshold for the absorption at $\omega = E_B$), and of an indirect threshold $\omega_I = 0$: The lowest energy required to create an exciton with momentum Q is just E_B, since the momentum can be tranferred to an electron-hole excitation of the Fermi sea at no energy cost. A sketch of the thresholds is shown in Fig. 7.7.

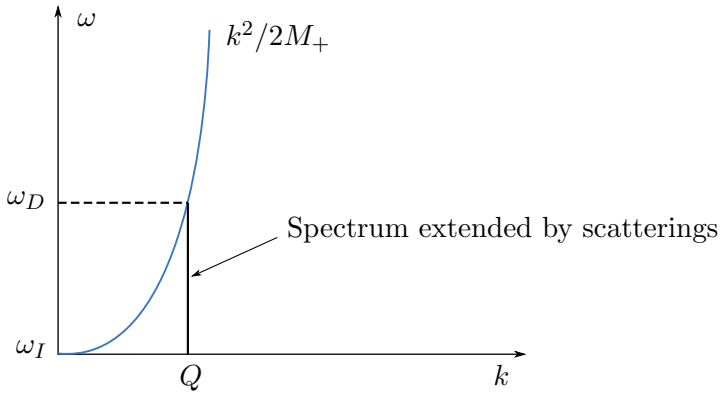

Figure 7.7.: Sketch of the two thresholds for external exciton momentum Q.

For the imaginary part of the self-energy we obtain:

$$\Im\left[\Sigma(Q,\omega)\right] \sim -\alpha g_{\mathrm{exc}}^2 \; \omega \cdot \sqrt{\frac{\omega}{Q^2/2M_+}} \sqrt{\frac{\omega}{\beta\mu}} \cdot \theta(\omega) \qquad \omega \ll Q^2/2M_+ \; . \tag{7.29}$$

This leads to a spectral function that behaves like

$$\mathcal{A}_{\text{exc}}(Q,\omega) \sim \alpha g_{\text{exc}}^2 \cdot \frac{\omega^2}{(Q^2/2M_+)^{5/2}\sqrt{\beta\mu}} \cdot \theta(\omega) \ , \qquad \omega \ll Q^2/2M_+ \ . \tag{7.30}$$

In the energy range $Q^2/2M_+ \ll \omega \ll \beta\mu$ we can disregard the Q-term in (7.28), and thus recover the $(Q = 0)$ behaviour.

Finally, for $\omega \gg \beta\mu$ we recover the $(M = \infty)$ behaviour.

Another property of interest is the linewidth of the Q-exciton, i.e. $\Im\left[\Sigma(Q, Q^2/2M_+)\right]$. Using the Lindhard-funciton as given in Ref. [37], we are able to calculate it exactly, and find that inserting $\omega = Q^2/2M_+$ into (7.29) reproduces the correct order of magnitude:

$$\Im\left[\Sigma(Q, Q^2/2M_+)\right] \sim -\alpha g_{\text{exc}}^2 Q^2/2M_+ \cdot Q/k_F \ . \tag{7.31}$$

This extra suppression by the factor Q/k_F comes from the fact that a small incoming momentum Q strongly rectricts the momentum transfer q in a scattering process: The energy of the scattered exciton with momentum $Q - q$ must be smaller than the energy of the exciton with momentum Q. Alltogether, we obtain a spectral function as shown in Fig. 7.8:

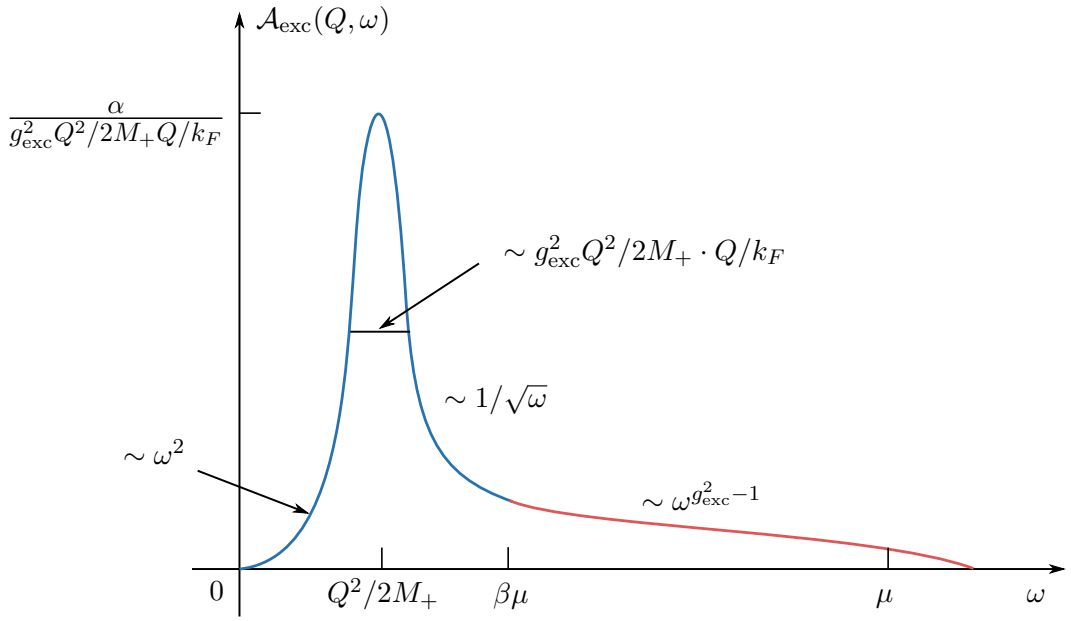

Figure 7.8.: Sketch of the exciton spectral function for $Q \ll k_F$.

7.2.3. Exciton momentum $k_F \ll Q \ll k_F/\sqrt{\beta}$

In this regime, if we consider two-particle processes only, the indirect threshold is shifted from $\omega_I = 0$ to $\omega_I = (Q - 2k_F)^2/2M_+$. The reason for this is the following: The maximal momentum of a Fermi-sea electron-hole pair with zero energy is $2k_F$. Thus, the full momentum of the exciton can no longer be transferred to the Fermi-sea at no energy cost. A sketch of the resulting two thresholds is shown in Fig. 7.9.

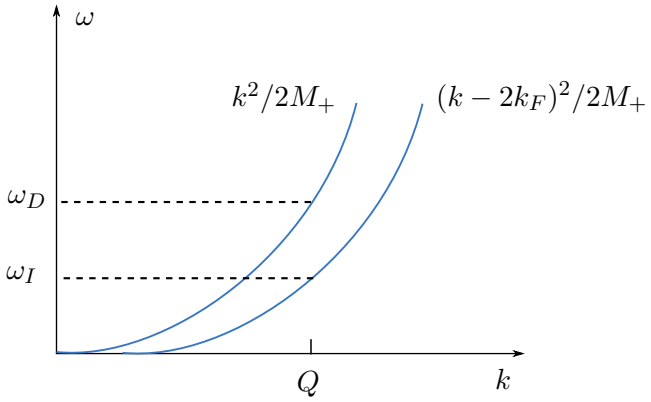

Figure 7.9.: Sketch of the two thresholds for $Q \gg k_F$.

We will disregard higher order scattering processes: These will extend the threshold all the way down to $\omega = 0$, but with a prefactor at least of order $\mathcal{O}(g_{\text{exc}}^4)$.

Studying (7.28) for small detunings ϵ from ω_I, we obtain:

$$\Im\left[\Sigma(Q,\epsilon)\right] = -\alpha g_{\text{exc}}^2 \frac{\epsilon^2}{\sqrt{\beta\mu \cdot Q^2/2M_+}} \cdot \theta(\epsilon) \ , \qquad \epsilon \ll (Q-2k_F)^2/M_+ \ . \tag{7.32}$$

We estimate the inverse lifetime as:

$$\Im\left[\Sigma(Q, Q^2/2M_+)\right] \sim -\alpha g_{\text{exc}}^2 Q^2/2M_+ \cdot k_F/Q \ . \tag{7.33}$$

The additonal suppression by k_F/Q is easily seen from (7.28): For $Q \gg k_F$, the angle between Q and q is not strongly restricted, such that the inverse lifetime is proportional to $Q^2/2M_+ - (Q-k_F)^2/2M_+$, i.e. the typical change of energy of an exciton as a result of a scattering.

The region where $\Im[\Sigma] \sim \omega^{3/2}$ will be absent, and for $Q^2/2M_+ \ll \omega \ll \mu$ we recover the $(M = \infty)$ powerlaw.

The resulting spectrum is sketched in Fig. 7.10.

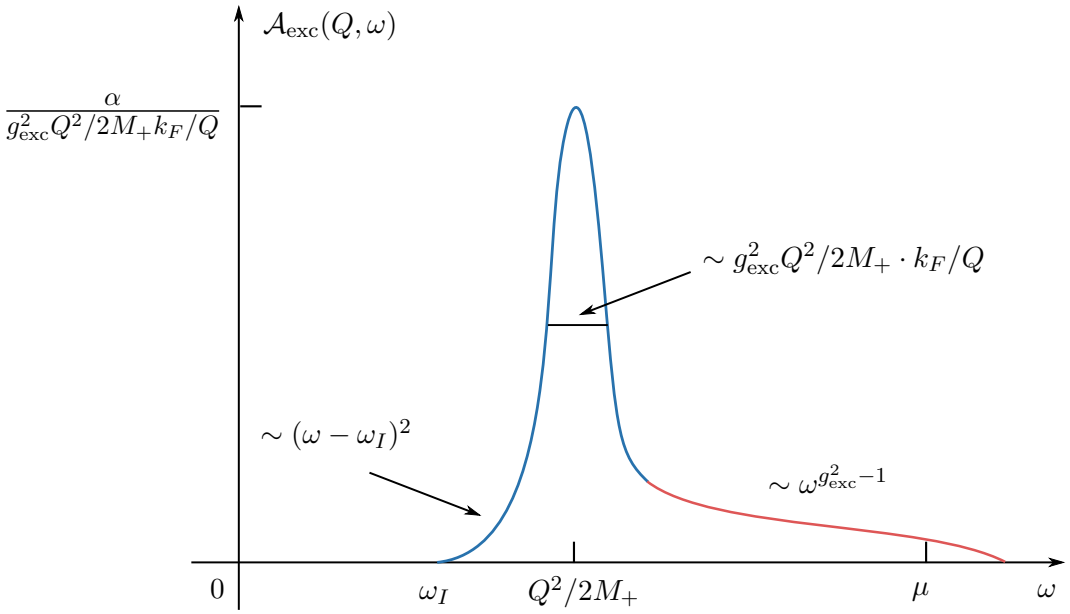

Figure 7.10.: Sketch of the spectrum for $k_F \ll Q \ll k_F/\sqrt{\beta}$.

7.2.4. Exciton momentum $Q \gg k_F/\sqrt{\beta}$

This regime is slightly academic for the exciton, but it is of relevance for the polariton where the mass ratio is very large instead of very small. The low-energy behaviour should be the same as in the previous case. For the inverse lifetime we only obtain μ, independent of Q – basically, in a scattering the incoming electron can come from anywhere in the Fermi sea.

Since now $Q^2/2M_+ \gg \mu$, no Anderson orthogonality powerlaw is left in any energy region.

7.3. Outlook on polaritons

Using a bare photon line as self-energy for the exciton, and disregarding the photon linewidth, we obtain the exciton-polariton:

$$\alpha \cdot G_{\rm ep}(Q,\omega) \equiv \frac{1}{\alpha^{-1} G_{\rm exc}(Q,\omega)^{-1} - \gamma_0 \left(\omega - \delta - Q^2/2m_{\rm cav} + i0^+\right)^{-1}} \,, \tag{7.34}$$

where δ is the detuning of the cavity mode from $E_G + \mu(1+\beta) - E_B$, and γ_0 is the light-matter coupling (c.f. (1.53)). We specialize on a situation as in Ref. [1], where the cavity is exactly tuned to the exciton resonance, i.e. $\delta = 0$.

Rewriting (7.34) in the standard Green's function form, we obtain two polariton branches, split by $2g_{\rm ep}$, where

$$g_{\rm ep} = \sqrt{\gamma_0 \alpha} \,. \tag{7.35}$$

We now consider energies close to the lower polariton, $\omega \simeq -g_{\rm ep}$, which is a well defined quasiparticle. By contrast, the lifetime of the upper polariton is relatively small since it

can decay into the lower polariton and also in the continuum of electron hole states if $g_{\mathrm{ep}} > E_B$.

Assuming that $Q^2/2m_{\mathrm{cav}} \ll g_{\mathrm{ep}}$, we obtain for the lower polariton:

$$G_{\mathrm{lp}}(Q,\omega) \simeq \frac{1}{2} \cdot \frac{1}{\omega + g_{\mathrm{ep}} - Q^2/2m_{\mathrm{p}} + i\delta} \ , \tag{7.36}$$

where $m_{\mathrm{p}} = m_{\mathrm{cav}}/2$ is the polariton mass.

If g_{ep} is sufficiently large, the quasiparticle interacting with the Fermi sea is no longer an exciton, but rather a polariton. To obtain the power laws for the polariton spectral function, we should then replace all ladders by ladders dressed by photon lines, i.e. replace G_{exc} by G_{lp}. In principle the calculation of self-energies then proceeds completely analogous to the exciton case, leading to expressions like (7.28). One only has to replace β by

$$\kappa = m/m_{\mathrm{p}} \ , \tag{7.37}$$

which is a very large instead of a small factor. In the calculation of the self-energy, for very small energies, $\omega + g_{\mathrm{ep}} \ll Q^2/\kappa m$ we expect the same results as in the exciton case; for larger energies, factors subleading in ω that get multiplied with κ need to be considered consistently. These calculations remain to be accomplished.

Appendices

A. Calculation of the crossed diagram with constant self-energy

In this appendix, we will show how to compute the momentum integrals for the crossed diagram of Fig. 3.12. We start from expression (3.36):

$$\Pi_{\text{cross}}(\Omega) = -\frac{\gamma_0 V_0^2}{(2\pi)^6}\int d\mathbf{k}_1 \int d\mathbf{k}_2 \int d\mathbf{k}_3\,(1-n_F(\mathbf{k}_1))\,n_F(\mathbf{k}_2)\,(1-n_F(\mathbf{k}_3)) \tag{A.1}$$
$$\cdot\,\frac{1}{(\Omega+i\Gamma-\Omega_I-(\epsilon_{\mathbf{k}_1}-\mu)-E_{\mathbf{k}_1})\,(\Omega+i\Gamma-\Omega_I-(\epsilon_{\mathbf{k}_3}-\mu)-E_{\mathbf{k}_3})}$$
$$\cdot\,\frac{1}{(\Omega+i\Gamma-\Omega_I-(\epsilon_{\mathbf{k}_1}-\mu)-(\epsilon_{\mathbf{k}_3}-\mu)+(\epsilon_{\mathbf{k}_2}-\mu)-E_{\mathbf{k}_1+\mathbf{k}_3-\mathbf{k}_2})}\,.$$

First, we will carry out the integral over k_2 and the two nontrivial angle integrals, showing that the resulting logarithm has the form

$$\log\left(\frac{\Omega-\Omega_D-(\epsilon_{\mathbf{k}_1}-\mu)-(\epsilon_{\mathbf{k}_3}-\mu)+i\beta\mu}{-\mu}\right)\,. \tag{A.2}$$

We switch to a dimensionless integration and introduce the following notations:

$$\mathbf{q}=\mathbf{k}_1+\mathbf{k}_3\,,\qquad \phi=\measuredangle(\mathbf{q},\mathbf{k}_2)\,,\qquad x=\frac{k_2^2}{2m}/\mu \tag{A.3}$$
$$\gamma=\frac{\Omega+i\Gamma-\Omega_I-(\epsilon_{\mathbf{k}_1}-\mu)-(\epsilon_{\mathbf{k}_3}-\mu)}{\mu}\,.$$

With these, we obtain for the $\mathbf{k}_2$-integral:

$$\frac{\rho}{2\pi}\int_0^{2\pi}d\phi\int_0^1\frac{dx}{\gamma-\frac{q^2}{2M\mu}-1+(1-\beta)x-\sqrt{x}\cdot\frac{qk_F}{M\mu}\cos(\phi)}\,. \tag{A.4}$$

To begin with, we analyse the parameter γ. We are mostly interested in the energy range $\Omega\in[\Omega_I,\Omega_I+\beta\mu]$ (recall that $\Omega_D=E_G+\mu(1+\beta)=\Omega_I+\beta\mu$). Hence, we can assume $\Omega-\Omega_I\in\mathcal{O}(\beta\mu)$. Furthermore, the integrals over $\mathbf{k}_1,\mathbf{k}_3$ in (A.1) will be dominated by the region where $\epsilon_{\mathbf{k}_1}-\mu,\epsilon_{\mathbf{k}_3}-\mu\in\mathcal{O}(\beta\mu)$. Finally, $\Gamma=g^2\beta\mu$.

Thus, we see that the dominant contribution to (A.4) comes from $|\gamma|\in\mathcal{O}(\beta)$. Then in the denominator of (A.4) we have the parameter $\frac{q^2}{2M\mu}$. It is clear that this is at most of order $\mathcal{O}(\beta)$. Therefore, we conclude that the $x-$integral will be dominated by it's upper boundary. Thus, we can approximate $\sqrt{x}$ in the the integral by it's expansion around 1. Carrying out the x-integral then gives with logarithmic accuracy:

$$\frac{\rho}{2\pi}\int_0^{2\pi}d\phi\log\left(\gamma-\frac{q^2}{2M\mu}-\beta-\frac{3}{2}\frac{qk_F}{M\mu}\cos(\phi)\right)\,, \tag{A.5}$$

where we have disregarded a global prefactor of $\frac{1}{1+\beta} \simeq 1$. Note that the logarithm is well defined since γ is complex. We now introduce the notations

$$B = \gamma - \frac{q^2}{2M\mu} - \beta \ , \qquad C = -\frac{3}{2}\frac{qk_F}{M\mu} \ .$$

We can distinguish 3 cases:

1. $|B| \gg |C|$. Then

$$\frac{\rho}{2\pi}\int_0^{2\pi} d\phi \log\left(B + C\cos(\phi)\right) \simeq \rho \log(|B|) \ . \tag{A.6}$$

2. $|C| \gg |B|$. Then

$$\frac{\rho}{2\pi}\int_0^{2\pi} d\phi \log\left(B + C\cos(\phi)\right) \simeq \rho \log(|C|) + \frac{\rho}{2\pi}\int_0^{2\pi} d\phi \log(|\cos(\phi)|) \tag{A.7}$$

$$= \rho\log(|C|) - \pi\log(4) \simeq \rho\log(|C|) \ .$$

The first estimate of (A.7) of course breaks down for $\cos(\phi)$ very small. But since the phase measure of these angles is negligibly small, and all appearing singularities of type $\log(|\cos(\phi)|)$ are integrable, this does not lead to problems.

3. $|C| \simeq |B|$. Then

$$\frac{\rho}{2\pi}\int_0^{2\pi} d\phi \log\left(B + C\cos(\phi)\right) \simeq \rho \log(|C|) + \frac{\rho}{2\pi}\int_0^{2\pi} d\phi \log(1+\cos(\phi)) \tag{A.8}$$

$$= \rho\log(|C|) - \pi\log(4) \simeq \rho\log(|C|) \ .$$

Alltogether we obtain:

$$\rho \log\left(\max\left\{\left|\gamma - \frac{q^2}{2M\mu} - \beta\right|, \frac{3}{2}\frac{qk_F}{M\mu}\right\}\right) \ . \tag{A.9}$$

Let us proceed with the second nontrivial angular integration. Writing

$$\theta = \measuredangle(\mathbf{k}_1, \mathbf{k}_3) \ , \tag{A.10}$$

it reads:

$$\int_0^{2\pi} d\theta \log\left(\max\left\{\left|\gamma - \frac{q^2}{2M\mu} - \beta\right|, \frac{3}{2}\frac{qk_F}{M\mu}\right\}\right) \ , \tag{A.11}$$

with $q = \sqrt{k_1^2 + k_3^2 + 2k_1k_3\cos(\theta)}$.

First we simplify the argument of the logarithm. We need to check two cases:

1. $q \ll k_F$. Then we can savely replace

$$\left|\gamma - \frac{q^2}{2M\mu} - \beta\right| \qquad \text{by} \qquad |\gamma - \beta| \ .$$

2. $q \simeq k_F$, i.e. $\frac{q^2}{2M\mu} \simeq \beta$.

   Then one can distiguish 3 subcases: $|\gamma| \ll \beta$, $|\gamma| \simeq \beta$, $|\gamma| \gg \beta$, and it is easily seen that one can always write

$$\max\left\{|\gamma-\beta|, \frac{qk_F}{M\mu}\right\} \qquad \text{instead of} \qquad \max\left\{\left|\gamma - \frac{q^2}{2M\mu} - \beta\right|, \frac{3}{2}\frac{qk_F}{M\mu}\right\} .$$

A third case $q \gg k_F$ does not show up because of the UV-cutoff on the $\mathbf{k}_1, \mathbf{k}_3$ - integrals. Therefore, we are left with

$$\int_0^{2\pi} d\theta \log\left(\max\left\{|\gamma-\beta|, \frac{qk_F}{M\mu}\right\}\right) \simeq \int_0^{2\pi} d\theta \log\left(\sqrt{|\gamma-\beta|^2 + \left(\frac{qk_F}{M\mu}\right)^2}\right) . \tag{A.12}$$

Now we notice that $q = \sqrt{k_1^2 + k_3^2 + 2k_1k_3\cos(\theta)} \simeq k_F\sqrt{2+2\cos^2(\theta)}$ since always $k_1, k_3 \in \mathcal{O}(k_F)$. Hence, we have to compare $|\gamma-\beta|^2$ with $\left(\frac{k_F^2}{M\mu}\right)^2 \simeq \beta^2$ analogous to (A.6) ff. Since again appearing integrands of the type $\log\left(1+\cos^2(\theta)\right)$ will be integrable, we finally end up with:

$$2\pi \log\left(\max\left\{|\gamma-\beta|, \beta\right\}\right) . \tag{A.13}$$

Inserting γ from (A.3), and restoring the correct phase of the logarithm, we obtain in terms of detuning $\nu = \Omega - \Omega_D$:

$$2\pi \log\left(\frac{\nu - (\epsilon_{\mathbf{k}_1} - \mu) - (\epsilon_{\mathbf{k}_3} - \mu) + i\beta\mu}{-\mu}\right) , \tag{A.14}$$

as claimed in the beginning.

With this result we can proceed with the calculation of $\Pi_{\text{cross}}(\Omega)$ as in (A.1), where we still have to perform the integrals over k_1, k_2 and one trivial angular integration, which gives an addtional factor of 2π. Furthermore, we will now restrict ourselfes to the non-perturbative regime $g \gg g_2(\beta)$ (c.f. section 3.3.4), where we can replace $g^2\beta\mu$ by $\beta\mu$ with logarithmic accuracy. Since the remaining denominators of (A.1) will yield logarithms, we can therefore write $i\beta\mu$ instead of $i\Gamma$. Changing variables:

$$y = \frac{k_1^2}{2m} - \mu , \qquad z = \frac{k_3^2}{2m} - \mu , \tag{A.15}$$

introducing the notation

$$\alpha = \nu + i\beta\mu , \tag{A.16}$$

and restoring all prefactors, we therefore get:

$$\Pi_{cross}(\nu) = -\gamma_0\rho g^2 \int_0^\xi dy \int_0^\xi dz \frac{1}{\alpha - y(1+\beta)} \frac{1}{\alpha - z(1+\beta)} \cdot \log\left(\frac{\alpha - y - z}{-\mu}\right) . \tag{A.17}$$

We can now replace $y(1+\beta),\ z(1+\beta)$ in the denominators by y, z: In doing so, we modify the argument of the resulting logarithm by β at most, but the the logarithms will be cut by β anyway. Furthermore, we ignore global prefactors $1/(1+\beta)$. Thus, we obtain the simpler form

$$\Pi_{\text{cross}}(\nu) = -\gamma_0 \rho g^2 \int_0^\xi dy \int_0^\xi dz \frac{1}{\alpha - y} \frac{1}{\alpha - z} \cdot \log\left(\frac{\alpha - y - z}{-\mu}\right) \ . \tag{A.18}$$

We now split the z-integration in two parts s.t. in the logarithm the term $-y-z$ just reads $-y$ or $-z$ with logarithmic accuracy. Then, using that $\mu \simeq \xi$, we can carry out the remaining integrals:

$$\begin{aligned}
&\Pi_{cross}(\nu) = -\gamma_0 \rho g^2 \int_0^\xi dy \frac{1}{\alpha - y} \cdot \qquad (A.19)\\
&\left\{ \int_0^y dz \frac{1}{\alpha - z} \cdot \log\left(\frac{\alpha - y}{-\xi}\right) + \int_y^\xi dz \frac{1}{\alpha - z} \cdot \log\left(\frac{\alpha - z}{-\xi}\right) \right\} = \\
&- \gamma_0 \rho g^2 \int_0^\xi dy \frac{1}{\alpha - y} \cdot \left\{ -\log\left(\frac{\alpha - y}{\alpha}\right) \log\left(\frac{\alpha - y}{-\xi}\right) + \frac{1}{2} \log^2\left(\frac{\alpha - y}{-\xi}\right) \right\} \simeq \\
&- \gamma_0 \rho g^2 \int_0^\xi dy \frac{1}{\alpha - y} \cdot \left(-\log\left(\frac{\alpha - y}{-\xi}\right) - \log\left(\frac{-\xi}{\alpha}\right) \right) \cdot \log\left(\frac{\alpha - y}{-\xi}\right) - \gamma_0 \rho g^2 \cdot \frac{1}{6} \log^3\left(\frac{\alpha}{-\xi}\right) \simeq \\
&\gamma_0 \rho g^2 \cdot \frac{1}{3} \log^3\left(\frac{\alpha}{-\xi}\right) - \gamma_0 \rho g^2 \cdot \frac{1}{2} \log^3\left(\frac{\alpha}{-\xi}\right) - \gamma_0 \rho g^2 \cdot \frac{1}{6} \log^3\left(\frac{\alpha}{-\xi}\right) = -\gamma_0 \rho g^2 \cdot \frac{1}{3} \log^3\left(\frac{\alpha}{-\xi}\right) \ .
\end{aligned}$$

Writing out α, our final result therefore reads:

$$\Pi_{\text{cross}}(\nu) = -\gamma_0 \rho g^2 \cdot \frac{1}{3} \log^3\left(\frac{-\nu - i\beta\mu}{\xi}\right) \ . \tag{A.20}$$

B. Calculation of the absorption power law at the indirect threshold

In the following we will present the evaluation of the absorption power law at the indirect threshold, starting from (4.13):

$$A_I(\epsilon) = \frac{\rho^3}{\pi^2}\frac{\gamma_0 V_0^2}{(\beta\mu)^2}\int_{x^2>\mu} d\mathbf{x}\int_{y^2>\mu} d\mathbf{y}\int_{z^2<\mu} d\mathbf{z} \tag{B.1}$$
$$\delta\left(\epsilon - \left(x^2-\mu\right) - \left(y^2-\mu\right) + \left(z^2-\mu\right) - \beta\left(\mathbf{x}+\mathbf{y}-\mathbf{z}\right)^2\right) \ .$$

Beginning with the $\mathbf{z}$-integral, we can linearize the dispersion relation, since all contributing momenta are very close to k_F:

$$\mathbf{z} \equiv \mathbf{e}_z(\sqrt{\mu}+\gamma) \qquad \Rightarrow \qquad z^2-\mu \simeq 2\sqrt{\mu}\gamma \ . \tag{B.2}$$

We also introduce the notations:

$$\mathbf{q} = \mathbf{x}+\mathbf{y} \ , \qquad \phi = \measuredangle(\mathbf{q},\mathbf{z}) \ , \qquad c = \cos(\phi) \ . \tag{B.3}$$

For later purpose we see from the fact that $\beta(\underbrace{\mathbf{x}+\mathbf{y}}_{\mathbf{q}}-\mathbf{z})^2 < \epsilon$ and $z \simeq \sqrt{\mu}$, that

$$q \simeq \sqrt{\mu} \ . \tag{B.4}$$

See also Fig. 4.2. In terms of the new notation (B.3), the $\mathbf{z}$-integrals reads:

$$2\int_{-1}^{1} dc \frac{1}{\sqrt{1-c^2}}\int_{-\sqrt{\mu}}^{0}(\sqrt{\mu}+\gamma)d\gamma \tag{B.5}$$
$$\delta\left(\underbrace{\epsilon-(x^2-\mu)-(y^2-\mu)-\beta q^2+2\beta cq\sqrt{\mu}-\beta\mu}_{\equiv C} + \gamma\underbrace{\left(2\sqrt{\mu}-2\sqrt{\mu}\beta+2cq\beta\right)}_{\equiv D}\right)$$

Since the only contribution to the integral comes from values of γ close to the upper boundary, we can write:

$$(\sqrt{\mu}+\gamma) \simeq \sqrt{\mu} \ . \tag{B.6}$$

Using $D \simeq 2\sqrt{\mu}$, the integral can then be taken easily, giving:

$$\int_{-1}^{1} dc \frac{1}{\sqrt{1-c^2}} \cdot \theta(C) \ . \tag{B.7}$$

We now rewrite the argument of the θ- function:

$$\theta(\underbrace{\epsilon-(x^2-\mu)-(y^2-\mu)-\beta q^2-\beta\mu}_{\equiv E}+2\beta cq\sqrt{\mu}) = \theta(c-(-E/2\beta q\sqrt{\mu})) \ . \tag{B.8}$$

Thus, (B.7) reads:

$$\theta(1+E/2\beta q\sqrt{\mu})\underbrace{\int_{-E/2\beta q\sqrt{\mu}}^{1} dc\frac{1}{\sqrt{1-c^2}}}_{\equiv I} \ . \tag{B.9}$$

Let us concentrate of the integral I. Since we are only interested in the power law, we can simpify $-E/2\beta q\sqrt{\mu}$ as follows: Firstly, the summands $(x^2-\mu)$, $(y^2-\mu)$ can be at most of order ϵ, or else e.g the θ- functions in (B.8) (or equivalently the δ- functions appearing before) will vanish. In addition, we can use the statement (B.4): $q \simeq \sqrt{\mu}$. Therefore, limiting ourselves to the correct order in ϵ only, we can write:

$$-E/2\beta q\sqrt{\mu} \sim 1-\frac{\epsilon}{\beta\mu} \ . \tag{B.10}$$

Thus, we see that the only contribution to I comes from angles around 0, as was sketched on the left hand side of Fig. 4.2. With these considerations, one obtains:

$$I \sim 0 + \mathrm{Arccos}(1-\frac{\epsilon}{\beta\mu}) \simeq \sqrt{\frac{2\epsilon}{\beta\mu}} \ , \tag{B.11}$$

where the last step came from an expansion of Arccos in $\sqrt{\epsilon}$. For later comparison with the results in [42], let us also consider the 3D case. In 3D we do not have the factor $1/\sqrt{1-c^2}$ in the c-integral, which leads to:

$$I_{3D} \sim \epsilon \ . \tag{B.12}$$

At this point, in the calculation of (B.1) we are left with the integral:

$$\int_{x^2>\mu}\int_{y^2>\mu} d\mathbf{x}\ d\mathbf{y}\ \theta(1+E/2\beta q\sqrt{\mu}) \ . \tag{B.13}$$

The condition in the θ-function can be rewritten as:

$$\epsilon > (x^2-\mu)+(y^2-\mu)+\beta(q-\sqrt{\mu})^2 \ . \tag{B.14}$$

It is clear that the summands $(x^2-\mu),(y^2-\mu)$ give a total factor of ϵ^2 to A_I. Then the condition $\epsilon > \beta(q-\sqrt{\mu})^2$ leads to:

$$q^2 \in \left[\mu - 2\sqrt{\frac{\mu\epsilon}{\beta}},\ \mu+2\sqrt{\frac{\mu\epsilon}{\beta}}\right] + \mathcal{O}(\epsilon) \ . \tag{B.15}$$

We further use

$$q^2 = (\mathbf{x}+\mathbf{y})^2 \overset{x,y\simeq\sqrt{\mu}}{\simeq} 2\mu(1+\cos(\theta)) \ , \qquad \theta = \measuredangle(\mathbf{x},\mathbf{y}) \ . \tag{B.16}$$

Then (B.15) gives a condition on θ:

$$\cos(\theta) \in \left[-\frac{1}{2}-\sqrt{\frac{\epsilon}{\beta\mu}},\ -\frac{1}{2}+\sqrt{\frac{\epsilon}{\beta\mu}}\right] \ , \tag{B.17}$$

which results in the phase-space-factor:

$$\int_{-\frac{1}{2}-\sqrt{\frac{\epsilon}{\beta\mu}}}^{-\frac{1}{2}+\sqrt{\frac{\epsilon}{\beta\mu}}} dc_1 \frac{1}{\sqrt{1-c_1^2}} \simeq \frac{4}{\sqrt{3}}\sqrt{\frac{\epsilon}{\beta\mu}} \ , \qquad c_1 = \cos(\theta) \ . \tag{B.18}$$

We note that the main contribution comes from $\theta \simeq 2\pi/3$ as was depicted on the right hand side of Fig. 4.2. In 3D this factor also goes as $\sqrt{\epsilon}$ since the factor $1/\sqrt{1-c_1^2}$ is nonsingular in the integration domain. Collecting all factors except for those of order 1, we thus arrive at:

$$A_I(\epsilon) \sim \rho^3 V_0^2 \left(\frac{\epsilon}{\beta\mu}\right)^3 \ . \tag{B.19}$$

The considerations above also show that in 3D one obtains:

$$A_I(\epsilon) \sim \rho^3 V_0^2 \left(\frac{\epsilon}{\beta\mu}\right)^{7/2} \ . \tag{B.20}$$

due to the higher power law in (B.12) in comparison to (B.11).

C. Exemplary solution of a Bethe-Salpeter equation

In this section, we will present the derivation of (4.50) for the simple case $|\Omega - \Omega_D| > \beta\mu$. The relevant equations then read:

$$\Lambda(x_1, \Omega) \simeq 1 + \int_{|\Omega-\Omega_D|}^{\xi} dx_3 \; \frac{1}{x_3} I_2(x_1, x_3, \Omega) \; \Lambda(x_3, \Omega) \tag{C.1}$$

$$\Pi(\Omega) = -\gamma_0 \rho \int_{|\Omega-\Omega_D|}^{\xi} dx_1 \; \frac{1}{x_1} \Lambda(x_1, \Omega) \tag{C.2}$$

$$I_2(x_1, x_3, \Omega) = g + g^2 \log\left(\max\left\{ \frac{|x_1 + x_3 + \Omega - \Omega_D|}{\xi}, \beta \right\} \right) \; . \tag{C.3}$$

Since $x_1, x_3 > |\Omega - \Omega_D| > \beta\mu$, we can simplify I_2 as

$$I_2(x_1, x_3) = g + \begin{cases} g^2 \log(x_3/\xi) & x_1 < x_3 \\ g^2 \log(x_1/\xi) & x_1 > x_3 \end{cases} \; . \tag{C.4}$$

With the notations

$$x = x_1/\xi \; , \qquad y = x_3/\xi \; , \qquad \nu = (\Omega - \Omega_D)/\xi \; , \tag{C.5}$$

(C.1) then reads:

$$\Lambda(x, \nu) = 1 + \int_{\nu}^{x} \frac{dy}{y} \left[g + g^2 \log(x) \right] \Lambda(y, \nu) + \int_{x}^{1} \frac{dy}{y} \left[g + g^2 \log(y) \right] \Lambda(y, \nu) \; . \tag{C.6}$$

Taking the derivative w.r.t. x once gives:

$$\Lambda'(x, \nu) = \frac{1}{x} g^2 \int_{\nu}^{x} \frac{dy}{y} \; \Lambda(y, \nu) \; , \tag{C.7}$$

and taking the derivative one more time yields:

$$x\Lambda(x, \nu)'' + \Lambda'(x, \nu) = \frac{g^2 \Lambda(x, \nu)}{x} \; . \tag{C.8}$$

The general solution to (C.8) reads:

$$\Lambda(x, \nu) = A(\nu) x^g + B(\nu) x^{-g} \qquad A(\nu), B(\nu) \in \mathbb{R} \; . \tag{C.9}$$

From (C.7) we can deduce the following boundary condition:

$$\Lambda'(\nu, \nu) = 0 \; , \tag{C.10}$$

which leads to

$$A = B \cdot \nu^{-2g} \ . \tag{C.11}$$

Furthermore, from (C.6) we can extract the boundary condition:

$$\Lambda(1,\nu) = 1 + \int_{\nu}^{1} \frac{dy}{y}\, g\Lambda(y,\nu) \ . \tag{C.12}$$

Inserting (C.9) and (C.11) into (C.12), we arrive at:

$$A = \frac{\nu^{-2g}}{2} \ , \qquad B = \frac{1}{2} \ . \tag{C.13}$$

$\Lambda(x,\nu)$ is now determined. Inserting it into (C.2) and switching to the detuning from the indirect threshold ϵ:

$$\nu = \frac{\epsilon - \beta\mu}{\xi} \ , \tag{C.14}$$

we obtain the result (4.50) for $|\epsilon - \beta\mu| > \beta\mu$

$$\Pi(\Omega) = -\frac{\gamma_0 \rho}{2g} \left(\left(\frac{\xi}{|\epsilon - \beta\mu|} \right)^{2g} - 1 \right) \ . \tag{C.15}$$

Bibliography

[1] S. Smolka, W.Wuester, F. Haupt, S. Faelt, W. Wegschneider, and A. Imamoglu. Cavity quantum electrodynamics with many-body state of a two-dimensional electron gas. *Science*, 346(6207):332–335, Oct 2014. See pages: 9, 10, 13, 26, 27, 28, 29, 30, 88, 89, 90, 96, 97, 98, 101, 102, 104, 114

[2] C. Weisbuch, M. Nishioka, A. Ishikawa, and Y. Arakawa. Observation of the coupled exciton-photon mode splitting in a semiconductor quantum microcavity. *Phys. Rev. Lett.*, 69:3314–3317, Dec 1992. See page: 10

[3] J. Kasprzak, M. Richard, S. Kundermann, A. Baas, P. Jeambrun, J. M. J. Keeling, F. M. Marchetti, M. H. Szymanska, R. Andre, J. L. Staehli, V. Savona, P. B. Littlewood, B. Deveaud, and Le Si Dang. Bose-einstein condensation of exciton polaritons. *Nature*, 443(7110):409–414, September 2006. See page: 10

[4] Fabrice P. Laussy, Alexey V. Kavokin, and Ivan A. Shelykh. Exciton-polariton mediated superconductivity. *Phys. Rev. Lett.*, 104:106402, Mar 2010. See page: 10

[5] A. Gabbay, Yulia Preezant, E. Cohen, B. M. Ashkinadze, and L. N. Pfeiffer. Fermi edge polaritons in a microcavity containing a high density two-dimensional electron gas. *Phys. Rev. Lett.*, 99:157402, Oct 2007. See pages: 10, 26, 27, 96

[6] G. D. Mahan. Excitons in metals: Infinite hole mass. *Phys. Rev.*, 163:612–617, Nov 1967. See pages: 10, 29, 59, 60, 63, 83, 103

[7] B. Roulet, J. Gavoret, and P. Nozières. Singularities in the x-ray absorption and emission of metals. i. first-order parquet calculation. *Phys. Rev.*, 178:1072–1083, Feb 1969. See pages: 10, 29, 39, 40, 41, 59, 64, 80, 81, 83

[8] P. Nozi‘eres, J. Gavoret, and B. Roulet. Singularities in the x-ray absorption and emission of metals. ii. self-consistent treatment of divergences. *Phys. Rev.*, 178:1084–1096, Feb 1969. See pages: 10, 39, 59, 64, 68, 80

[9] P. Nozières and C.T de Dominicis. Singularities in the x-ray absorption and emission of metals. iii. one-body theory exact solution. *Phys. Rev.*, 178:1097–1107, Feb 1969. See pages: 10, 41, 59

[10] C.F. Klingshirn. *Semiconductor Optics*. Springer, 2007. See pages: 10, 11, 12

[11] C. Jacobini. *Theory of Electron Transport in Semiconductors*. Springer, 2010. See page: 12

[12] P.T. Coleridge, Hayneb, P. Zawadzkia, and A.S. Sachrajdaa. Effective masses in high-mobility 2d electron gas structures. *Surface Science, Proceedings of the Eleventh International Conference on the Electronic Properties of Two-Dimensional Systems*, 1996. See page: 13

[13] W. Pan, K. Lai, S. P. Bayrakci, N. P. Ong, D. C. Tsui, L. N. Pfeiffer, and K. W. West. Cyclotron resonance at microwave frequencies in two-dimensional hole system in algaas/gaas quantum wells. *Appl. Phys. Lett. 83, 3519*, 2003. See page: 13

[14] M. Kira and S. W. Koch. *Semiconductor Quantum Optics*. Cambridge Univerity Press, 2012. See page: 13

[15] Y.Yamamotu and A. Imamoglu. *Mesoscopic Quantum Optics*. John Wiley & Sons, 1999. See pages: 13, 21

[16] I. Carusotto and C. Ciuti. Quantum fluids of light. *Reviews of Modern Physics*, 85, Feb 2013. See page: 16

[17] G. H. Wannier. The Structure of Electronic Excitation Levels in Insulating Crystals. *Phys. Rev.*, 52:191, 1937. See page: 17

[18] J. J. Hopfield. Theory of the contribution of excitons to the complex dielectric constant of crystals. *Phys. Rev.*, 112:1555–1567, Dec 1958. See page: 18

[19] A. L. Fetter and J. D. Walecka. *Quantum Theory of Many-Particle Systems*. Dover Publications, 2003. See page: 18

[20] E. W. Weisstein. Titchmarsh theorem. MathWorld–A Wolfram Web Resource. http://mathworld.wolfram.com/TitchmarshTheorem.html. See page: 19

[21] G.D.Mahan. *Many-particle-physics*. Kluwer Academic/Plenum Publishers, 3rd edition, 2000. See pages: 19, 21, 22, 31, 32, 34, 35, 38, 42, 60, 72

[22] H. Haug and S. W. Koch. *Quantum Theory of the Optical and Electronic Properties of Semiconductors*. World Scientific, 2009. See pages: 20, 21, 24, 26

[23] Y.Yamamotu, F.Tassone, and H.Cao. *Semiconductor Cavity Quantum Electrodynamics*. Number 169 in Springer Tracts in Modern Physics. Springer, 2000. See page: 26

[24] Maarten Baeten and Michiel Wouters. Many-body effects of a two-dimensional electron gas on trion-polaritons. *Phys. Rev. B*, 91:115313, Mar 2015. See page: 26

[25] Marius Grundmann. *The Physics of Semiconductors*. Springer, second edition edition, 2010. See page: 27

[26] N.W. Ashcroft and M.N.Mermin. *Solid State Physics*. Holt, Rinehart and Winston, 1976. See page: 27

[27] J. Gavoret, P. Nozières, B. Roulet, and M. Combescot. Optical absorption in degenerate semiconductors. *Journal de Physique, 1969, 30 (11-12), pp.987-997. <10.1051/jphys:019690030011- 12098700>. <jpa-00206867>*, 1969. See pages: 29, 54, 60, 68, 74, 83, 85, 86, 103

[28] A. O. Gogolin, A. A. Nersesyan, and A. M. Tsvelik. *Bosonization and Strongly Correlated Systems*. Cambridge Univerity Press, 2004. See pages: 32, 33, 34, 80

[29] Wolfgang Münder, Andreas Weichselbaum, Moshe Goldstein, Yuval Gefen, and Jan von Delft. Anderson orthogonality in the dynamics after a local quantum quench. *Phys. Rev. B*, 85:235104, Jun 2012. See pages: 32, 33, 59

[30] P.W. Anderson. Infrared catastrophe in fermi gases with local scattering potentials. *Phys. Rev. Lett.*, 18:1049, Jun 1967. See page: 32

[31] Hakan E. Türeci, M. Hanl, M. Claassen, A. Weichselbaum, T. Hecht, B. Braunecker, A. Govorov, L. Glazman, A. Imamoglu, and J. von Delft. Many-body dynamics of exciton creation in a quantum dot by optical absorption: A quantum quench towards kondo correlations. *Phys. Rev. Lett.*, 106:107402, Mar 2011. See page: 34

[32] C. Latta, F. Haupt, M. Hanl, A. Weichselbaum, M. Claassen, W. Wuester, P. Fallahi, S. Faelt, L. Glazman, J. von Delft, H. E. Tureci, and A. Imamoglu. Quantum quench of kondo correlations in optical absorption. *Nature*, 474(7353):627–630, June 2011. See page: 34

[33] K. D. Schotte and U. Schotte. Tomonaga's model and the threshold singularity of x-ray spectra of metals. *Phys. Rev.*, 182:479–482, Jun 1969. See pages: 34, 60

[34] A. Rosch. Private communications with J. von Delft. See page: 42

[35] Achim Rosch and Thilo Kopp. Heavy particle in a d-dimensional fermionic bath: A strong coupling approach. *Phys. Rev. Lett.*, 75:1988–1991, Sep 1995. See pages: 45, 46, 50, 103, 110

[36] Thilo Kopp, Andrei E. Ruckenstein, and Stefan Schmitt-Rink. Single spin flip in the nagaoka state: Problems with the gutzwiller wave function. *Phys. Rev. B*, 42:6850–6852, Oct 1990. See page: 45

[37] Bogdan Mihaila. Lindhard-function of a d-dimensional Fermi gas. *http://arxiv.org/abs/1111.5337*, November 2011. See pages: 47, 112

[38] P. Nozi'eres. The effect of recoil on edge singularities. *Journal de Physique I, EDP Sciences, <10.1051/jp1:1994188>. <jpa-00246990>*, 4 (9):1275–1280, 1994. See pages: 53, 60

[39] J.J. Hopfield. Infrared divergences, x-ray edges, and all that. *Comments Solid State Phys.*, 2:40–49, 1969. See page: 59

[40] M. Combescot and P. Nozières. Infrared catastrophy and excitons in the x-ray spectra of metals. *Journal de Physique*, 32, 1971. See pages: 60, 63, 88, 104, 106

[41] K. Ohtaka and Y. Tanabe. Theory of the soft-x-ray edge problem in simple metals: historical survey and recent developments. *Rev. Mod. Phys.*, 62:929–991, Oct 1990. See page: 60

[42] Andrei E. Ruckenstein and Stefan Schmitt-Rink. Many-body aspects of the optical spectra of bulk and low-dimensional doped semiconductors. *Phys. Rev. B*, 35:7551–7557, May 1987. See pages: 60, 74, 77, 103, 122

[43] T. Uenoyama and L. J. Sham. Effect of finite hole mass on edge singularities in optical spectra. *Phys. Rev. Lett.*, 65:1048–1051, Aug 1990. See page: 60

[44] Pawel Hawrylak. Optical properties of a two-dimensional electron gas: Evolution of spectra from excitons to fermi-edge singularities. *Phys. Rev. B*, 44:3821–3828, Aug 1991. See page: 60

[45] G. D. Mahan. Excitons in degenerate semiconductors. *Phys. Rev.*, 153:882–889, Jan 1967. See page: 62

[46] Gerrit E. W. Bauer. Excitons in the quasi-two-dimensional electron gas. *Phys. Rev. B*, 45:9153–9162, Apr 1992. See page: 63

[47] Maarten Baeten and Michiel Wouters. Fermi edge polaritons in a highly degenerate 2d electron gas: a diagrammatic theory. *http://arxiv.org/abs/1301.4119*, 2013. See pages: 63, 88

[48] Elias Burstein. Anomalous optical absorption limit in insb. *Phys. Rev.*, 93:632–633, Feb 1954. See page: 67

[49] N. S. Averkiev and M. M. Glazov. Light-matter interaction in doped microcavities. *Phys. Rev. B*, 76:045320, Jul 2007. See page: 88

[50] Maarten Baeten and Michiel Wouters. Polariton formation in a microcavity with a doped quantum well: Roles of the fermi edge singularity and anderson orthogonality catastrophe. *Phys. Rev. B*, 89:245301, Jun 2014. See pages: 88, 90

[51] G. Malpuech, A. Kavokin, A. Di Carlo, and J. J. Baumberg. Polariton lasing by exciton-electron scattering in semiconductor microcavities. *Phys. Rev. B*, 65:153310, Apr 2002. See page: 104

[52] Moshe Goldstein. Private communications, 2015. See page: 105

Acknowledgement

This thesis would not have been possible without the advice and support from many people:

First of all I want to express my gratitude to Jan von Delft for his choice of the topic, his helpful and sympathetic supervision, and the excellent working conditions in his group. I also thank him for introducing me to my international coworkers, and for encouraging and financing my visits in Zurich and Tel Aviv.

I am very grateful to my second supervisor Oleg Yevtushenko for his steady support and his technical assistance. What is more, I deeply appreciated his general teaching and advice, which helped me grow as a physicist.

I want to thank all members of our group who created a very pleasant work atmosphere. My special thanks goes to Lukas Weidinger, for our numerous physical and real-life discussions. Furthermore, I enourmously benefited from the physical input of Dennis Schimmel who always had an open ear for me.

I owe a lot of general understanding to my visit of Moshe Goldstein in Tel Aviv. His ideas substantially advanced my thesis, and I found working with him very enjoyable.

I am thankful to Ataç Imamoğlu for his experiment that motivated this thesis, for hosting me in Zurich and for giving me access to his measurements.

I gratefully acknowledge the discussions with Leonid Glazman, whose suggestions were very helpful to me.

A special thanks goes to all my friends, especially to my science buddies Flo and Basti, for making my physics study such a nice time.

Last but certainly not least I want to thank my family for their dedicated and enduring support in all aspects of life.

Statement of authorship

I hereby certify that this thesis is the result of my own work. Used material from published or unpublished work of others is referenced clearly in the text.

Munich, Mai 25, 2015